AFRL-OSR-VA-TR-2012-1771

INVESTIGATION OF IONOSPHERIC TURBULENCE AND WHISTLER WAVE INTERACTIONS WITH SPACE PLASMAS

Min-Chang Lee
Department of Electrical and Computer Engineering BostonUniversity
8 St. Mary's Street Boston, MA 02215

21/11/2012
Final Report

REPORT DOCUMENTATION PAGE

Form Approved
OMB No. 0704-0188

PLEASE DO NOT RETURN YOUR FORM TO THE ABOVE ORGANIZATION.

1. REPORT DATE *(DD-MM-YYYY)*	2. REPORT TYPE	3. DATES COVERED *(From - To)*
21/11/2012	Final Report	June 1, 2009 - August 31, 2012

4. TITLE AND SUBTITLE

INVESTIGATION OF IONOSPHERIC TURBULENCE AND WHISTLER WAVE INTERACTIONS WITH SPACE PLASMAS

5a. CONTRACT NUMBER

5b. GRANT NUMBER

FA9550-09-1-0391

5c. PROGRAM ELEMENT NUMBER

6. AUTHOR(S)

Min-Chang Lee

5d. PROJECT NUMBER

5e. TASK NUMBER

5f. WORK UNIT NUMBER

7. PERFORMING ORGANIZATION NAME(S) AND ADDRESS(ES)

Department of Electrical and Computer Engineering
Boston University
8 St. Mary's Street
Boston, MA 02215

8. PERFORMING ORGANIZATION REPORT NUMBER

9. SPONSORING/MONITORING AGENCY NAME(S) AND ADDRESS(ES)

Air Force Office of Scientific Research
875 N. Randolph Street., Suite 3112
Arlington, Virginia 22203
Program Manager: Dr. Cassandra Fesen

10. SPONSOR/MONITOR'S ACRONYM(S)

AFOSR/NE

11. SPONSOR/MONITOR'S REPORT NUMBER(S)

12. DISTRIBUTION/AVAILABILITY STATEMENT

DISTRIBUTION A:
Distribution approved for
public release.

13. SUPPLEMENTARY NOTES

14. ABSTRACT

We report on AFOSR-sponsored research titled “Investigation of Ionospheric Turbulence and Whistler Wave Interactions with Space Plasmas" (FA9550-09-1-0391 for the period of June 1, 2009 – August 31, 2012). It includes two parts: (1) naturally occurring and radio wave-induced large-and medium-scale ionospheric turbulence, and (2) whistler wave-generated short-scale ionospheric turbulence. Two types of large- and medium-scale ionospheric turbulence are discussed separately, viz., (a) anomalous heat source-induced acoustic gravity waves (AGW), and (b) HF radio wave-excited large ionospheric ducts. Our whistler wave injection experiments have been conducted at Arecibo, Puerto Rico, and Gakona, Alaska, using Naval 40.75 kHz transmitter (code-named NAU) and HAARP heater to generate VLF whistler waves, respectively. These experiments are aimed at the controlled study of whistler wave interactions with ionospheric plasma and inner (outer) radiation belts at L = 1.35 (4.6). Several journal and conference papers as well as students’ Ph.D./M.S./B.S. theses have resulted from these research projects.

15. SUBJECT TERMS

Ionospheric turbulence, whistler waves, ionospheric ducts, acoustic gravity waves (AGWs), anomalous heat sources, inner and outer radiation belts, L parameter, whistler wave interactions with ionospheric plasmas, whistler wave interactions with charged particles in radiation belts,

16. SECURITY CLASSIFICATION OF:			17. LIMITATION OF ABSTRACT	18. NUMBER OF PAGES	19a. NAME OF RESPONSIBLE PERSON
a. REPORT	b. ABSTRACT	c. THIS PAGE			Min-Chang Lee
unclassified	unclassified	unclassified	unclassified	130	19b. TELEPHONE NUMBER *(Include area code)* 617-353-3363

Reset

Standard Form 298 (Rev. 8/98)
Prescribed by ANSI Std. Z39.18
Adobe Professional 7.0

INSTRUCTIONS FOR COMPLETING SF 298

1. REPORT DATE. Full publication date, including day, month, if available. Must cite at least the year and be Year 2000 compliant, e.g. 30-06-1998; xx-06-1998; xx-xx-1998.

2. REPORT TYPE. State the type of report, such as final, technical, interim, memorandum, master's thesis, progress, quarterly, research, special, group study, etc.

3. DATES COVERED. Indicate the time during which the work was performed and the report was written, e.g., Jun 1997 - Jun 1998; 1-10 Jun 1996; May - Nov 1998; Nov 1998.

4. TITLE. Enter title and subtitle with volume number and part number, if applicable. On classified documents, enter the title classification in parentheses.

5a. CONTRACT NUMBER. Enter all contract numbers as they appear in the report, e.g. F33615-86-C-5169.

5b. GRANT NUMBER. Enter all grant numbers as they appear in the report, e.g. AFOSR-82-1234.

5c. PROGRAM ELEMENT NUMBER. Enter all program element numbers as they appear in the report, e.g. 61101A.

5d. PROJECT NUMBER. Enter all project numbers as they appear in the report, e.g. 1F665702D1257; ILIR.

5e. TASK NUMBER. Enter all task numbers as they appear in the report, e.g. 05; RF0330201; T4112.

5f. WORK UNIT NUMBER. Enter all work unit numbers as they appear in the report, e.g. 001; AFAPL30480105.

6. AUTHOR(S). Enter name(s) of person(s) responsible for writing the report, performing the research, or credited with the content of the report. The form of entry is the last name, first name, middle initial, and additional qualifiers separated by commas, e.g. Smith, Richard, J, Jr.

7. PERFORMING ORGANIZATION NAME(S) AND ADDRESS(ES). Self-explanatory.

8. PERFORMING ORGANIZATION REPORT NUMBER. Enter all unique alphanumeric report numbers assigned by the performing organization, e.g. BRL-1234; AFWL-TR-85-4017-Vol-21-PT-2.

9. SPONSORING/MONITORING AGENCY NAME(S) AND ADDRESS(ES). Enter the name and address of the organization(s) financially responsible for and monitoring the work.

10. SPONSOR/MONITOR'S ACRONYM(S). Enter, if available, e.g. BRL, ARDEC, NADC.

11. SPONSOR/MONITOR'S REPORT NUMBER(S). Enter report number as assigned by the sponsoring/ monitoring agency, if available, e.g. BRL-TR-829; -215.

12. DISTRIBUTION/AVAILABILITY STATEMENT. Use agency-mandated availability statements to indicate the public availability or distribution limitations of the report. If additional limitations/ restrictions or special markings are indicated, follow agency authorization procedures, e.g. RD/FRD, PROPIN, ITAR, etc. Include copyright information.

13. SUPPLEMENTARY NOTES. Enter information not included elsewhere such as: prepared in cooperation with; translation of; report supersedes; old edition number, etc.

14. ABSTRACT. A brief (approximately 200 words) factual summary of the most significant information.

15. SUBJECT TERMS. Key words or phrases identifying major concepts in the report.

16. SECURITY CLASSIFICATION. Enter security classification in accordance with security classification regulations, e.g. U, C, S, etc. If this form contains classified information, stamp classification level on the top and bottom of this page.

17. LIMITATION OF ABSTRACT. This block must be completed to assign a distribution limitation to the abstract. Enter UU (Unclassified Unlimited) or SAR (Same as Report). An entry in this block is necessary if the abstract is to be limited.

Final Report on

INVESTIGATION OF IONOSPHERIC TURBULENCE AND WHISTLER WAVE INTERACTIONS WITH SPACE PLASMAS

Space Plasmas
(FA9550-09-1-0391 for the period of June 1, 2009 – May 31, 2012)

1. Introduction

We report on AFOSR-sponsored research entitled "Investigation of Ionospheric Turbulence and Whistler Wave Interactions with Space Plasmas" (FA9550-09-1-0391 for the period of June 1, 2009 –August 31, 2012). It includes two parts: (1) naturally occurring and radio wave-induced large-and medium-scale ionospheric turbulence, and (2) whistler wave-generated short-scale ionospheric turbulence. Several journal and conference papers and students' Ph.D./M.S./B.S. theses have resulted from these research projects. We present the research results in order below.

2. Large- and Medium-scale Ionospheric Turbulence

Two types of large- and medium-scale ionospheric turbulence are discussed separately, namely, (a) anomalous heat source-induced acoustic gravity waves (AGW), and (b) HF radio wave-excited large plasma sheets. Anomalous heat sources can occur naturally to generate heat waves. They produce temperature gradients as the sources for the generation of acoustic gravity waves, as we observed at Arecibo Observatory [R. Pradipta, M.S. Thesis, M.I.T., 2008]. Besides, temperature gradients resulted from HF wave-depleted magnetic flux tubes were inferred from our earlier ionospheric HF heating experiments conducted at Arecibo Observatory, before the Arecibo HF heater was damaged by Hurricane Georges in 1998 [Lee et al., GRL,1998a]. Based on these Arecibo experiments, we have conducted a series of HF heating experiments at Gakona, Alaska to simulate anomalous heat source-excited acoustic gravity waves (AGWs) [R. Pradipota, Ph.D. Dissertation, M.I.T., 2012; Pradipta and Lee, 2012].

In our earlier Arecibo experiments large-scale plasma sheets in the form of parallel plate waveguides were detected by 430 MHz incoherent scatter radar [Lee et al., 1998b]. However, we could not investigate this intriguing phenomenon further, because the Arecibo heater was subsequently dismantled after its damage by the hurricane. Fortunately, we have been able to conduct ionospheric HF heating experiments at Gakona, Alaska ever since. Extensive diagnostic instruments are available to us in our Gakona experiments, including digisonde, MUIR radar at 446 MHz, magnetometers, riometer, GPS receivers, as well as our own VLF receiving system, All Sky Imaging System (ASIS), and GeoMagnetic Observatory System (GMO). We then have detection of HF heater-induced large plasma sheets, using MUIR radar and GPS satellites [Cohen et al,, 2010; Pradipta and Lee, 2012].

2.1. Naturally Occurring Acoustic Gravity Waves (AGWs)

A series of highly-structured ionospheric plasma turbulence was observed over Arecibo on the nights of 22/23 and 23/24 July, 2006. Incoherent scatter radar (ISR) measurements by Arecibo radar, airglow measurements using MIT PSFC's all-sky imaging system (ASIS), together with TEC measurements from GPS satellite network provide well-integrated diagnostics of turbulent plasma conditions. Two kinds of turbulent structures were seen as slanted stripes and filaments/quasi-periodic echoes on the range-time-intensity (RTI) plots of radar measurements. Detailed analyses of radar, airglow, and GPS data allow us to determine the drift velocity/direction, the orientation/geometry, and the scale lengths of these plasma turbulence structures. They are large plasma sheets with tens of kilometer scale lengths, moving in the form of traveling ionospheric disturbances (TIDs) southward within the meridional plane or westward in zonal plane at tens of meter per second. The signatures of observed TIDs indicate that they were triggered by internal gravity waves that had reached the altitudes of ionospheric F region. All possible sources producing gravity waves have been examined. We rule out solar/geomagnetic conditions which were quiet, and the atmospheric weather anomalies which were absent, during the period of time for our experiments. It is found that the heat wave fronts, which occurred in US, were plausible sources of free energy generating intense gravity waves and triggering large plasma turbulence over Arecibo. In other words, anomalous heat sources can be responsible for the occurrence of intense space plasma turbulence all over the world. The reported research suggests that global warming may affect the space weather conditions significantly. Further GPS data analysis has verified some predictions based on our current research outcomes [R Pradipta, M.S. Thesis, M.I.T., 2008; Pradipta et al., 2012]. Simulation experiments have been conducted at Gakona, Alaska using the powerful High-frequency Active Auroral Research Programs (HAARP) heating facility, to generate gravity waves for the controlled study of concerned intriguing phenomenon. The important results are briefly discussed below.

2.2. Generation of Acoustic Gravity Waves Using HF Heater

Following the research discussed in the previous section, we have investigated the potential role played by large-scale anomalous heat sources (e.g. prolonged heat wave events) in generating acoustic-gravity waves (AGWs), which might trigger widespread plasma turbulence in the ionosphere. The main hypothesis is that, the thermal gradients associated with the heat wave fronts could act as a source of powerful AGW to trigger ionospheric plasma turbulence over extensive areas. In our investigations, first we examined the case study of the summer 2006 North American heat wave event, using GPS-derived total electron content (TEC) data over the North American sector. It revealed quite noticeable increase in the level of daily plasma density fluctuations during the summer 2006 heat wave period. Comparison with the summer 2005 and summer 2007 data further confirms that the observed increase of traveling ionospheric disturbances (TIDs) during the summer 2006 heat wave period was not simply a regular seasonal phenomenon. Furthermore, a series of field experiments had been carried out at the High-frequency Active Auroral Research Program (HAARP) facility in order to physically simulate the process of AGW/TID generation by large-scale thermal gradients in the ionosphere. In these ionospheric HF heating experiments, we create some time-varying artificial thermal gradients at an altitude of 200-300 km above the Earth's surface, using vertically-transmitted amplitude-modulated O-mode HF heater waves. In our experiments, a number of radio diagnostic instruments had been utilized to detect the characteristic signatures of heater-generated AGW/TID, including MUIR radar, digisonde generated ionograms and skymaps, and GPS/LEO satellites. We have been able to obtain affirmative indications that some artificial AGW/TID can indeed radiate out of the HF wave

heated plasma volume during the HAARP-AGW experiments. Based on the experimental evidence, we can conclude that it is certainly quite plausible for large-scale thermal gradients associated with severe heat wave events to generate AGW, which can subsequently cause widespread ionospheric plasma turbulence in Earth's environment. See the details of attached R. Pradipta, Ph.D. Dissertation, M.I.T., 2012 and Pradipta and Lee, 2012(a) as Appendix (A) and Appendix (B), respectively.

2.3. Ionospheric Ducts Generated by HF Heater Waves

We report an investigation of ionospheric ducts having the shape of large plasma sheets, generated by vertically transmitted HAARP HF heater waves in several experiments conducted in Gakona, Alaska. Theory predicts that O-mode heater wave-created ionospheric ducts form parallel-plate waveguides within the meridional plane, and those generated by the X-mode heater waves are orthogonal to the meridional plane. Our theoretical prediction is supported by measurements of GPS data, ionosonde data (namely ionograms), range–time–intensity (RTI) plots of UHF and HF backscatter radars, as well as magnetometer data analyses. When these plasma sheets experienced **E**×**B** drifts, they were intercepted by the HAARP UHF radar and seen as slanted stripes in the RTI plots. See the details of attached paper by J.A. Cohen et al. [2010] as Appendix C.

Presented in Appendix D is our investigation of solar powered microwave transmission for communications and remote sensing. A solar powered microwave transmission system is proposed for remote sensing and communications purposes [Whitehurst et al., 2012a]. We present in this IEEE paper (1) a proof of concept to operate solar powered microwave transmission, and (2) investigation of microwave interactions with atmospheric plasmas. In this conceptualized system, a solar thermophotovoltaic system is considered to produce direct current electricity, which is then converted to microwaves. The results from these simulations provide insight on how to produce an economically and environmentally conscience energy source, that can be used for communication and remote sensing applications. However, it is expected that microwaves may interact with ionospheric plasmas, primarily, in the E region to induce large scale fluctuations in plasma density and geomagnetic fields with threshold wave electric field intensities of ~ 1 V/m. After we determine the instability thresholds, we can use them to set up the safe operation range of solar powered microwave transmission. As discussed in Appendix E by Whitehurst et al. [2012b], filament-type of ionospheric plasma turbulence can be produced primarily, in the E region by the ground-based microwave transmission system. Electron collisions play key roles in the generation of large scale fluctuations in ionospheric plasma density and geomagnetic fields via a thermal filamentation instability. Possible radar detection of microwave-induced ionospheric plasma effects has been planned for our future Arecibo experiments in Puerto Rico [Whitehurst and Lee, 2013].

3. Short-scale Ionospheric Turbulence

3.1. Arecibo Experiments with NAU Transmitter

We have been conducting whistler wave injection experiments at Arecibo Observatory, Puerto Rico, using the Naval transmitter (code-named NAU) located nearby at Aquadilla, to radiate VLF waves at 40.75 kHz. These experiments are aimed at the controlled study of whistler wave interactions with ionospheric plasmas [Labno et al., JGR, 2007] and inner radiation belts at L = 1.35 [Pradipta et al., GRL, 2007]. The ionospheric plasma effects caused by NAU transmission can be analyzed from Arecibo-radar measured enhanced plasma lines. While plasmas line enhancement occurs in F region due to 40.75 kHz whistler wave interactions with ionospheric plasmas [Labno et al., JGR, 2007], energetic electrons precipitated by whistler waves from inner radiation belts cause plasma line enhancement in E region. From the backscatter radar operation, if plasma lines arise from radar-detected beam modes associated with downward streaming electrons, then the preferentially detected plasma waves are expected to yield frequency-upshifted plasma lines due to the Doppler effect. However, as shown in our JASTP paper by Rooker et al. [2012a] given in Appendix F, enhanced plasma lines with frequency-downshifted spectra were exclusively measured in our summer 2008 experiments. The characteristic features of these frequency-downshifted plasma lines are very different from those of frequency-upshifted plasma lines observed in our earlier Arecibo experiments [Labno et al., JGR, 2007]. A new mechanism to understand this intriguing phenomenon and to explain how NAU-launched whistler waves can accelerate ionosphere electrons upward along the Earth's magnetic field is addressed in [Rooker et al., 2012a].

3.2. Gakona Experiments Using Beat Wave Technique

In Appendix G we report on the development of beat wave technique in our HAARP experiments conducted in the past two years [Rooker et al., 2012b], which extends our Arecibo experiments for the controlled study of whistler wave interactions with ionospheric plasmas and outer radiation belts at L = 4.6. This work focuses on the beat wave generation of VLF waves in the frequency range of 2 kHz to 42.5 kHz, using two HF radio waves. This technique can generates VLF whistler waves much more effectively than the conventional HF wave-modulation of electrojet currents. These beat wave-generated waves can propagate into the so-called radiation belts to interact with trapped energetic charged particles and precipitate them into the lower ionosphere. This technique can provide a method to clean hazardous charged particles in space environment for satellite remediation. Ion line measurements were made in our HAARP experiments by MUIR radar operated at 446 MHz. As shown in Appendix G [Rooker et al., 2012b], the new mechanism proposed by Rooker et al. [2012a] plays a dominant role in whistler wave interactions with ionospheric plasmas in turbulent plasma conditions.

Next given in Appendix H are results of Gakona experiments conducted in summer 2011 to verify our theoretical formulation of the coupling mechanism(s) for whistler wave generation [Kuo et al., 2012]. In brief, summer nighttime and daytime VLF wave generation experiments were conducted

on July 25 and July 27, 2011, respectively, using two CW HF X-mode waves with eleven VLF frequency differences from 2 to 21.5 kHz. The background magnetic variations were at comparable levels, except for that in the daytime experiment the D region absorption was significant and increasing and the number of the ionogram echoes was decreasing in the later time period. VLF signals were detected from 2 to 7.6 kHz in both experiments, showing an inverse frequency dependence of intensity, although signal intensity (except at 5.5 kHz) detected at nighttime was stronger than the corresponding one detected in the daytime before observing a decreasing in the ionogram echoes. However, VLF signals from 11.5 to 21.5 (except at 19.6 kHz) were also generated in the daytime experiment concurrent with a decreasing in the O-mode ionosonde echoes from 2 to 4 MHz. The concurrence of a decreasing in the ionogram echoes, the unexpected generation of VLF waves at higher frequencies, and the increasing D region absorption throughout the experiment may be explained by the generation of large scale density irregularities, which scatter the ionosonde signals as well as couple with the modulated electrojet to generate whistler waves.

Finally presented is Appendix I is a review paper accepted for publication entitled "Whistler Wave-induced Ionospheric Plasma Turbulence: Source Mechanisms and Remote Sensing". We report a series of experiments conducted at Arecibo Observatory in the past, aimed at the investigation of 40.75 kHz whistler wave interactions with ionospheric plasmas and the inner radiation belts at L = 1.35. The whistler waves are launched from a Naval transmitter (code-named NAU) operating in Aguadilla, Puerto Rico at the frequency and power of 40.75 kHz and 100 kilowatt, respectively. Arecibo radar, CADI, and optical instruments were used to monitor the background ionospheric conditions and detect the induced ionospheric plasma effects. Four-wave interaction processes produced by whistler waves in the ionosphere can excite lower hybrid waves, which can accelerate ionospheric electrons. Furthermore, whistler waves propagating into the magnetosphere can trigger precipitation of energetic electrons from the radiation belts. Radar and optical measurements can distinguish wave-wave and wave-particle interaction processes occurring at different altitudes. Electron acceleration by different mechanisms can be verified from the radar measurements of plasma lines. To facilitate the coupling of NAU-launched 40.75 kHz whistler waves into the ionosphere, we can rely on naturally occurring spread F irregularities to serve as ionospheric ducts. We can also use HF wave-created ducts/artificial waveguides, as demonstrated in our earlier Arecibo experiments and recent Gakona experiments at HAARP. The newly constructed Arecibo HF heater will be employed in our future experiments, which can extend the study of whistler wave interactions with the ionosphere and the magnetosphere/radiation belts as well as the whistler wave conjugate propagation between Arecibo and Puerto Madryn, Argentina.

Appendix A. Summary of R. Pradipta's Ph.D. Dissertation, MIT, 2012

Generation of Acoustic-Gravity Wave in Ionospheric HF Heating Experiments: Simulating Large-Scale Natural Heat Sources

MIT Department of Nuclear Science and Engineering
Doctoral Thesis Defense

Rezy Pradipta

29 August 2012

1 Introduction

In the modern era, our radio communication and navigation systems tend to rely more heavily on space science and technology. Consequently, a thorough understanding on various aspects of space plasma environment and space weather is quite crucial for us in order to ensure that these systems run and function properly. There are in fact many types of adverse space environment scenario that one should be aware of. For example, a severe turbulence in the ionospheric plasma layer could potentially disrupt short wave radio communications and might even affect the accuracy of GPS navigation system. In the long run, we ultimately hope to be able to mitigate the effects of such space plasma turbulence, so that we can maintain reliable communication and navigation capabilities under any space weather condition.

In this thesis, we focus on a certain type of ionospheric plasma turbulence known as traveling ionospheric disturbances (TIDs), which is caused by acoustic-gravity waves (AGWs) in the upper atmosphere. More specifically, we are considering the possibility for powerful AGWs to be generated by large-scale anomalous heat sources (e.g. heat wave events) that might subsequently trigger intense TIDs over an extensive geographical region.

Essentially, this investigation put an earlier speculation [*Pradipta*, MS Thesis 2007] to the test. During the considerably severe and prolonged summer 2006 heat wave event in North America, intense TIDs were observed over Arecibo, Puerto Rico, for several consecutive days of our radar and optical observations there. It was later speculated that these TIDs might have been triggered by AGWs generated by the advancing thermal fronts associated with the heat wave in the mainland United States. In short, the main goal of this doctoral thesis work is to obtain a more definitive evidence that would demonstrate the plausibility of AGW generation by large-scale natural thermal fronts.

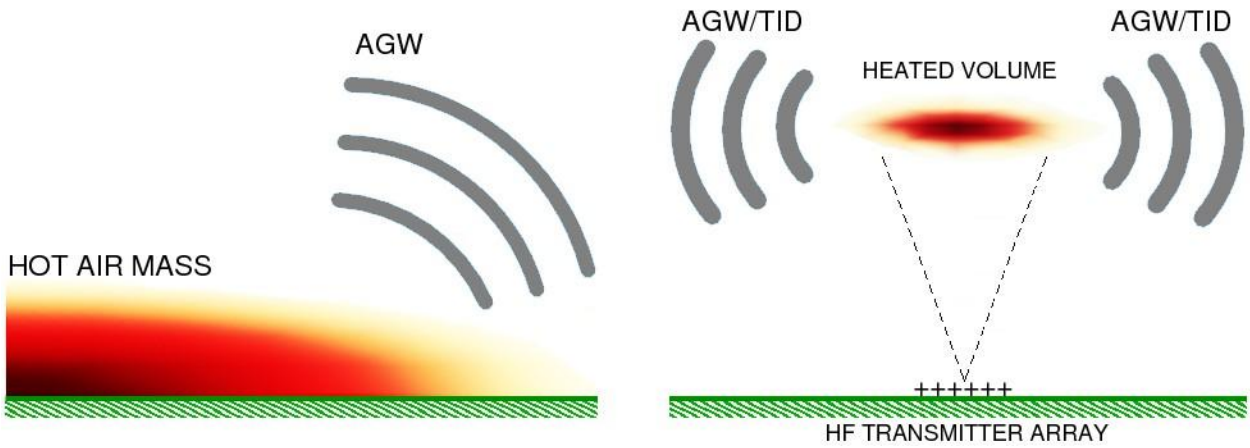

Figure 1: The suspected natural AGW excitation during a heat wave event (left). The basic concept of an ionospheric RF heating experiment to simulate AGW/TID excitation by large-scale thermal gradients (right). Note that the diagrams are not to scale.

This investigation is roughly divided into two main parts: (1) an examination on the level of ionospheric disturbances during natural heat wave events, and (2) a series of field experiments on the controlled study of AGW generation in the ionosphere using high-power radio transmitter. The first part of this investigation looks for any correlation between large-scale heat wave event and increased TID activity, while the second part basically attempts to demonstrate the causal relation in a relatively smaller scale.

In the first part of our investigation, we are using the summer 2006 North American heat wave event as a case study. For this case study, we examined the GPS-derived total electron content (TEC) data over the North American sector to monitor the level of ionospheric disturbances in this area. A significant increase in the level of TID activity that happened promptly during the heat wave period would indicate that it is plausible for large-scale natural thermal fronts to generate powerful AGWs that could subsequently trigger some TIDs over the corresponding area — corroborating our earlier speculation.

In the second part of our investigation, we attempt to physically simulate the process of AGW generation due to large-scale thermal gradients. This controlled study of AGW generation is done in a specially-designed ionospheric HF heating experiment, where a high-power radio transmitter on the ground illuminates certain ionospheric plasma volume overhead to create a sinusoidally time-varying artificial thermal fronts directly at ionospheric heights. In this ionospheric heating experiment, we look for the AGW/TID that are being generated as a result of the modulated HF heating. Figure 1 illustrates the concept of this HF heating experiment in relation to the suspected natural phenomenon we are trying to simulate.

2 Heat Wave Event and Ionospheric Disturbances

As mentioned previously, the first part of our investigation will be about the observation of increased TID activity during the summer 2006 North American heat wave period. In this case study, we are using the worldwide GPS-TEC data from the MIT Haystack Observatory's Madrigal Database (accessible at http://madrigal.haystack.mit.edu/ for public use) to monitor the overall TID activity over the North American sector.

In brief, the procedures for our GPS-TEC data analysis and examination are as follows. We first start with the absolute vertical TEC values ($= \int n_e \, dz$ along vertical column) as a function of geographical latitude/longitude coordinate. At each latitude/longitude coordinate location, we then estimate the diurnal TEC variation and subtract it out from the absolute TEC data. For each day's data, we are now left with TEC perturbation (TECP) values as a function of geographical coordinate and time-of-day. Finally, we average this TECP values over the 24-hour period to obtain an indicator for the level of TID activity at a certain latitude/longitude coordinate location on a given day.

From our GPS-TEC data examination over the North American region, we found a slight but noticeable increase in the day-averaged TEC fluctuations during the summer 2006 heat wave period (15 July – 27 August 2006). It should be noted that geomagnetic condition was relatively quiet during that time period, and thus AGW/TID of auroral origin can be ruled out. Furthermore, comparison with the summer 2005 and 2007 data suggest that the aforementioned increase in TID activity during the summer 2006 heat wave period was not a regular seasonal phenomenon that recurs every summer.

The top panel of Figure 2 shows a thermal satellite imagery of the relatively prolonged and severe heat wave event over North America in the summer 2006 [image taken from NASA *Earth Observatory*, 2006]. Meanwhile, the bottom panel of Figure 2 shows a set of overlaid/stacked plots of the day-averaged DTECP values around coordinate 35°N & 80°W (facing the southeast side of the 2006 heat wave front) from the summer 2005-2007 data. The red line on the time axis marks the summer 2006 heat wave period, which also serves as a comparison period for the 2005 and 2007 data. Note that the tickmarks on the y-axis for these RMS DTECP datasets had been set equal to each other, in order to allow for a relatively easier visual comparison.

The observed increase in the TID activity during the summer 2006 North American heat wave event is a promising indication that the advancing thermal fronts associated with the heat wave could potentially act as a source of AGWs, which could subsequently trigger some TIDs over the region. This finding supports our earlier speculation and provides a good basis/motivation for the controlled study of AGW generation via ionospheric HF heating.

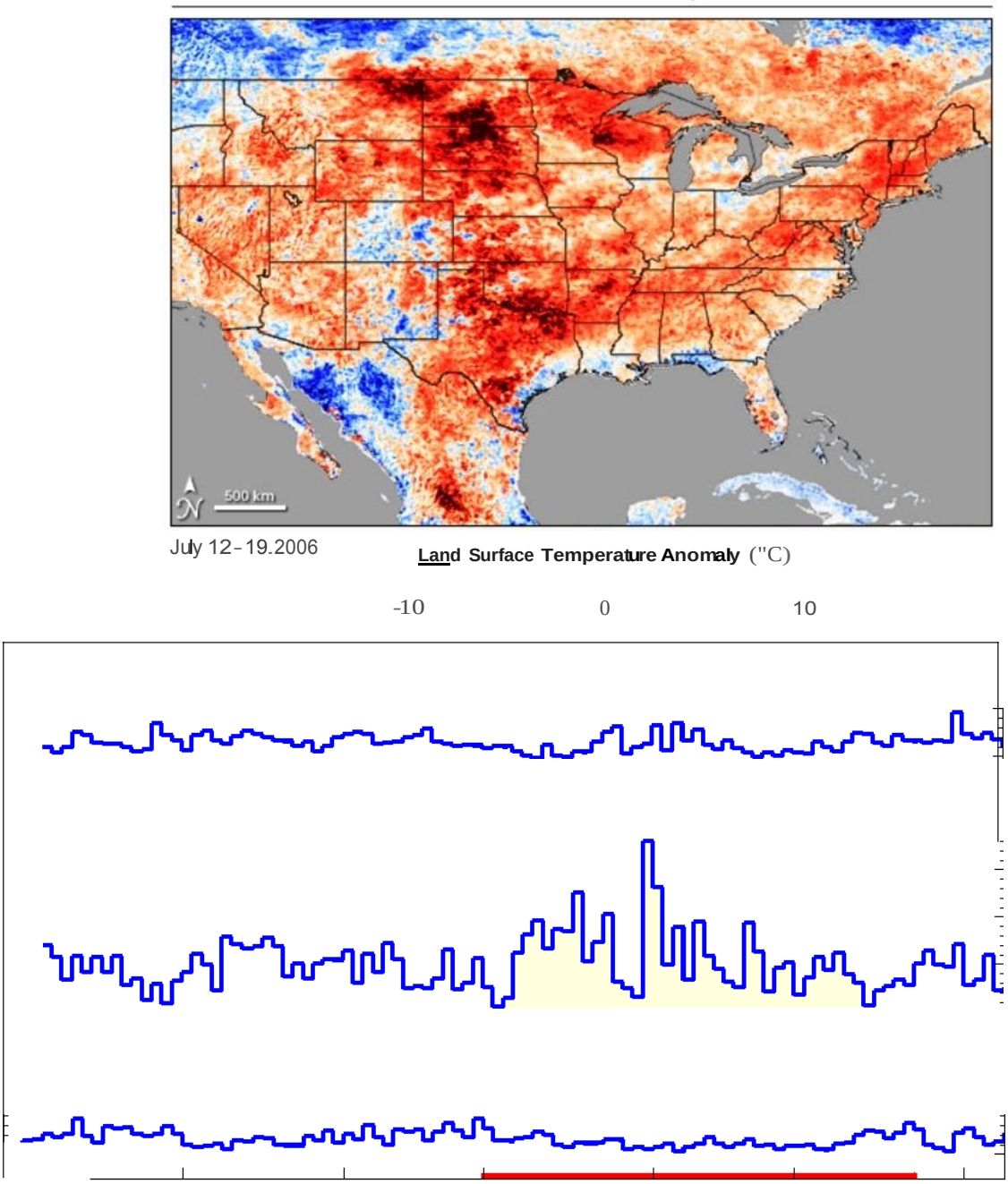

Figure 2: NASA's thermal satellite imagery of the summer 2006 North American heat wave event (top panel). Plots of the day-averaged DTECP amplitudes (around 35° N & 80°W) for summer months 2005-2007 (bottom panel). Red line marks the 2006 heat wave period.

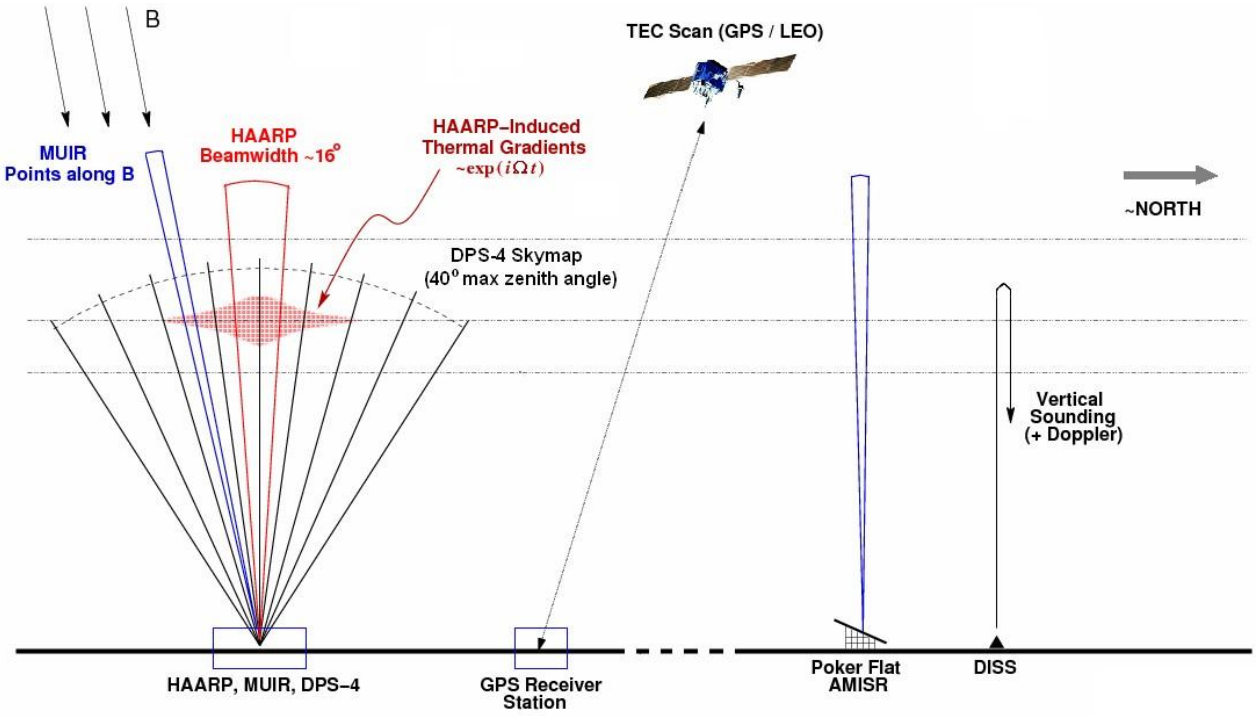

Figure 3: The basic experimental configuration of the HAARP-AGW experiment, depicting the most relevant diagnostic instruments.

3 The HAARP-AGW Experiment

In the second part of our investigation, we are looking for some further verification of our earlier hypothesis by trying to demonstrate a causal relation. In particular, we try to generate some artificial AGW/TID under a reasonably controlled condition in a series of ionospheric HF heating experiments. In the past four years or so, these field experiments had been conducted at the High-frequency Active Auroral Research Program (HAARP) facility located in Gakona, Alaska (latitude 62.4°N, longitude 145°W).

The general setup of the HAARP-AGW experiment is depicted schematically in Figure 3. The HAARP high-power HF transmitter illuminate a certain plasma volume overhead, and the transmitted power is sinusoidally varied as $\exp(i\Omega t)$. The modulation period has been chosen to be $T \equiv 2\pi/\Omega = 12$ minutes in order to ensure that we are in the appropriate frequency range for the (internal) gravity waves. Note also that the HAARP transmitter has a peak power capability of 3600 kW, and for the HAARP-AGW experiment we are transmitting heater waves in O-mode polarization.

In order to detect the artificial AGW/TID that are being generated as a result of the modulated HF heating, we are employing a number of radio diagnostic instruments. The

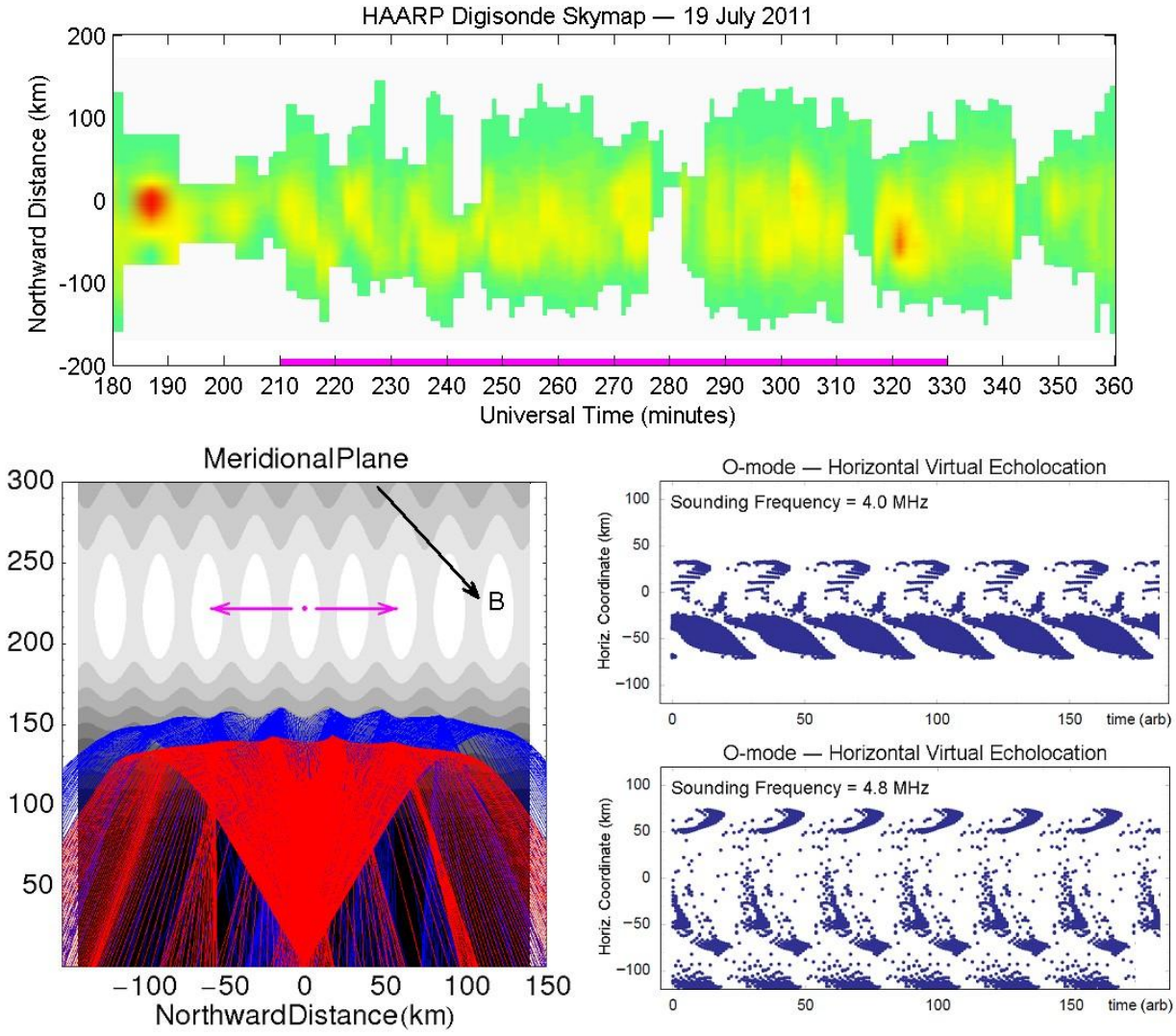

Figure 4: A skymap echolocation distribution-evolution plot from HAARP-AGW experiment conducted on 19 July 2011 (top panel). The purple line marks the time period for the experiment. The basic setup and a few representative results from our numerical ray tracing calculations to simulate the digisonde skymap data (bottom panels).

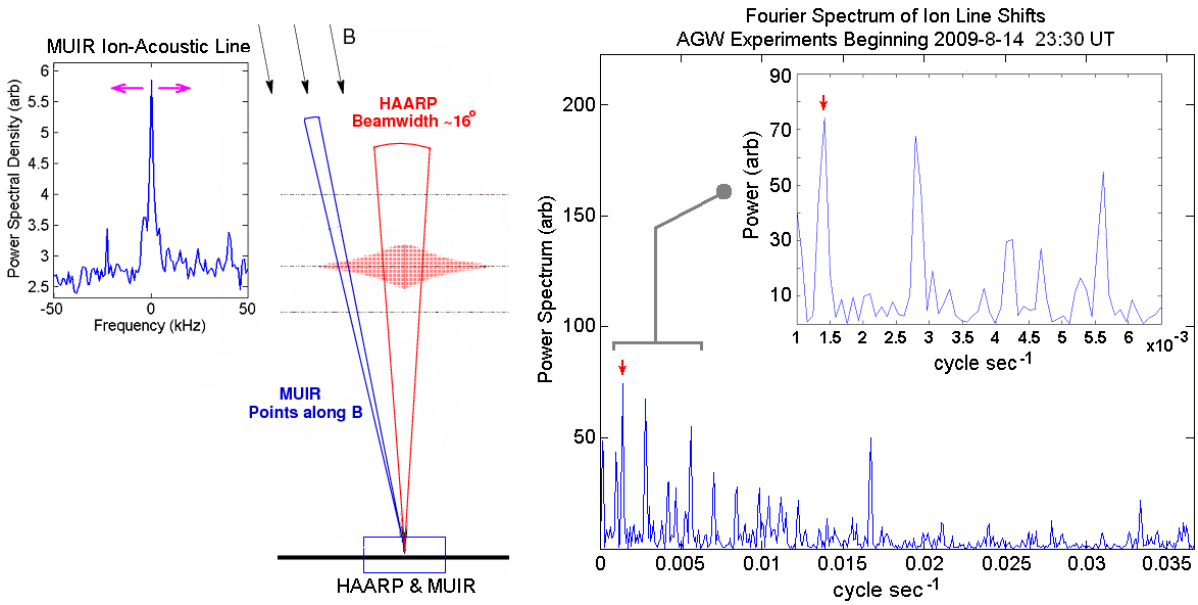

Figure 5: MUIR radar detection of heater-generated AGW/TID at HAARP. We found periodic time variation in the LOS velocity that matched the heating modulation period.

main strategy in the usage of these diagnostic instruments is to show that there are some traveling disturbances coming out from the heated plasma volume during/after the modulated HF heating. Furthermore, we want to show that these disturbances exhibit wave propagation properties (i.e. not static perturbations carried downstream by plasma drift) and they have some matching characteristics with the heating modulation cycle.

The top panel of Figure 4 shows some result from digisonde skymap measurements during a HAARP-AGW experiment carried out on 19 July 2011. We can see a few streaks of traveling disturbances coming out from the center toward the south, at an apparent propagation speed of approximately 160 m/s. In addition, we also ran some ray tracing calculations to try to resolve the lack of similar characteristic streaks on the north side of the digisonde. The setup and a few representative results are shown on the bottom panels of Figure 4. We found that, under ideal condition, the characteristic skymap signatures of point-source disturbances propagating radially away from the overhead location are generally much more recognizable on the south side — an overall agreement with the experimental observations.

Meanwhile, Figure 5 illustrates the usage of MUIR radar to detect HAARP-generated artificial AGW/TID. For the HAARP-AGW experiments, the MUIR radar beam points along the geomagnetic field lines — well outside of the heated plasma volume. If the heater-generated AGW/TID are being intercepted by the MUIR radar beam, then we can expect to see an oscillatory line-of-sight (LOS) velocity along the MUIR radar beam with the

Table 1: A comprehensive summary of the various multidiagnostic observations in support of the HAARP-AGW experiments 2008–2011.

Diagnostic Instrument	Summary of Main Findings[†]
LEO satellite pass	TECP ripple pattern, more-or-less symmetrical with respect to the center of heated region
GPS satellite pass	wavelike pattern in the TECP signal, with a rather pronounced peak in Fourier frequency spectrum
HAARP digisonde	cluster of skymap echoes with large Doppler shifts at both +ve/-ve polarities; radial-outward streak of traveling disturbances in the skymap echo distribution; additional set of oblique ionogram traces that appear/disappear periodically;
MUIR radar	periodic/oscillatory time variation of LOS velocity just outside of the heated region
Kodiak SuperDARN	AGW/TID signatures in the modulated pattern of ground-scatter echoes
Poker Flat AMISR	AGW/TID signatures overhead the Poker Flat site after 2~3 hour time delay

[†]Targeted search for affirmative indications of AGW/TID being generated as a result of the modulated ionospheric RF heating.

same periodicity as the heating modulation cycle. Since the heating modulation period is $T = 2\pi/\Omega = 12$ minutes, we are expecting a periodic time variation in the Doppler shift of the MUIR ion-acoustic line at $f = 1/T \approx 1.39 \times 10^{-3}$ Hz. From the computed Fourier periodogram shown in Figure 5, we found a quite sharp peak at $f \approx 1.4 \times 10^{-3}$ Hz. This pattern is a good indication that some AGW/TID were intercepted by the MUIR radar beam as they propagated out from the heated plasma volume

Besides the digisonde skymap and MUIR radar data, we had also obtained a number of additional positive indications that AGW/TID are indeed being radiated out from the heated plasma volume during our HAARP-AGW experiments. A summary of the key results from all the available radio diagnostic instruments are listed in Table 1.

4 Summary and Conclusion

In conclusion, our investigation has provided us with a number of positive indications that it is quite plausible for large-scale natural thermal gradients to generate powerful AGWs that might subsequently trigger some TIDs. Furthermore, as a by-product of our investigation, we have also opened up a rather exciting new path of controlled generation of artificial AGW/TID in ionospheric HF heating experiments.

Certified by:

Prof. Min-Chang Lee
Former Head, PSFC Ionospheric Plasma Research Group
Thesis Supervisor

Prof. Manuel Martinez-Sanchez
Department of Aeronautics and Astronautics
Thesis Supervisor

Prof. Anne E. White
Department of Nuclear Science and Engineering
Thesis Supervisor

Appendix B.

Investigation of acoustic gravity waves created by anomalous heat sources: experiments and theoretical analysis

R Pradipta[1] **and M C Lee**[1,2]

[1] Space Propulsion Laboratory, Massachusetts Institute of Technology (MIT), Cambridge, MA 02139, USA
[2] Department of Electrical and Computer Engineering, Boston University, Boston, MA 02215, USA

E-mail: mclee@mit.edu

Received 23 July 2012
Accepted for publication 24 July 2012
Published xxx
Online at stacks.iop.org/PhysScr/T149/000000

Abstract
We have been investigating high-power radio wave-induced acoustic gravity waves (AGWs) at Gakona, Alaska, using the High-frequency Active Aurora Research Program (HAARP) heating facility (i.e. HF heater) and extensive diagnostic instruments. This work was aimed at performing a controlled study of the space plasma turbulence triggered by the AGWs originating from anomalous heat sources, as observed in our earlier experiments at Arecibo, Puerto Rico (Pradipta 2007 *MS Thesis* MIT Press, Cambridge, MA). The HF heater operated in continuous wave (CW) O-mode can heat ionospheric plasmas effectively to yield a depleted magnetic flux tube as rising plasma bubbles (Lee *et al* 1998 *Geophys. Res. Lett.* **25** 579). Two processes are responsible for the depletion of the magnetic flux tube: (i) thermal expansion and (ii) chemical reactions caused by heated ions. The depleted plasmas create large density gradients that can augment spread F processes via generalized Rayleigh–Taylor instabilities (Lee *et al* 1999 *Geophys. Res. Lett.* **26** 37). It is thus expected that the temperature of neutral particles in the heated ionospheric region can be increased. Such a heat source in the neutral atmosphere may potentially generate AGWs in the form of traveling ionospheric plasma disturbances (TIPDs). We should point out that these TIPDs have features distinctively different from electric and magnetic field (ExB) drifts of HF wave-induced large-scale non-propagating plasma structures. Moreover, it was noted in our recent study of naturally occurring AGW-induced TIDs that only large-scale AGWs can propagate upward to reach higher altitudes. Thus, in our Gakona experiments we select optimum heating schemes for HF wave-induced AGWs that can be distinguished from the naturally occurring ones. The generation and propagation of AGWs are monitored by MUIR (Modular Ultra high-frequency Ionospheric Radar), Digisonde and GPS/low-earth-orbit satellites. Our theoretical and experimental studies have shown that anomalous heat sources produced by, for example, global warming can become potential causes inducing extensive large-scale turbulence in the neutral atmosphere and space plasmas.

PACS number: 52.50.−b

(Some figures may appear in color only in the online journal)

1. Introduction

Over the last five years or so, we have been conducting experiments at Gakona, Alaska, using the High-frequency Active Aurora Research Program (HAARP) heating facility

(i.e. HF heater) and extensive diagnostic instruments to investigate radio wave-induced acoustic gravity waves (AGWs). This research was inspired by the following physical processes. The HF heater operated in continuous wave (CW) O-mode can heat ionospheric plasmas so effectively as to

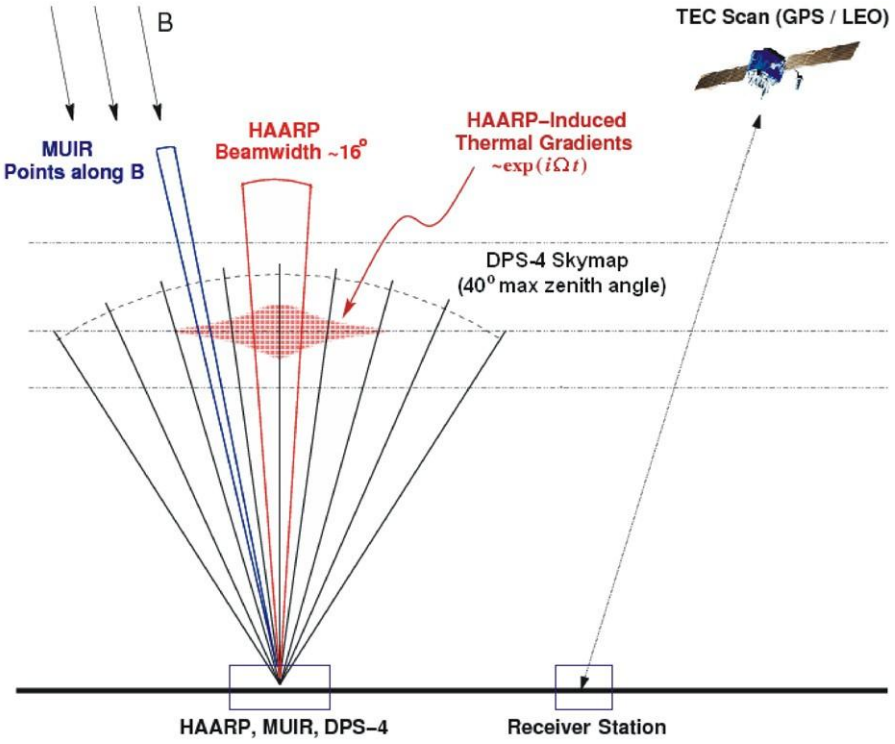

Figure 1. A schematic illustration of the basic geometry for the HAARP-AGW experiments.

yield the depleted magnetic flux tube. Two processes are responsible for the depletion of the magnetic flux tube. They are: (i) thermal expansion and (ii) chemical reactions caused by heated ions (Lee *et al* 1999). It is expected that the temperature of neutral particles in the heated ionospheric region can be increased, and temperature gradients can be consequently created. Such a heat source in the neutral atmosphere may potentially generate AGWs in the form of traveling ionospheric disturbances (TIDs) (Pradipta 2009, Pradipta and Lee 2011, Pradipta *et al* 2011). These TIDs have features distinctively different from electric and magnetic field (ExB) drifts of HF wave-induced large-scale non-propagating plasma structures. It was noted in our recent study of naturally occurring AGW-induced TIDs that only large-scale AGWs can propagate upward to reach higher altitudes. Thus, optimum heating schemes were selected for HF wave-induced AGWs to distinguish them from the naturally occurring ones. This work is conducive to the understanding of the mechanism(s) producing AGWs by natural anomalous heat sources (Pradipta 2007).

The experiments and theoretical analysis are presented as follows. A general overview of our AGW experiments is first given in section 2. In section 3, the details of the experiments described are given, including the survey of relevant geophysical parameters, heating schemes, diagnostic instruments and essential data from satellite and ground-based diagnostics. The discussions and conclusions are presented in section 4.

2. Experimental setup

Our experiments are aimed at physically simulating the possible generation of AGWs by large-scale thermal fronts

encountered in, e.g., naturally occurring heat wave events. We do so by creating some time-varying artificial thermal gradients at ionospheric heights through modulated HF heating. In these experiments, the high-power HF transmitter at the HAARP research facility injected O-mode heater waves vertically. The transmitted power varied sinusoidally with a modulation frequency Q below the Brunt–Vaisala frequency ω_g. We started from zero transmitter power at the beginning of the heating cycles. This heating scheme has been selected to ensure that we generate the (internal) gravity wave branch, which is most often responsible for triggering medium-scale as well as large-scale TIDs. Using the NRL MSIS-E atmospheric model, at altitude range
200–250 km where the foF2 peak is usually located for the ionosphere above HAARP, the Brunt–Vaisala period can be estimated to be $2\pi/\omega_g = 10$–11 min. Based on this estimate,
we decided to use a modulation period of $2\pi/Q = 12$ min in
our HAARP-AGW experiments.

The overall setup of the HAARP-AGW experiments is depicted schematically in figure 1. Using several different radio diagnostic instruments, we searched for characteristic signatures of AGW/TID during and after performing the sinusoidal heater power modulation. In addition, we intended to show that the observed AGW/TID indeed originated from the heated

region (not naturally occurring ones that simply happen to pass by) and they reflected some features similar to the heating modulation pattern.

As illustrated in figure 1, the HAARP heater transmitted high-power HF waves vertically with a beam width of ~ 16°. Thermal gradients in the form of $\exp(iQt)$ are expected to be induced. They are subsequently diagnosed by 446 MHz MUIR (Modular UHF Ionospheric Radar) radar, Digisonde and GPS/LEO (low-earth-orbit) satellites. MUIR radar was beamed along the Earth's magnetic field lines to record ion

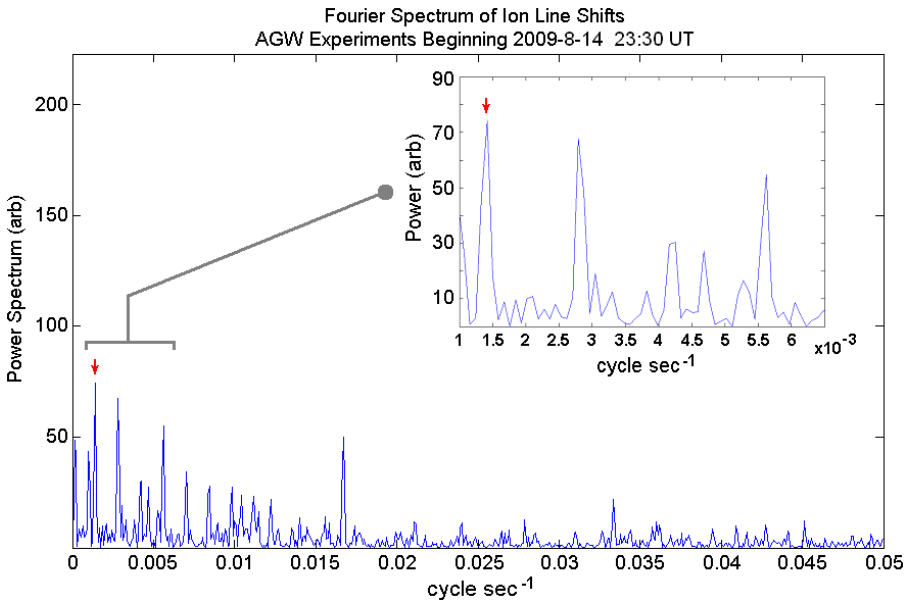

Figure 2. A set of Fourier periodograms of the LOS velocity time series as recorded by the MUIR radar during the HAARP-AGW experiments on 14 August 2009.

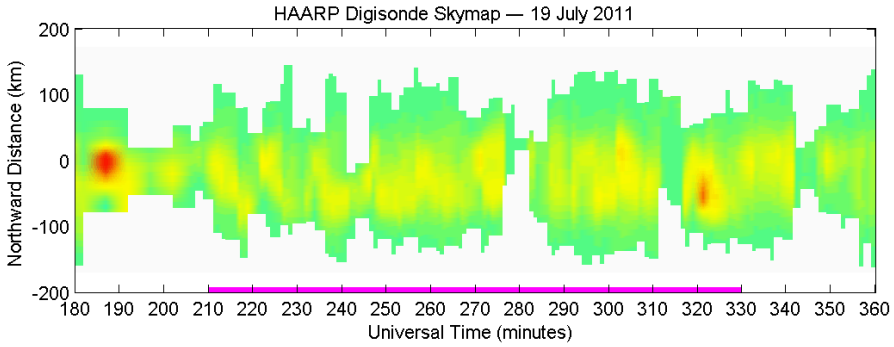

Figure 3. The time evolution plot of the spatial distribution of Digisonde skymap echolocations projected along the north–south plane.

lines. The Digisonde was operated to inject swept-frequency HF diagnostic waves with a maximum zenith angle of 40°, to produce skymaps. Several GPS receiving systems deployed near the HAARP heating facility were used to monitor total electron content (TEC) variations in the HF-heated ionospheric plasma regions.

3. Experimental results

Based on the analysis of the data recorded from aforementioned diagnostic instruments, we have obtained good indications that the AGW/TID had been generated out of the HF wave-heated plasma region, as a result of modulated O-mode heating with a modulation frequency $Q < \omega_g$.

3.1. MUIR ion line measurements

The first experimental evidence to discuss comes from the so-called ion line measurements of MUIR operating at

446 MHz. In the HAARP-AGW experiments, the MUIR radar beam points along the background magnetic field, i.e. 15° from the vertical direction, well outside the HAARP-heated region. The MUIR provides basic line-of-sight (LOS) velocity measurements from the ion line spectra. Heater-generated AGW/TID would give rise to an oscillating LOS velocity with the same periodicity as the heating modulation pattern. A set of Fourier periodogram from the MUIR LOS velocity time series obtained during our experiments is shown in figure 2. It shows a strong peak at around 1.4 mHz (along with some harmonics up to 13 mHz or so), which corresponds to a periodicity close to our heating modulation period of 12 min.

3.2. Digisonde skymap measurements

Meanwhile, skymap measurements using the Digisonde showed that, during the modulated HF heating, the echo locations periodically shifted outwards radially from the center of the heated region. Such an echo-location-shift pattern is depicted in figure 3, where the purple line on the time axis marks the time period when we performed the AGW heating modulation cycle. In this case, we can see that the echo locations shifted outwards to 100 km in approximately 10 min—revealing a propagation speed estimate of $\sim$160 m s^{-1}. Furthermore, we also found that this radial shift is independent of the background plasma drift velocity, indicating some wave propagation features.

AGW/TIDs radiated away from the heated ionospheric plasma volume. In summary, based on the TEC scan measurements (with an approximately symmetric TECP pattern), we can estimate the propagation speed of AGW to be a few tens of $\mathrm{m\,s^{-1}}$. We note that AGW originated from the edge of the heated region, which is consistent with the expectation that thermal gradients are the driving source. Skymap measurements showed the radially propagating disturbances, in the direction opposite of the bulk plasma drift. The LOS Doppler measurements by UHF radar pointing outside of the heated plasma volume revealed periodic Doppler shifts with periodicity which matches the RF modulation cycle.

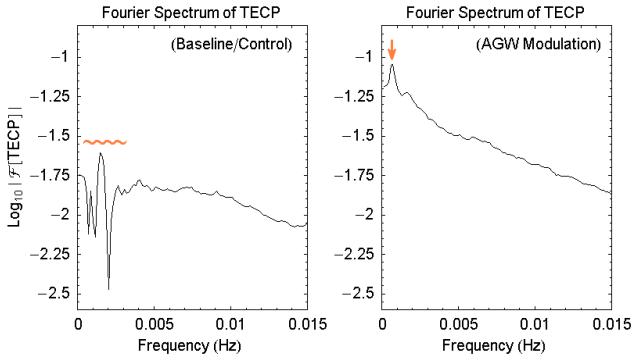

Figure 4. Computed Fourier frequency spectra of the GPS TECP signal, recorded in the HAARP-AGW experiment on 25 October 2008, at the baseline/control period and at the main period of interest.

In addition to ground-based radio measurements, we also have some TEC measurements from LEO and GPS satellite passes during our HAARP-AGW experiments.

3.3. GPS/LEO TEC measurements

For our experiment on 30 July 2008, 04:00–05:12 UTC, we had a LEO satellite pass scheduled over Gakona, AK immediately after a full set of AGW modulation cycle was completed. The satellite pass started from 05:02 UTC and lasted for about 15 min. At that time, we had just completed four cycles of heater power modulation. After removing the trend in the absolute TEC values, we obtain the total electron content perturbation (TECP) signal along the satellite's ionospheric piercing point trajectory. In the TECP data, we found some near-symmetric TECP ripple pattern around the center point of the heated region, indicating that AGW/TID wavefronts are coming radially out from the heated plasma volume.

Finally, GPS satellite passes also give us useful TEC measurements. However, note that the GPS satellite's piercing point moves considerably more slowly compared to the LEO satellite case. Hence, we cannot perform a rapid TEC scan using GPS satellite pass, but we can examine the Fourier frequency spectrum of the TECP time series recorded during the GPS satellite pass. As shown in figure 4, we examined the Fourier spectrum of the GPS TECP signal before and during/after the AGW modulation. We found quite a pronounced peak near the heating modulation frequency Q in the spectrum during/after the AGW modulation heating. In relative comparison, the spectra look rather flat during the control period before the AGW modulation had started.

4. Discussions and conclusions

We have presented some data recorded in our ionospheric HF heating experiments at Gakona, Alaska, aimed at simulating AGW excitation by an anomalous heat source. The data from satellite passes and ground-based radio diagnostic instruments have provided good indications that HF wave-induced

In conclusion, we have made steady progress in learning the role(s) of anomalous thermal fronts in triggering large-scale ionospheric plasma turbulence. This work simulates well the series of naturally occurring highly structured ionospheric plasma turbulence we observed over Arecibo in 2006. It was found that the heat wave fronts, which occurred in USA, were the plausible sources of free energy, generating intense gravity waves and triggering large plasma turbulence over Arecibo. In other words, anomalous heat sources can be responsible for the occurrence of intense space plasma turbulence all over the world. This is a large-scale source producing AGW in addition to tsunamis, which we reported earlier to cause global ionospheric plasma turbulence (Lee *et al* 2008).

Acknowledgments

This work was supported by AFOSR grant FA9550-09-1-0391. This paper was presented at the 3rd International Conference on 'Turbulent Mixing and Beyond', Abdus Salam International Centre for Theoretical Physics (ICTP), Trieste, Italy, 21–28 August 2010.

References

Lee M C, Klien E M C, Burke W J, Zhang A X, Riddolls R J, Kuo S P, Sulzer M P and Isham B 1999 Augmentation of natural ionospheric plasma turbulence by HF heater waves *Geophys. Res. Lett.* **26** 37

Lee M C, Pradipta R, Burke W J, Labno A, Burton L M, Cohen J A, Dorfman S E, Coster A J, Sulzer M P and Kuo S P 2008 Did Tsunami-launched gravity waves trigger ionospheric turbulence over Arecibo? *J. Geophys. Res.* **113** A01302

Lee M C, Riddolls R J, Burke W J, Sulzer M P, Klien E M C, Rowlands M J and Kuo S P 1998 Ionospheric plasma bubble generated by Arecibo heater *Geophys. Res. Lett.* **25** 579

Pradipta R 2007 *MS Thesis* MIT Press, Cambridge, MA

Pradipta R 2009 Controlled study of radiation belts and space plasma turbulence *PhD Thesis* MIT Press, Cambridge, MA

Pradipta R and Lee M C 2011 Large-scale ionospheric plasma turbulence generated by HAARP heater *SSRC Tutorial Lecture (Gakona, Alaska, 20 July)*

Pradipta *et al* 2011 Investigation of acoustic gravity waves created by anomalous heat sources: experiments and theoretical analysis *Int. Conf. on Turbulent Mixing and Beyond (Abdus Salam International Centre for Theoretical Physics (ICTP)) (Trieste, Italy, 21–28 August)*

Appendix C.

IOP PUBLISHING PHYSICA SCRIPTA

Phys. Scr. **T142** (2010) 014040 (7pp) doi:10.1088/0031-8949/2010/T142/014040

Generation of ionospheric ducts by the HAARP HF heater

J A Cohen[1], R Pradipta[1], L M Burton[1], A Labno[1], M C Lee[1,2], B J Watkins[3], C Fallen[3], S P Kuo[4], W J Burke[5], D Mabius[2] and B Z See[2]

[1] Massachusetts Institute of Technology, Cambridge, MA 02139, USA
[2] Boston University, Boston, MA 02215, USA
[3] University of Alaska Fairbanks, Fairbanks, AK 99775, USA
[4] New York University, Brooklyn, NY 11201, USA
[5] Air Force Research Laboratory, Hanscom AFB, MA 01731, USA

E-mail: mclee@mit.edu

Received 8 July 2010
Accepted for publication 23 August 2010
Published 31 December 2010
Online at stacks.iop.org/PhysScr/T142/014040

Abstract

We report an investigation of ionospheric ducts having the shape of large plasma sheets, generated by vertically transmitted HAARP HF heater waves in several experiments conducted in Gakona, Alaska. Theory predicts that O-mode heater wave-created ionospheric ducts form parallel-plate waveguides within the meridional plane, and those generated by the X-mode heater waves are orthogonal to the meridional plane. Our theoretical prediction is supported by measurements of ionosonde data (namely ionograms), range–time–intensity (RTI) plots of UHF and HF backscatter radars, as well as magnetometer data analyses. When these plasma sheets experienced **E × B** drifts, they were intercepted by the HAARP UHF radar and seen as slanted stripes in the RTI plots. This striking feature was also observed in our earlier experiments using the Arecibo UHF radar.

PACS numbers: 94.20.−y, 94.05.−a

(Some figures in this article are in colour only in the electronic version.)

1. Introduction

We have been conducting experiments in Gakona, Alaska to investigate the characteristic features of HAARP HF heater-induced large-scale ionospheric ducts (Cohen *et al* 2008) as well as short-scale plasma waves (Burton *et al* 2008). Depending on the polarizations (i.e. O-mode or X-mode) of the heater waves, these large-scale ionospheric plasma structures have different configurations. In brief, large-scale sheet-like ionospheric density irregularities can be excited within and orthogonal to meridional planes above Gakona by vertically injected O-mode and X-mode heater waves, respectively, as illustrated in figures 1 and 2 (Cohen *et al* 2008, Kuo *et al* 2009 and references therein). How these plasma sheets can affect ionosonde signals in the presence of distant plasma blobs, as delineated in figures 1 and 2, will be discussed in the next section.

These experiments were motivated by our earlier Arecibo experiments, wherein we observed HF heater-generated large plasma sheets (Lee *et al* 1998). Presented in figure 3 is a range–time–intensity (RTI) plot of Arecibo 430 MHz backscattered radar echoes, showing that large sheet-like plasma density irregularities were created by Arecibo O-mode HF heater waves within the meridional planes. When these plasma sheets experienced **E × B** drifts, they were detected by the Arecibo radar and were seen as slanted stripes in the RTI plots. These large plasma sheets, known as 'artificial ionospheric ducts' or 'waveguides', had successfully supported the US Navy Naval transmitter (codenamed NAU)-launched 28.5 kHz whistler waves to propagate between Arecibo, Puerto Rico and Trelew, Argentina along the $L = 1.35$ magnetic flux tube (Starks and Lee 2000, Starks *et al* 2001, Pradipta *et al* 2008). This work has important applications for radiation belt remediation

0031-8949/10/014040+07$30.00

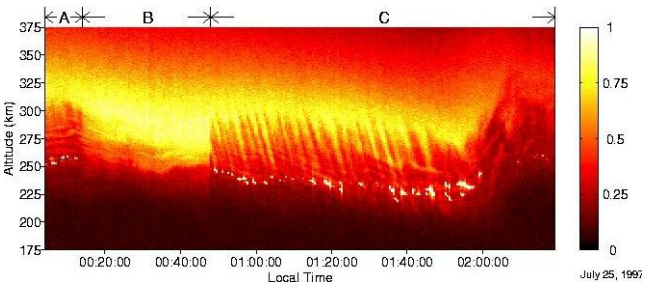

Figure 3. Arecibo radar detection of O-mode HF heater wave-created large plasma sheets (seen on the RTI plot as slanted stripes), from about 00:50 to 01:50 LT on 25 July 1997 (Lee *et al* 1998).

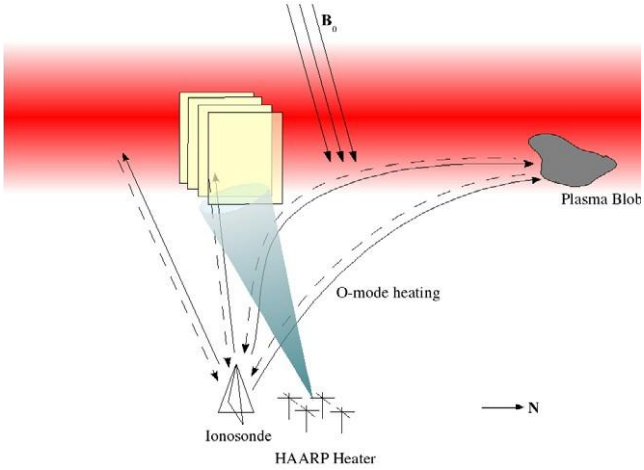

Figure 1. Large plasma sheets generated by O-mode HAARP heater waves within the meridional plane. Ionosonde signals can be bounced back by remote plasma blobs to propagate through those parallel-plate waveguides and recorded in ionograms.

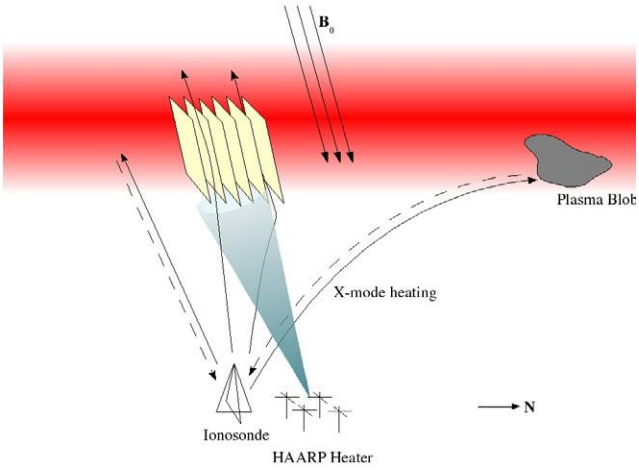

Figure 2. Large plasma sheets generated by X-mode HAARP heater waves are orthogonal to the meridional plane. Ionosonde signals transmitted near the zenith will be guided by these plasma sheets to propagate away. Thus they cannot be bounced back to appear in the ionograms. However, ionosonde signals transmitted at large angles from the zenith can still be reflected by remote plasma blobs and recorded in ionograms.

(Pradipta *et al* 2007) and whistler wave interactions with ionospheric plasmas (Labno *et al* 2007).

2. Detection of heater-excited large plasma sheets at the HAARP facility

Several diagnostic instruments have been used to detect HAARP heater-generated large plasma sheets, including an ionosonde, MUIR (Modular UHF Ionospheric Radar at 446 MHz), SuperDARN HF backscatter radar and magnetometers. The results are discussed as follows.

2.1. Digisonde measurements

We use a sequence of ionograms, displayed in figure 4, to discuss the effects of HF heater-excited plasma irregularities on signals transmitted from the HAARP ionosonde. In the

attached color code, O+ and O− denote the blueshifted and redshifted return echoes of ordinary ionosonde signals from the vertical direction, respectively. Similarly, X+ and X− denote the blueshifted and redshifted return echoes of extraordinary ionosonde signals from the vertical direction, respectively. Other colors denote echoes from the oblique direction (indicated by NNE, E, W, SSW, SSE, NNW) without Doppler information.

These representative ionograms were recorded during our experiments conducted on 21 August 2005 from 10:00 UT to 12:15 UT. Prior to our experiments, ionogram (a) (figure 4(a)) was recorded at 9:55 UT during the vertical transmission of ramped X-mode. The ionograms showed strong spread-F and ionosonde signals were reflected from the northward direction. Our experiments began with 3.16 MHz CW O-mode transmitted along the magnetic zenith. As soon as the heater was switched to this mode, a vertical stripe appeared around the heater frequency, affecting the blue northward traces (ionogram

(b)). This reduction in signal persisted throughout the O-mode heating. When the heater was turned off, the traces filled in again (ionogram (c)).

The heater was turned on at 11:05:30, transmitting 3.15 MHz CW X-mode vertically. A decrease in northward signal intensity was again seen, but was more pronounced this time (ionogram (d)). Changing the heater direction to the magnetic zenith did not make an appreciable difference (ionogram (e)), but increasing the heater frequency to 4.50 MHz at 11:35:30 altered the appearance of the ionograms. A vertical stripe appeared around the new heater frequency, but was narrower and bore greater resemblance to the first O-mode stripe in ionogram (b), centered in a narrow frequency range around the heater frequency (ionogram (f)). At this higher frequency, there was not a significant difference when we switched to CW O-mode, still transmitting at 4.50 MHz (ionogram (g)). Increasing the frequency once more and transmitting 6.80 MHz CW O-mode had no apparent effect on the ionogram traces and they filled back in quickly (ionogram (h)). When the heater was turned off, the traces remained essentially the same (ionogram (i)). We note that there was an apparent weakening of the X-mode trace on the ionograms when the heater began transmitting CW X-mode (ionogram (d)) and in fact this trace disappeared altogether after 5 min. However, when the heater was later switched to CW O-mode (ionograms (g) and (h)) and eventually turned off (ionograms (i)), the X-mode trace did become apparent

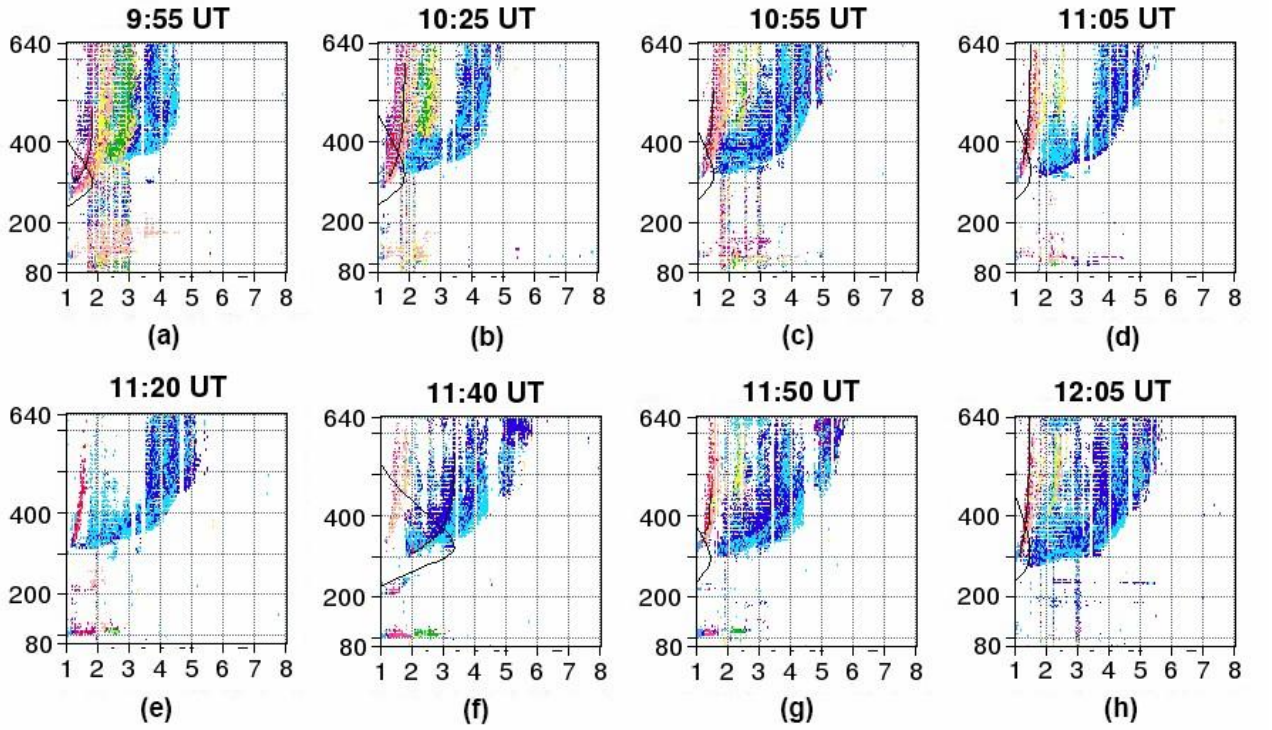

Representative ionograms from heating periods. The heater orientation is given as (azimuth, angle from zenith) in degrees.

(a) prior to experiments, ramped X-mode at (0,0)
(b) 3.16 MHz CW O-mode at (204,15)
(c) heater off
(d) 3.15 MHz CW X-mode at (0,0)
(e) 3.16 MHz CW X-mode at (204, 15)
(f) 4.50 MHz CW X-mode at (204, 15)
(g) 4.50 MHz CW O-mode at (204, 15)
(h) 6.80 MHz CW O-mode at (204, 15)
(i) heater off

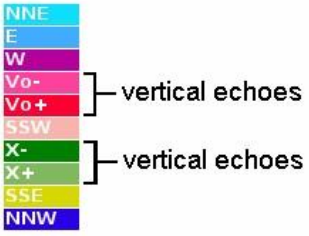

the others are oblique echoes

Figure 4. Ionograms recorded in HAARP experiments on 21 August 2005.

again. Thus, it is interesting to examine what effect the heater had on the X-mode trace in ionograms.

We expect that heater-excited small-scale and large-scale irregularities may scatter and duct ionosonde signals, respectively, and cause a loss in received signal near the heater frequency (Kuo *et al* 2009). This results in the appearance of broad vertical stripes in ionograms. While narrow stripes may be automatically taken out by the ionosonde software, namely automatic gain control (Reinisch 2009), the stripes in ionograms show rough edges, which are not characteristic of software-removed interference lines. In addition, we believe that heater-excited large plasma sheets are responsible for the reduction of northward signals in the ionograms. During the night of our experiments on 21 August 2005, a plasma blob was seen in total electron content (TEC) measurements to the north of HAARP (see figure 5), taken by a LEO receiver with the right geometry to produce a tomographic image of electron density over Alaska.

As shown in figure 1, CW O-mode heating produces sheet-like irregularities parallel to the meridional plane. Ionosonde signals that are refracted by the ionosphere may reach and be reflected by the density gradient created by the plasma blob. These reflected signals reaching the ionosonde are seen as blue northward traces. There existed some correlation between ionospheric structures such as plasma blobs and the intense northward traces. As illustrated in figure 2, CW X-mode heating produces sheet-like irregularities that are perpendicular to the meridional plane. In this scenario, the ionosonde signals that would otherwise be reflected by the plasma blob are ducted away or undergo scattering. This interpretation provides a plausible explanation regarding HAARP heater effects on the observed X-mode trace in concerned ionograms.

2.2. MUIR and SuperDARN radar measurements

The aforementioned effects of excited plasma density irregularities on HAARP digisonde have also been seen on

MUIR from 01:49 to 01:54 UT. When these plasma sheets experienced $\mathbf{E} \times \mathbf{B}$ drifts, they were intercepted by MUIR radar and are seen as slanted stripes in the RTI plots.

By contrast, the RTI plot of SuperDARN backscatter radar measurements that is displayed in figure 7 shows different aspects but expected features of plasma sheets, which were generated by vertically transmitted heater waves during our HAARP experiment on 27 February 2008. In these experiments Kodiak SuperDARN radar periodically scanned the region overhead HAARP (beam no. 8). The range is about 670 km for the SuperDARN beam to reach the heated ionospheric region above Gakona. It is seen from the RTI plot that SuperDARN signals weakened significantly when we changed the heating schemes from O-mode to X-mode. We have used black arrows in the RTI plot to show the significant reduction of radar echo occurring during CW X-mode operation. This feature is consistent with the

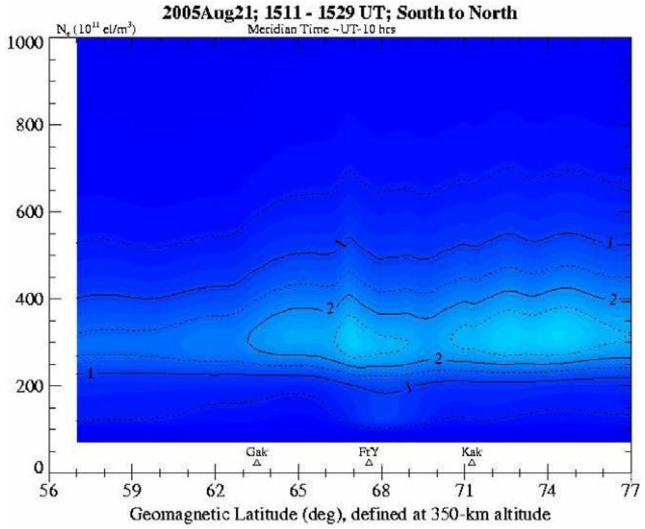

Figure 5. TEC measurements from LEO satellites over Alaska on 21 August 2008 from 15:11 to 15:29 UT.

the operation of MUIR and SuperDARN radar. MUIR is not as sensitive as the Arecibo radar. Thus, Arecibo radar measurements to generate RTI of electron density structures, as shown in figure 3, cannot be done by MUIR. However, the RTI plots of ion lines can be produced by MUIR. Displayed in figure 6 is such an RTI plot of MUIR ion line measurements recorded from 01:43:00 to 01:59:30 UT on 21 October 2009. It shows that three large sheet-like plasma density irregularities were created by HAARP O-mode HF heater waves within the meridional planes, and detected by

measurements using SuperDARN beam no. 2, which scanned the west side of the heated region to diagnose drifted away large plasma structures. That is, radar echoes from X-mode excited plasma structures were significantly weaker than those from O-mode excited structures. During the O-mode heating SuperDARN signals were bounced back by plasma sheets generated within the meridional plane, as shown in figure 1. By contrast, SuperDARN signals were forward-scattered by X-mode generated plasma sheets, which are orthogonal to the meridional plane as illustrated in figure 2. These scenarios explain reasonably well why the SuperDARN signals weakened significantly when we changed the heating schemes from O-mode to X-mode.

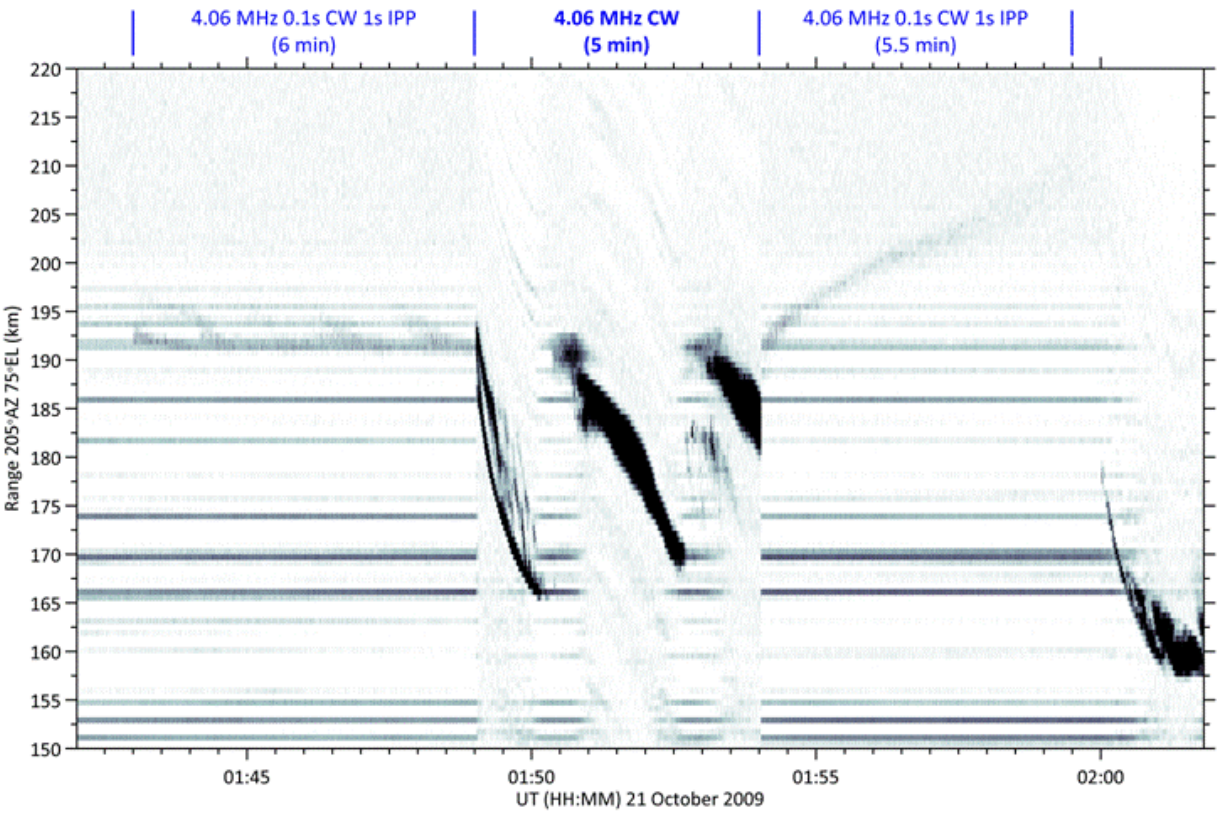

Figure 6. HAARP MUIR radar detection of O-mode HF heater wave-created large plasma sheets (seen on RTI plot as slanted stripes), from about 01:49 to 01:54 UT on 21 October 2009 (Fallen 2009).

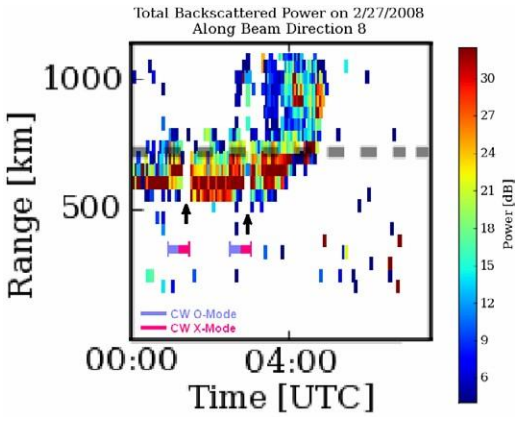

Figure 7. SuperDARN data recorded during CW O-mode and CW X-mode operation of the HAARP heater on 27 February 2008 for the investigation of the generation of large plasma sheets.

Figure 9. Simultaneous generation of plasma density fluctuations (δn) and geomagnetic fluctuations ($\delta \mathbf{B}$) in X-mode HF heating experiments (adapted from Lee and Kuo 1985).

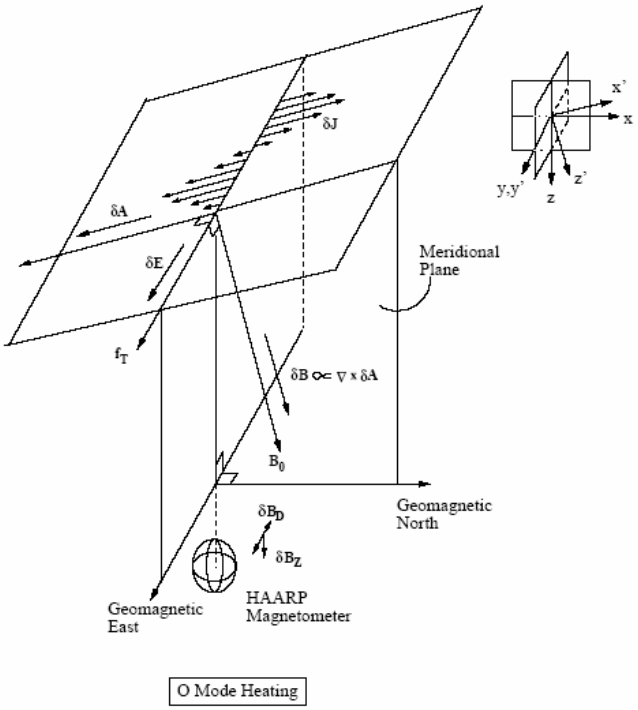

Figure 8. Simultaneous generation of plasma density fluctuations (δn) and geomagnetic fluctuations ($\delta \mathbf{B}$) in O-mode HF heating experiments (adapted from Lee and Kuo 1985).

2.3. Magnetometer measurements

HF heater wave-excited 'thermal filamentation instability' is responsible for the generation of ionospheric ducts in the form of large plasma sheets. A striking feature of this mechanism is the simultaneous generation of plasma density fluctuations (δn) and geomagnetic fluctuations ($\delta \mathbf{B}$) (Kuo *et al* 2009 and references therein). This physical process is briefly described as follows with the aid of figures 8 and 9 (adapted from Lee and Kuo 1985). Differential joule heating, resulting from the interactions of HF heater waves and excited high-frequency sidebands, yields a thermal pressure force ($\mathbf{f_T}$) on electrons across the geomagnetic field, pointing to the direction along the *y*-axis ('Geomagnetic East' as specified in figure 8 for O-mode heating) or along the *x*-axis ('Geomagnetic North

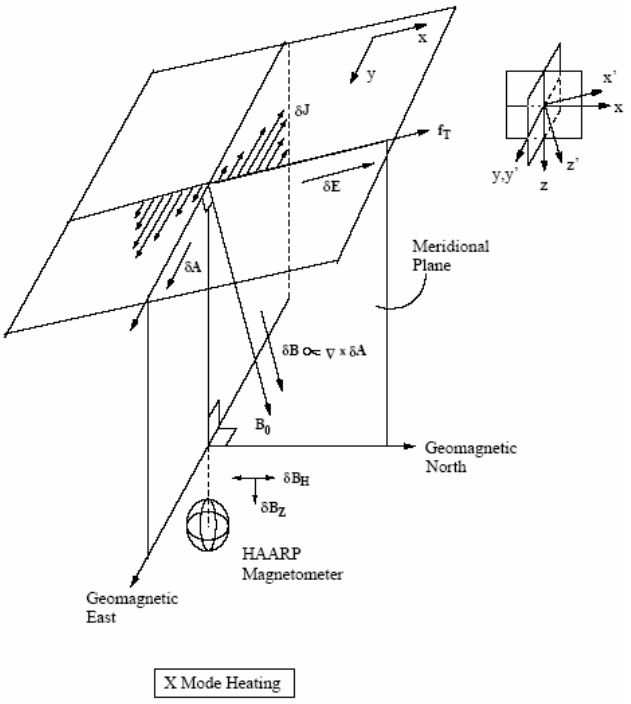

and upward' as specified in figure 9 for X-mode heating). Note that the thermal pressure force ($\mathbf{f_T}$) gives rise to electron density fluctuations (δn) with wave vectors ($\mathbf{k}$) pointing along the same direction. Hence, large plasma sheets are produced within (or orthogonal to) the meridional plane for the O-mode (X-mode) heating cases, as vividly illustrated in figures 8 and 9, respectively.

The thermal pressure force ($\mathbf{f_T}$) leads to an $\mathbf{f_T} \times \mathbf{B_0}$ drift motion of electrons and, consequently, induces a net electron drift current along the *x*-axis (as shown in figure 8 for O-mode heating) or along the *y*-axis (as shown in figure 9 for X-mode heating). The direction of the current is perpendicular to both the background magnetic field B_0 and the wave vector $\mathbf{k}$ of the excited plasma density irregularities. Therefore, magnetic field fluctuations ($\delta\mathbf{B}$) are excited along the background Earth's magnetic field ($\mathbf{B_0}$ designated as the *z*-axis) simultaneously with the density irregularities via the filamentation instability in both O- and X-mode heating processes. Note that the background geomagnetic field ($\mathbf{B_0}$) has a dip angle of 75.8°. Thus, it has three components (designated as $\mathbf{B_{0D}}$, $\mathbf{B_{0H}}$ and $\mathbf{B_{0Z}}$) along the East–West, North–South and downward directions, respectively. Therefore, the excited magnetic field fluctuations ($\delta\mathbf{B}$) also have the corresponding three components (designated as $\delta\mathbf{B_D}$, $\delta\mathbf{B_H}$ and $\delta\mathbf{B_Z}$).

Based on our theoretical analyses and illustrations of the simultaneous excitations of δn and $\delta\mathbf{B}$ in figures 8 and 9, aided by the delineation of sheet-like configurations in figures 1 and 2, we can expect that $\delta\mathbf{B_D}$ and $\delta\mathbf{B_Z}$ (or $\delta\mathbf{B_H}$ and $\delta\mathbf{B_Z}$) will be highly correlated in O-mode (or X-mode) heating experiments. While our detailed correlation study of these magnetic field fluctuations is in progress, we present in figure 10 the preliminary correlation analyses: the η_{HZ} of $\delta\mathbf{B_H}$

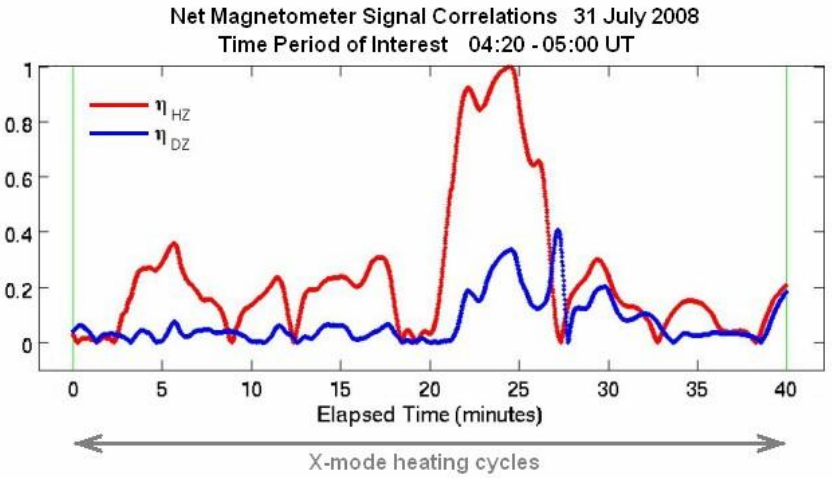

Plotted here is the net magnetometer signal correlations during a HAARP experiment.

We have an X-mode heating cycle:

1min ON - 30sec OFF for 7.5min
2min ON - 30sec OFF for 12.5min
3min ON - 30sec OFF for 17.5min
4min ON - 30sec OFF for 22.5min (*)

and we can see that the net H-Z correlation dominates over the net D-Z correlation, as expected.

(*) the heating cycle was truncated here

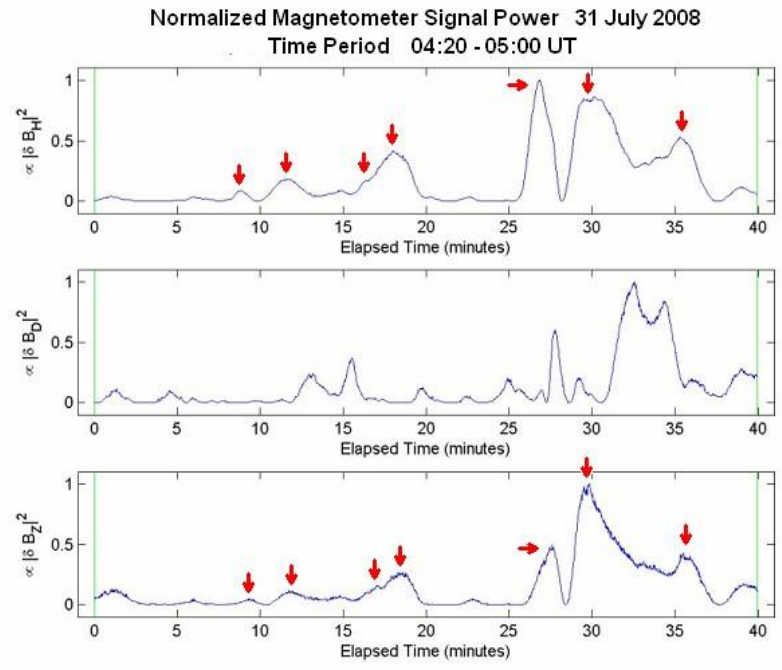

Furthermore, the plot of normalized power for each signal components also indicates that there was a very apparent correlation between the H- and Z-component of magnetometer signals.

Red arrows marked several noticeable features that can be seen present in both H- and Z-component signals.

Figure 10. Generation of large plasma sheets by X-mode heater waves supported by close correlation of excited $\delta\mathbf{B_H}$ and $\delta\mathbf{B_Z}$ (in red) (top

|

panel) and temporal power variation of $\mu|\delta B_H|^2$

|

and $\mu|\delta B_Z|^2$.

and $\delta\mathbf{B_Z}$ and the η_{DZ} of $\delta\mathbf{B_D}$ and $\delta\mathbf{B_Z}$ (top panel) and a plot of normalized power for $\delta\mathbf{B_D}$, $\delta\mathbf{B_H}$, and $\delta\mathbf{B_Z}$ (bottom panel).

It is seen in figure 10 that during the X-mode heating experiments carried out on 31 July 2008, the η_{HZ} of $\delta\mathbf{B_H}$ and $\delta\mathbf{B_Z}$ (in red) is much greater than the η_{DZ} of $\delta\mathbf{B_D}$ and $\delta\mathbf{B_Z}$ (in blue). This indicates that large plasma sheets orthogonal to the meridional plane were favorably excited by X-mode heater waves, as elaborated above. This is further supported

and communications, etc. These artificial ionospheric ducts are sheet-like large-scale plasma irregularities (δn), excited by O-mode and X-mode HF heater waves via thermal filamentation instabilities within and orthogonal to meridional planes, respectively. The configurations of these plasma sheets are supported by HAARP digisonde data (namely ionograms), as well as MUIR radar and SuperDARN radar signals due to reflection and scattering off the plasma

by the temporal variations of the normalized power $\mu|\delta B_H|^2$

2

sheets. When these plasma sheets experienced E ×

B drifts,

and $\mu|\delta B_Z|$, which show very similar patterns and features, as marked by red arrows in the bottom panel of figure 10.

3. Summary and discussions

We present the data recorded by several HAARP experi- ments in Gakona, Alaska aimed at investigating HF heater wave-induced ionospheric ducts for radiation belt remediation, controlled study of space plasma turbulence

they were intercepted by MUIR radar and are seen as slanted stripes in the RTI plots. A similar striking feature was seen in our Arecibo experiments. Our preliminary magnetometer data analysis confirms the characteristic features of the simultaneously excited geomagnetic field fluctuations ($\delta\mathbf{B}$), reflecting the geometry of the plasma sheets. For example, close correlation between $\delta\mathbf{B_H}$ and $\delta\mathbf{B_Z}$ is indeed found for X-mode generated plasma sheets, expected to be orthogonal to the meridional plane.

6

Acknowledgment

This work was supported by the HAARP under ONR grants N00014-07-1-0999 (MIT), ONR-N00014-10-1-0856 (NYU) and N00014-17-1-1082 (UAF). We thank Bodo Reinisch, Dima Paznukhov, Lee Snyder and Mike McCarrick for useful discussions and Bill Bristow and Jeff Spaleta for providing SuperDARN data. A part of this paper was presented by MCL as an invited lecture at the 2nd International Conference and Advanced School on 'Turbulent Mixing and Beyond', held at the International Centre for Theoretical Physics, 27 July–7
August 2009, Trieste, Italy.

References

Burton L M, Cohen J A, Pradipta R, Labno A, Lee M C, Batishchev
O, Rokusek D L, Kuo S P, Watkins B J and Oyama S 2008
Excitation and diagnosis of cascading Langmuir waves in ionospheric plasmas at Gakona, Alaska *Phys. Scr.* **T132**
014030
Cohen J A, Burton L M, Pradipta R, Labno A, Lee MC, Kuo S P, Watkins B J and Oyama S 2008 Ionospheric ducts and plasma waves induced by HF heater over Gakona *Proc. XXIX URSI General Assembly (Chicago, IL, 7–16 August 2008)*
Fallen C T 2010 Applications of a time-dependent polar ionosphere model for radio modification experiments *PhD Thesis* University of Alaska Fairbanks, Fairbanks

Kuo S P, Cheng W-T, Cohen J A, Pradipta R, Lee M C,
Kuo S S and Snyder A 2009 Simultaneous generation of large-scale density irregularities and geomagnetic pulsations via filamentation instability *Geophys. Res. Lett.*
36 L09107
Labno A, Pradipta R, Lee M C, Sulzer M P, Burton L M, Cohen J A, Kuo S P and Rokusek D L 2007 Whistler-mode wave interactions with ionospheric plasmas over Arecibo
J. Geophys. Res. **112** A03306
Lee M C and Kuo S P 1985 Simultaneous excitation of large-scale geomagnetic field fluctuations and plasma density irregularities by powerful radio waves *Radio Sci.*
20 539
Lee M C, Riddolls R J, Burke W J, Sulzer M P, Kuo S P and
Klien E M C 1998 Generation of large sheet-like ionospheric plasma irregularities at Arecibo *Geophys. Res. Lett.*
25 3067
Pradipta R, Labno A, Lee M C, Burke W J, Sulzer M P, Cohen J A, Burton L M, Kuo S P and Rokusek D L 2007 Electron precipitation from the inner radiation belt above
Arecibo *Geophys. Res. Lett.* **34** L08101
Pradipta R *et al* 2008 Space plasma disturbances caused by launched whistler waves *Phys. Scr.* **T132** 014031
Reinisch B 2009 private communication
Starks M J and Lee M C 2000 Matched filtering for the measurement of conjugately ducted VLF transmission *Radio Sci.* **35** 351
Starks M J, Lee M C and Jastrzebski P 2001 Interhemispheric propagation of VLF transmissions in the presence of ionospheric HF heating *J. Geophys. Res.* **106** 5579

Appendix D.

Solar Powered Microwave Transmission for Communications and Remote Sensing

By L.N. Whitehurst[1], M.C. Lee[1,2], R. Pradipta[2]

1. Department of Electrical & Computer Engineering, Boston University, Boston, MA 02215, USA
2. Space Propulsion Lab, Massachusetts Institute of Technology (MIT), Cambridge, MA 02139, USA

Abstract

A solar powered microwave transmission system is proposed for remote sensing and communications purposes. We present in this paper (1) a proof of concept to operate solar powered microwave transmission, and (2) investigation of microwave interactions with atmospheric plasmas. In this conceptualized system, a solar thermophotovoltaic system is considered to produce direct current electricity, which is then converted to microwaves in an array. The results from these simulations provide insight on how to produce an economically and environmentally conscience energy source, that can be used for communication and remote sensing applications. However, it is expected that microwaves may interact with ionospheric plasmas, primarily, in the E region to induce large scale fluctuations in plasma density and geomagnetic fields with threshold wave electric field intensities of ~ 1 V/m. After we determine the instability thresholds, we can use them to set up the safe operation range of solar powered microwave transmission.

1. Introduction to Proposed System

The proposed system, illustrated in Figure 1, consists of the sun as the input to a solar thermophotovoltaic system which produces dc current. The dc current passes through a power electronic device that powers a microwave antenna array. The solar thermophotovoltaic system (STPV system) consists of a Fresnel lens, an intermediate structure made up of an emitter and a filter, and photovoltaic cells. A solar thermophotovoltaic system was chosen because it has been theoretically proven to be more efficient than conventional systems, which do not include an intermediate structure [Andreev et al., 2007]. The output current is calculated, and the power transmitted from the system is estimated in order to use the system under safe conditions for not perturbing Earth's environment.

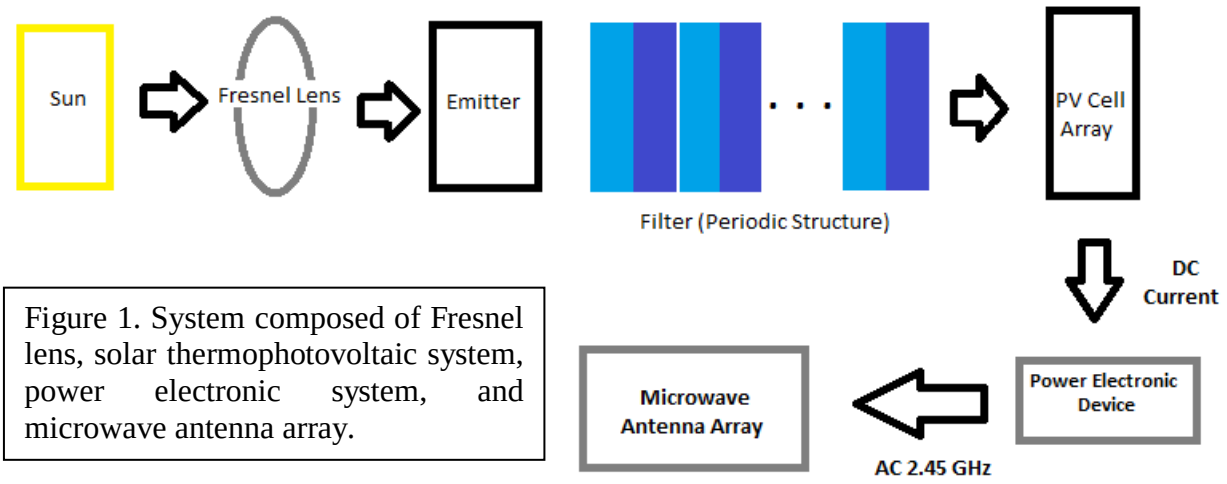

Figure 1. System composed of Fresnel lens, solar thermophotovoltaic system, power electronic system, and microwave antenna array.

The second part of this paper is the analysis of microwave interactions with atmospheric plasmas. It is expected that microwaves may interact with ionospheric plasmas, especially in the E region, to induce large-scale fluctuations in plasma density and geomagnetic fields. This expectation arises from the fact that microwaves can impose two kinds of nonlinear forces on ionospheric plasmas, i.e., radiation pressure force, and thermal pressure force. These two nonlinear forces additively produce a quasi-DC apparent electric field (E_{app}), acting on electrons, to induce plasma density irregularities/fluctuations (δn), according to electric Gauss' law. Consequently, the apparent electric field (E_{app}) together with the background

Earth's magnetic field (B_o) cause the so-called E_{app} x B_o electron drifts, and subsequently yield the geomagnetic field fluctuations (δB_o), according to Ampere's law. The simultaneous generation of δn and δB_o is associated with a large-scale plasma instability driven by thermal pressure force. The calculations of the intensity and impact of these instabilities is necessary to operate the proposed system under conditions safe to the environment.

The overall system was inspired by the solar powered satellite (SPS) project, which has been researched for over forty years [see, e.g., National Space Society website, 2011]. In the SPS project, solar energy is harvested by a solar array in orbit around the earth, and then the collected power is transmitted to the surface of the earth through microwave transmission for conversion into electricity. However, the proposed system in this paper is a different idea. We propose to build the system on the surface of the earth, rather than in space, for remote sensing and communications purposes. The second part of this paper is also imperative because interactions between microwaves and the atmosphere need to be evaluated for environmental impacts. It is important that the proposed system does not cause detrimental ecological effects, such as causing geomagnetic field fluctuations, which birds and some insects rely on for daily life.

First describe in this paper is the properties behind a solar thermophotovoltaic system, which will then lead into the description of the preliminary calculations carried out for first part of the paper. After a full system description, theory on microwave interactions with atmospheric plasmas is presented**.** This includes analysis of geomagnetic field fluctuations and plasma density irregularities caused by the injected microwave radiation. Thus, the presentation of this paper is organized as follows. The proof of concept for the proposed solar powered system together with the numerical method is described in Section 2. Subsequently given in Section 3 is the preliminary system analysis based on selected STPV design parameters. Evaluations of microwave interactions with atmospheric plasmas are discussed in Section 4. Finally given in Section 5 are the summary, conclusions, and discussion on future work.

2. Proof of Concept for Solar Powered System

The proposed solar thermophotovoltaic system is described below to explain why we use this system rather than the conventional one, which does not have an intermediate structure between the sun and the solar cell. Then, the mathematical approach used for finding system properties is presented.

2.1 Solar Thermophotovoltaic Systems

The solar thermophotovoltaic system consists of a Fresnel lens, a thermally heated emitter, a selective filter, and photovoltaic cells (see the block diagram given in Figure 1). The Fresnel lens is used to allow a high concentration of solar radiation to hit the emitter of the system, and allow the emitter to reach the desired temperature range [Andreev et al., 2007]. The emitter is chosen so that it absorbs solar energy with high efficiency, and it has a selective emission spectrum. Therefore, the high temperature emitter will emit radiation within a known range of wavelengths. The emitted photons then pass through a filter that will further reflect radiation back to the emitter to be reabsorbed. The filter's transmissivity will allow radiation within a narrow wavelength range, corresponding to the band gap wavelength in the photovoltaic cells, to pass through and reach the solar cells. The reflected radiation off the filter is

reabsorbed by the intermediate structure. This allows the emitter to stay within a specific temperature range, and it also recycles the radiation whose energy would have been lost.

The intermediate structure in this system is used to increase the efficiency of solar energy conversion. Without it, photons with energy below the band gap of the PV cells, corresponding to light with wavelengths above the band gap wavelength, do not contribute to current, and all of their energy is lost. On the other hand, photons with energy much higher than the band gap of the PV cells do contribute to current, but all the energy that surpasses the band-gap is lost to heat. Therefore, a properly designed intermediate structure may improve the efficiency of the system if it only permits photons within a specific energy range, corresponding to a specific wavelength range, to reach the solar cell. The intermediate structure should absorb radiation, suppress sub-band gap radiation, and restrict the bandwidth of emission above the band gap. The incorporation of the intermediate structure to perform these tasks can greatly improve the efficiency of the system, because reflection off the top of a PV cell, and losses due to photons with not enough energy or too much energy accounts to almost 70% of solar energy losses [El-Sharkawi, 2009].

2.2 Transfer Matrix Method

The transfer matrix of a system relates the input electromagnetic field to the output electromagnetic field passing through a material of known optical properties. First, consider a transverse, electromagnetic field at normal incidence to a system consisting of one material:

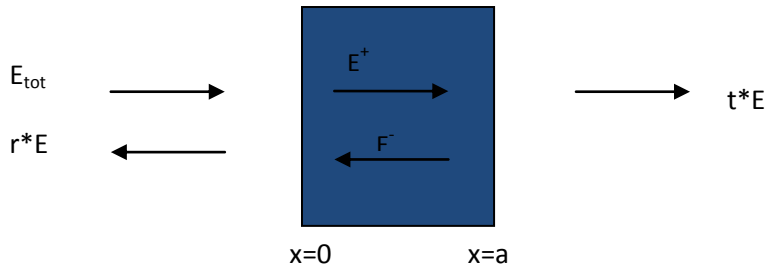

Figure 2. Illustration of input and output electromagnetic fields passing through a material.

The total electromagnetic field $E_z(x)$ within the material is made up of the wave moving in the positive x-direction (E^+), and the reflected wave moving in the negative x-direction (E^-). These together represent the total wave traveling in the x-direction; Faraday's Law relates this electric field to the corresponding magnetic field (B):

$$\nabla x\vec{E} = -j\omega\vec{B}$$

We have two expressions, one for the electric field and the other for the magnetic field,

$$E_Z(x) = E_1^+ e^{+jkx} + E_1^- e^{-jkx}$$

$$Z_0 H_y(x) = -\frac{ck}{\omega} E_1^+ e^{+jkx} + \frac{ck}{\omega} E_1^- e^{-jkx}$$

Then, at the initial position (x=0), the boundary condition requires:

$$E_Z(x=0) = E_1^+ + E_1^-$$

$$Z_0 H_y(x=0) = -\frac{ck}{\omega} E_1^+ + \frac{ck}{\omega} E_1^-$$

$$.Z_o = \sqrt{\frac{\mu_o}{\varepsilon_o}}$$

They can be written in the matrix form:

$$\begin{bmatrix} E_z(x=0) \\ Z_0 H_y(x=0) \end{bmatrix} = \begin{bmatrix} 1 & 1 \\ -\frac{ck}{\omega} & \frac{ck}{\omega} \end{bmatrix} \begin{bmatrix} E_1^+ \\ E_1^- \end{bmatrix}$$

$B = \mu_o H$, and Z_0 is the intrinsic impedance in free space. Next, we find the corresponding equations for the wave as it reaches the edge of the material (x=a). Here, the two equations for the electric and magnetic field result in:

$$E_Z(x=a) = E_1^+ e^{+jka} + E_1^- e^{-jka}$$

$$Z_0 H_y(x=a) = -\frac{ck}{\omega} E_1^+ e^{+jka} + \frac{ck}{\omega} E_1^- e^{-jka}$$

The corresponding matrix form is:

$$\begin{bmatrix} E_z(x=a) \\ Z_0 H_y(x=a) \end{bmatrix} = \begin{bmatrix} 1 & 1 \\ -\frac{ck}{\omega} & \frac{ck}{\omega} \end{bmatrix} \begin{bmatrix} e^{+jka} & 0 \\ 0 & e^{-jka} \end{bmatrix} \begin{bmatrix} E_1^+ \\ E_1^- \end{bmatrix}$$

Therefore, to find the matrix representing the incident wave at x=0 related to the output wave at x=a, we combine these two matrix equations and get the following, overall system matrix equation:

$$\begin{bmatrix} E_z(x=a) \\ Z_0 H_y(x=a) \end{bmatrix} = \begin{bmatrix} 1 & 1 \\ -\frac{ck}{\omega} & \frac{ck}{\omega} \end{bmatrix} \begin{bmatrix} e^{+jka} & 0 \\ 0 & e^{-jka} \end{bmatrix} \begin{bmatrix} 1 & 1 \\ -\frac{ck}{\omega} & \frac{ck}{\omega} \end{bmatrix}^{-1} \begin{bmatrix} E_z(x=0) \\ Z_0 H_y(x=0) \end{bmatrix}$$

or

$$\begin{bmatrix} E_z(x=a) \\ Z_0 H_y(x=a) \end{bmatrix} = \begin{bmatrix} cos(ka) & -jsin(ka)\frac{\omega}{ck} \\ -jsin(ka)\frac{ck}{\omega} & cos(ka) \end{bmatrix} \begin{bmatrix} E_z(x=0) \\ Z_0 H_y(x=0) \end{bmatrix}$$

In the presence of a second material, it can be shown through the same method that the overall matrix representation for the electromagnetic wave to propagate in two media is:

$$\begin{bmatrix} E_z(x=b) \\ Z_0 H_y(x=b) \end{bmatrix} = \\ \begin{bmatrix} cos(kb) & -jsin(kb)\frac{\omega}{ck} \\ -jsin(kb)\frac{ck}{\omega} & cos(kb) \end{bmatrix} \begin{bmatrix} cos(ka) & -jsin(ka)\frac{\omega}{ck} \\ -jsin(ka)\frac{ck}{\omega} & cos(ka) \end{bmatrix} \begin{bmatrix} E_z(x=0) \\ Z_0 H_y(x=0) \end{bmatrix}$$

The "Transfer-Matrix" is the matrix that relates the input signal to the output signal of the system, and it is represented by:

$$M = \\ \begin{bmatrix} cos(kb) & -jsin(kb)\frac{\omega}{ck} \\ -jsin(kb)\frac{ck}{\omega} & cos(kb) \end{bmatrix} \begin{bmatrix} cos(ka) & -jsin(ka)\frac{\omega}{ck} \\ -jsin(ka)\frac{ck}{\omega} & cos(ka) \end{bmatrix}$$

In order to find the relationship between the transfer matrix and the reflection and transmission coefficients, we consider the following normalized equations to relate the electric fields with reflection and transmission coefficients for the system:

$$E_z(x=0) = 1 + r$$

$$E_z(x=a) = t$$

$$Z_0 H_y(x=0) = -\frac{ck_i}{\omega} + r\frac{ck_i}{\omega}$$

$$Z_0 H_y(x=a) = t\frac{ck_0}{\omega}$$

It can be shown with these reflection and transmission equations, along with the matrix equation relating the incident and transmitted electromagnetic waves, yields the following matrix equation:

$$\begin{bmatrix} 1 \\ r \end{bmatrix} = \begin{bmatrix} 1 & 1 \\ -\frac{ck_i}{\omega} & \frac{ck_i}{\omega} \end{bmatrix}^{-1} M^{-1} \begin{bmatrix} 1 & 1 \\ -\frac{ck_0}{\omega} & \frac{ck_0}{\omega} \end{bmatrix} \begin{bmatrix} t \\ 0 \end{bmatrix}$$

This method can be used to study the optical properties of photonic crystals. With these matrices, we have the tools to calculate the absorption, and therefore emission of materials. It is also possible to find the

transmission and reflection of a multiple layer stack of materials by computing the overall transfer matrix for the system and solving the above matrix equation for the transmission and reflection coefficients. Although all angles of incidence should be considered, we only consider normal incidence, because it is a good approximation for a wide range of incident angles for our system [Bermel, 2010].

3. System Analyses and Results

In order to analyze the overall system, each component was chosen from previously proposed designs. For the solar thermophotovoltaic system, we chose the system proposed by Celanovic et al. [2004] in "1D and 2D Photonic Crystals for Thermophotovoltaic Applications."

3.1 STPV Design Parameters and Results

The system described by Celanovic et al. consists of a selective emitter and multiple layer photonic crystal. These are placed between the Fresnel lens and photovoltaic cells in our proposed system. The photovoltaic cells are made up of GaSb devices. GaSb devices are low-bandgap semiconductor materials, their electronic bandgap is $E_g = 0.7$ eV. This bandgap corresponds to the wavelength $\lambda_g = 1.78$ µm. The refractive index of GaSb is n = 3.9.

The photonic crystal is a periodic structure consisting of SiO_2 and Si, with refractive indices $n_1 = 1.5$ and $n_2 = 3.4$, respectively. The photonic crystal's central wavelength is designed around the bandgap wavelength of the GaSb cells. The optimal system designed around this central wavelength was determined to be composed of five periods of SiO_2/Si materials placed in front of the PV cell. The thickness for each layer is $d_1 = 0.39$ µm and $d_2 = 0.17$ µm, as depicted in Figure 3. Using the matrix transfer method for determining the reflectance of this system produces the results in Figure 4.

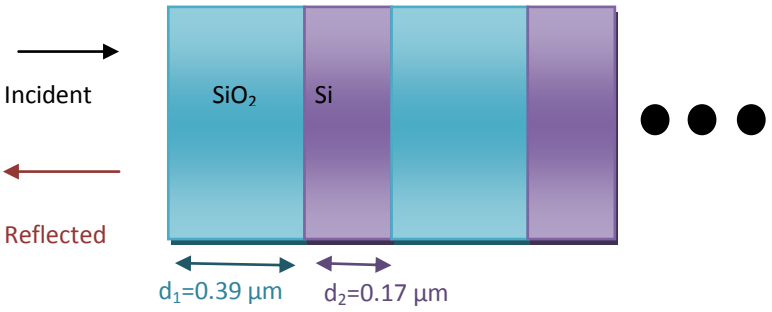

Figure 3. Periodic filter made up of SiO_2 and Si consisting of five periods. It is placed in front of the photovoltaic cells.

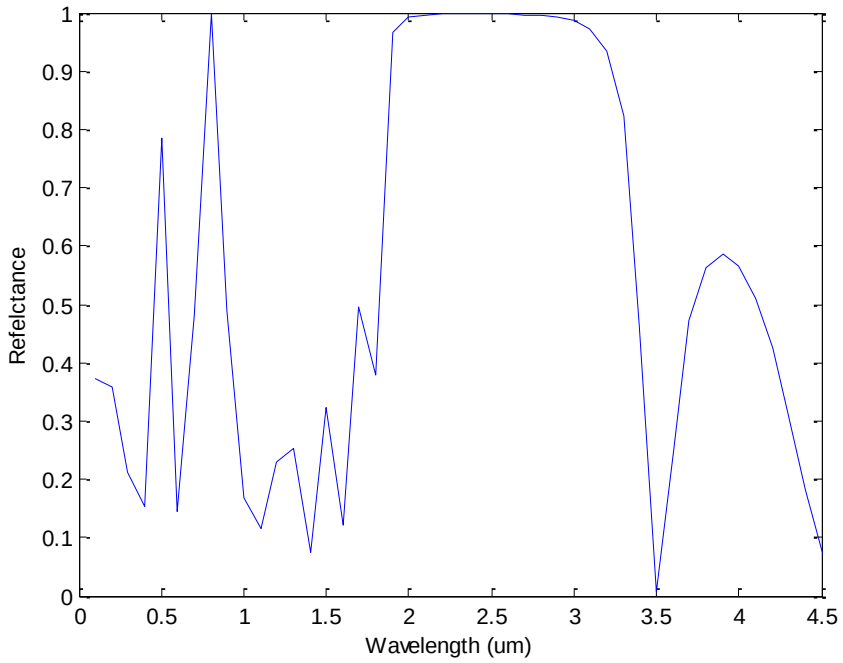

Figure 4. Reflectance of periodic photonic crystal made of SiO_2 and Si. It is composed of five periods.

These results are a reproduction of the original publication findings for the filter reflectance characteristics. As one can see, the filter allows radiation with wavelengths around the bandgap of the GaSb cells (1.78 μm) to pass through, and highly reflects the radiation above and below the bandgap wavelength. This will allow the emitter to reabsorb the radiation that would not have been useful in producing current in the GaSb cells.

The selective emitter for this system is made of tungsten substrate because it exhibits high emittance at low wavelengths, up to 1.8 μm, and high reflectance at longer wavelengths. Using this tungsten emitter and the periodic photonic crystal structure, the radiation reaching the GaSb cells will be in the range so that it produces current at a high efficiency. Figure 5 shows the output power density as a function of emitter temperature.

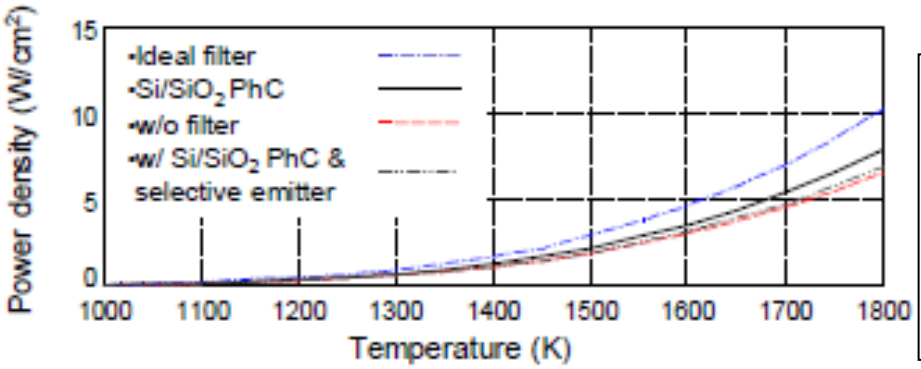

Figure 5. Output power density produced by GaSb cells with a tungsten selective emitter together with the periodic structure [Celanovic et al., 2004].

For a tungsten emitter at 1400K, the output power density of the system will be approximately 1.5 W/cm^2. According to the current-voltage characteristics for GaSb cells (Figure 6), this corresponds to an output current of 5 A at a voltage around 0.3 V per square centimeter of GaSb cells.

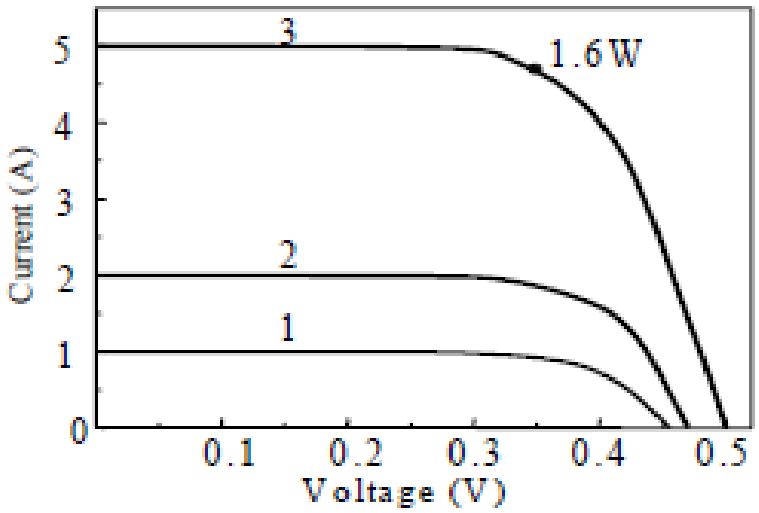

Figure 6. V-I characteristics for 1 cm^2 area of GaSb cells [Rumyantsev et al., 2004].

3.2 Powering Microwave Antenna Array

This solar thermophotovoltaic system will produce dc current. This current will then pass through integrated electronic circuits to power a microwave antenna array. Currently, microwave transmitting systems can be powered using magnetron at 2.45 GHz, e.g., in VTF laboratory experiments [Lee et al., 1998a] and klystron for radars (e.g., 2.38 GHz dish at Arecibo, Puerto Rico). However, klystron transmitters require high voltages to operate, which make them not desirable for use in our proposed solar powered system. While the klystron radar systems are powered by high voltages, the GaSb cells operate at low voltages. Therefore, our system should utilize a power electronic device for low-voltage applications. The future work will consider the development of this part of overall system. It is mandatory to develop integrated electronic circuits for transmission of microwave radiations for low-voltage applications.

4. Microwave Interactions with Ionospheric Plasmas

Based on the proposed solar powered microwave transmission system, we hypothesize the following scenario. A microwave beam is transmitted from the antenna array on the ground, as depicted in Figure 7, propagating from the neutral atmosphere into the ionosphere. We ignore any microwave interactions with the neutral atmosphere due to background density inhomogeneity and temperature gradients. Furthermore, any birefringent effects imposed by the Earth's magnetic field can be also neglected, because ionospheric plasma density is dilute enough for one to consider that the ionosphere is transparent to the microwave. In other words, one can reasonably assume that there is no significant reflection of transmitted microwave from the neural atmosphere and the ionosphere.

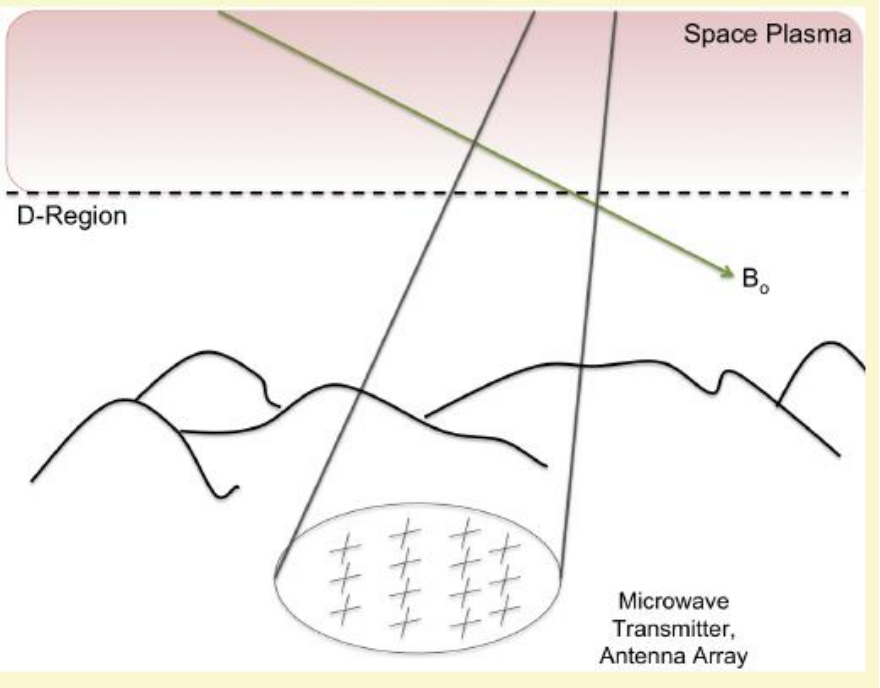

Figure7. A microwave beam is transmitted from the antenna array on the ground, propagating from the neutral atmosphere into the ionosphere.

4.1 Radio Wave-induced Ionospheric Plasma Structures

However, microwave can interact with the ionosphere via electron collisions (ν_e), which includes two parts, i.e., $\nu_e = \nu_{en} + \nu_{ei}$ where ν_{en}, is electron-neutral collision frequency and ν_{ei} the electron-ion collision frequency. In the ionospheric E region, $\nu_{en} \approx 1$ MHz, $\nu_{ei} \approx$ a few tens of Hz (i.e., $\nu_e \approx \nu_{en}$), while in the ionospheric F region, $\nu_{en} \approx$ a few Hz, $\nu_{ei} \approx 1$ kHz (i.e., $\nu_e \approx \nu_{ei}$). Electron collisions can create thermal pressure force as the main driving force, to excite the so-called thermal filamentation instability, yielding large-scale ionospheric density irregularities and geomagnetic field fluctuations [Lee et al., 1998b; Cohen et al., 2010]. In the
HF heating of the ionosphere, large plasma sheets (ionospheric ducts) in the form of parallel-plate waveguides was generated in our Arecibo experiments [Lee et al., 1998b; Pradipta et al., 2008] and Gakona experiments [Cohen et al., 2010], shown in Figures 8(a) and 8(b), respectively. As these large plasma sheets experienced ExB drifts, they were detected by radar beams to produce slanted stripes in the RTI (range-time-intensity) plots. By contrast, we expect that microwave-produced ionospheric ducts will have filament-type of structures as shown in Figure 9.

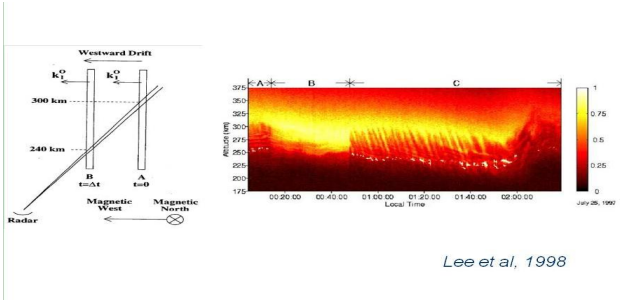

Figure 8(a). Arecibo radar-detection of parallel-plate waveguides generated by HF heater waves [Lee et al. 1998b].

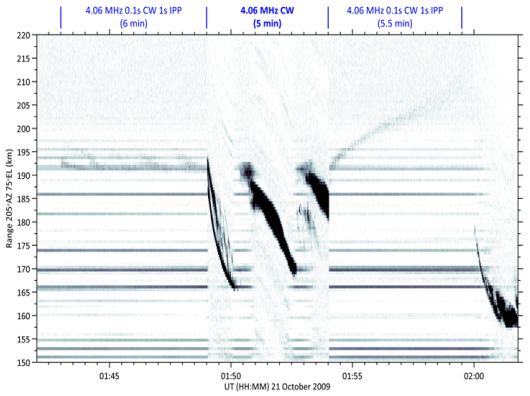

Figure 8(b). HAARP MUIR radar detect of O-mode HF heater wave-created large plasma sheets [Cohen et al., 2012].

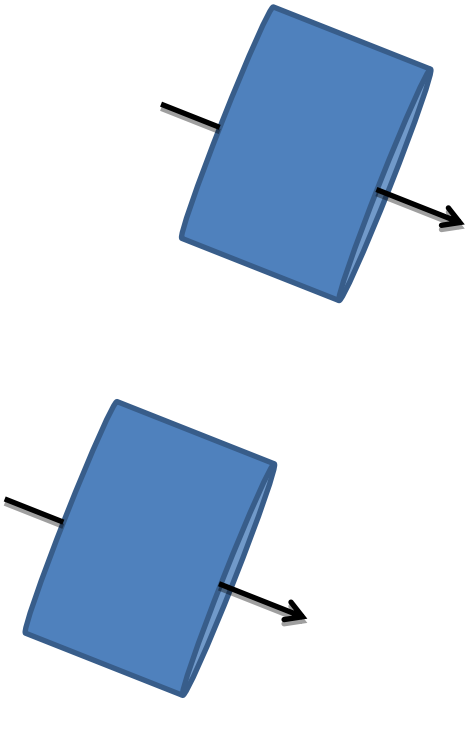

Figure 9. Predicted filament-type of microwave-induced ionospheric ducts/waveguides. The arrowed straight lines represent the Earth's magnetic field ($\mathbf{B_0}$). The size of the filaments along $\mathbf{B_0}$ is determined by the microwave beamwidth.

The basis for this prediction is the following. For HF heater waves transmitted vertically in the experiments, the two component waves known as O- and X-modes propagate across and along the Earth's magnetic field (**B**) near their reflection heights, as delineated in Figure 10. The magnetic field and the horizontal direction can be used to determine the meridional plane. For vertically transmitted O- or X-mode HF wave, it is reasonable to expect that they propagate within the meridional plane. The thermal filamentation instability involves a three wave interaction process wherein the heater wave (with a wave vector of either $\mathbf{k_o}$ or $\mathbf{k_x}$) parametrically excites a high-frequency electromagnetic wave and a low-

frequency (nearly zero-frequency) electrostatic wave (denoted corresponding by $\mathbf{k}^{o}_{I}$ or $\mathbf{k}^{x}_{I}$). Note that $\mathbf{k}^{o}_{I}$ or $\mathbf{k}^{x}_{I}$, in general, has a rather small component along the Earth's magnetic field, compared to its perpendicular component. In other words, they are highly field-aligned to reduce parallel diffusion loss as elaborated later.

As depicted in Figure 10, this electrostatic mode is associated with ionospheric plasma density fluctuations with wave vector $\mathbf{k}^{o}_{I}$ ($\mathbf{k}^{x}_{I}$) nearly orthogonal (parallel) to the meridional plane. It indicates that plasma sheets/parallel-plate waveguides can be generated by O-mode (X-mode) HF heater wave parallel (orthogonal) to the meridional plane. These parallel-plate waveguides have been detected by Arecibo radar and HAARP MUIR radar in RTI plots shown in Figures 8(a) and 8(b). Contrastingly, in the case of microwave interactions with ionospheric plasmas, there is no significant difference between the two component waves (O- and X-modes) in generating large-scale field-aligned plasma modes. The reason is that microwave frequency is greater than electron plasma frequency and electron gyro-frequency by nearly three orders of magnitude. Consequently, $\mathbf{k}_{I}$ (either $\mathbf{k}^{o}_{I}$ or $\mathbf{k}^{x}_{I}$) is orthogonal to the Earth's magnetic field in any direction to form filament type of density irregularities, as illustrated in Figure 9.

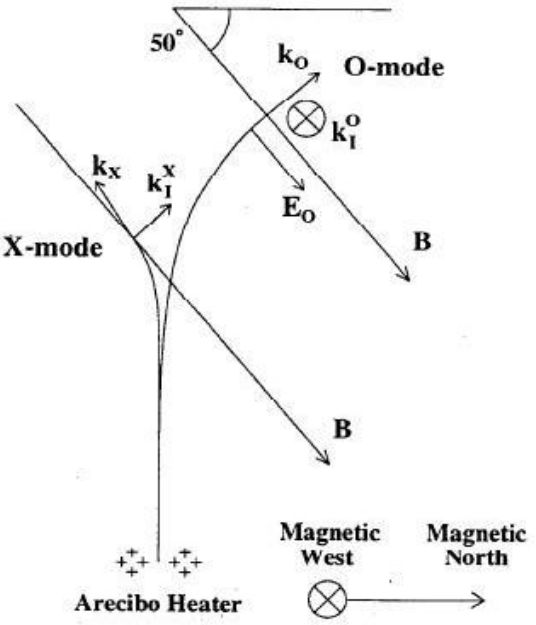

Figure 10. Trajectories of O- and X-mode propagation in the ionosphere [Lee et al., 1998b]. $\mathbf{k}_{o}$ and $\mathbf{k}_{x}$ denote the wave vectors of O- and X-modes, respectively. $\mathbf{k}^{o}_{I}$ and $\mathbf{k}^{x}_{I}$ stand for the wave vectors of O- and X-mode induced plasma sheets/parallel-plate waveguides.

The plasma process responsible for the generation of large plasma sheets or plasma filaments and magnetic field fluctuations during ionospheric RF heating is briefly explained below [Whitehurst and Lee, 2012]. Both radiation pressure force (and known as ponderomotive force) and thermal pressure force work additively to provide the nonlinear effects in exciting the filamentation instability. But, the thermal pressure force plays a dominant role in the excitation of large-scale field-aligned ionospheric plasma modes. Here, the term "large-scale field-aligned" refers to those electrostatic plasma modes with scale lengths ranging from hundreds meters to a few kilometers. Their scale lengths are greater than electron mean free paths; therefore, collisional heating can favorably occur to build a heat source along the Earth's magnetic field. Under the action of HF waves or microwaves, only electrons but not ions (e.g., atomic oxygen ions concerned in ionospheric E and F regions) can respond to these high-frequency wave fields. Hence, electron density fluctuations result according to Electric Gauss law. An apparent electric field

($\mathbf{E_{app}}$) can be defined from the thermal pressure force ($\mathbf{F_{th}}$) as ($\mathbf{E_{app}}$) = $\mathbf{F_{th}}$/(- en_o) where e and n_o are electric charge and the background electron density, respectively. This apparent electric field together with Earth's magnetic field ($\mathbf{B_o}$) gives rise to an $\mathbf{E_{app}}$ x$\mathbf{B_o}$ drift of electrons, producing an electric current following Ampere's law.

4.2 Roles of Electron Collisions in Micriowave-ionospheric Interactions

We now examine the key roles of electron collisions in leading to thresholds for the thermal filamentation instability during microwave-ionospheric interactions. One hand electron collisions produces a heat source, as the source of free energy, to drive the instability. On the other hand they impose a damping process in colliding with neutral and charged particles. Electrons can move freely along but not across the magnetic field. Thus, heat conduction loss of electrons occurs mainly along the geomagnetic field. It reduces the effect of the thermal pressure force, and thus, is a factor to impose the instability threshold. However, electron collisions can reduce the heat conduction loss along the magnetic field. This aspect can be understood as follows. In the microwave-illuminated ionospheric region the motion of heated electrons are restricted by many surrounding neutral particles, especially, in the ionospheric E region. Heated electrons moving to escape the area can be bounced back by neutrals. Heat conduction loss can, thus, be reduced by electron collisions.

Following above discussions we can subsequently estimate the three key damping mechanisms. They are (1) collisional damping , (2) cross-field diffusion, and (3) parallel thermal diffusion loss, described respectively by the expressions of (1) $m_e/M_i(M_n)$, (2) $k_\perp^2 v_{te}^2/\omega_{ce}^2$ [= $(2\pi)^2(r_{ce}/\lambda_\perp)^2$] and (3) $k_{||}^2 v_{te}^2/\nu_e^2$ [= $(2\pi)^2(\lambda_{mfp})/\lambda_{||})^2$] where $m_e/M_i(M_n)$, $k_\perp$ (=$2\pi/\lambda_\perp$), $k_{||}$ (=$2\pi/\lambda_{||}$), $\lambda_\perp$, $\lambda_{||}$, v_{te}, ω_{ce}, r_{ce}, ν_e, and λ_{mfp} are electron to ion (neutral particle) mass ratio, irregularity perpendicular wave number, irregularity parallel wave number, perpendicular scale length, parallel scale length, electron thermal velocity, electron cyclotron frequency, electron gyro-radius, electron collision frequency, and electron mean free path, respectively. Note that m_e/M_i is basically equal to m_e/M_n, and $\lambda_\perp << \lambda_{||}$ (i.e., $k_\perp >> k_{||}$). Here, $\lambda_\perp$ and $\lambda_{||}$ represent, respectively, the radius and the length of the plasma density filaments created by microwaves and delineated in Figure 9. In the transmission of microwaves for communications and remote sensing applications, the beamwidth determines the maximum length of $\lambda_{||}$. It is reasonable to assume that the dimension of the microwave heated ionospheric region is about a few kilometers (say, 5 km). Then, filaments of large ionospheric ducts with scale lengths from hundreds meters to a few kilometers can be generated within the microwave heated plasma region, as depicted in Figure 9.

While the thermal filamentation instability can be excited in both E- and F-regions during ionospheric HF heating experiments, we will show that only E-region can be perturbed by hypothesize microwave beams. Simply speaking, the parallel diffusion loss ($k_{||}^2 v_{te}^2/\nu_e^2$) is much greater in microwave beam case than in typical HF heating experiments. This difference stems from the fact that HF wave heated region has a linear dimension of several tens of kilometers (say, $\lambda_{||} \approx 50$ km) versus a few kilometers (say, $\lambda_{||} \approx 5$ km) in microwave illuminated region. We adopt the following E-region and F-region parameters to evaluate the relevant importance of these damping mechanisms in the excitation of 500 meter-scale ducts (i.e., $\lambda_\perp = 5$ km, $\lambda_{||} = \sim 14$ km).

(In E region): m_e/M_i (NO^+) = 1/(30 x 1840), v_{te} = 1.3 x 10^5 m/s (for T_e = 1000^o k), $\omega_{ce}/2\pi$ = 1.3 MHz, and ν_e = 1.0 MHz. Then, we get (1) m_e/M_i = 2.0 x 10^{-5}, (2) $k_\perp^2 v_{te}^2/\omega_{ce}^2$ = 7.0 x 10^{-9}, and (3) $k_{||}^2 v_{te}^2/\nu_e^2$ = 1.0 x 10^{-10}. It is seen that collisional damping is the dominant damping mechanism among those three.

(In F region): m_e/M_i (O^+) = 1/(16 x 1840), v_{te} = 1.3 x 10^5 m/s (for T_e = 1000^o k), $\omega_{ce}/2\pi$ = 1.3 MHz, and ν_e = 1.0 kHz. Then, we have (1) m_e/M_i = 3.3 x 10^{-5} (slightly greater than that in E region), (2) $k_\perp^2 v_{te}^2/\omega_{ce}^2$ = 7.0 x 10^{-9} (same as that in E region) and (3) $k_\parallel^2 v_{te}^2/\nu_e^2$ = 1.0 x 10^{-4} (much greater than that in E region). It is found that the parallel diffusion loss even exceeds the collisional damping for the excitation of kilometer-scale modes. These results indicate that the thermal filamentation instability of microwaves cannot occur in the ionospheric F region primarily because of the larger parallel diffusion loss, as mentioned before.

It is interesting to notice that when the thermal filamentation instability is excited in ionospheric plasmas, electron collisions create the heat source and, meanwhile, impose the collisional damping. We can expect that the threshold field intensity for the instability excitation is independent of electron collision frequency. In fact, this is indeed what we find in our instability analyses for HF ionospheric heating experiments as well as for the hypothesized microwave-ionosphere interactions processes. The required threshold microwave fields in the E region are estimated to be a fraction of 1.0 V/m, which are higher than those for HF wave fields by two orders of magnitude. This is expected from the fact that microwave frequency is higher than that of ionospheric plasma frequency by nearly three orders of magnitude, while HF heater wave frequency is comparable but, slightly less than the FoF2 (i.e., the maximum ionospheric plasma frequency).

5. Summary and Conclusions

We have used transfer matrix method as a different approach to analyze the proposed solar thermophotovoltaic system, along with calculations for the output current required for the microwave transmission through an antenna array. The theoretical study carried out for microwave interactions with space plasmas shows that on one hand electron collisions create the thermal source to excite the thermal filamentation instability, but, on the other hand, they cause collisional damping as a mechanism to impose instability thresholds. If electron collisions are the dominant damping mechanism, then, the threshold wave field intensities are mainly determined by the balance between the heat source and collisional damping. Then, it is understandable that the expressions for the threshold condition do not depend on electron collision frequency. This is the common situation in HF wave heating experiments, which involve a large illuminated area (e.g., 50 km by 50 km). However, in our hypothesized microwave interactions with the ionosphere, a narrow wave beam is considered for remote sensing and communications applications. It is found that significant microwave interactions can occur in the ionospheric E region, but not in the F region primarily due to different parallel diffusion loss.

The prominent role of parallel diffusion process in preventing the instability from occurrence can be seen in the following calculations. The parallel diffusion process can be represented by $k_\parallel^2 v_{te}^2/\nu_e^2$ [= $(2\pi)^2(\lambda_{mfp}/\lambda_\parallel)^2$] where λ_{mfp} is mean free path and $\lambda_\parallel$ = 5 km imposed by the microwave beamwidth. In the F region, $\nu_e \approx \nu_{ei}$ (electron-ion collision frequency) ~ e.g., 1 kHz, and λ_{mfp} ~ 130 m for v_{te} ~ 1.3 x 10^5 m/sec, leading to $k_\parallel^2 v_{te}^2/\nu_e^2$ ~ 1.0 x 10^{-4}. It is larger than the collisional damping ~ 3.3 x 10^{-5}. By contrast, $\nu_e \approx \nu_{ei}$ (electron-neutral collision frequency) ~ e.g., 1 MHz in the E region, thus, λ_{mfp} ~ 0.13 m, yielding $k_\parallel^2 v_{te}^2/\nu_e^2$ ~ 1.0 x 10^{-10}, which is six orders of magnitude less than the parallel diffusion loss in the F region. One can see that large electron collision frequency can effectively reduce the parallel diffusion loss. For complete comparison, we also examine the cross-field diffusion given by $k_\perp^2 v_{te}^2/\omega_{ce}^2$ [= $(2\pi)^2(r_{ce}/\lambda_\perp)^2$] where r_{ce} is the electron gyro-radius and $\lambda_\perp$ the scale length. For large-scale modes (e.g., $\lambda_\perp$ = 500 m) the ratio $r_{ce}/\lambda_\perp$ is rather small, leading to a negligible cross-field diffusion loss ~ 7.0 x 10^{-9} (approximately the same in both E- and F-regions) in comparison to the collisional damping (~ 3.3 x 10^{-5}).

We plan to conduct experiments to test the predicted microwave wave-ionospheric E region interactions at the Arecibo Observatory. Arecibo radar at 2.38 GHz can be used as the microwave source, and Arecibo 430 MHz incoherent scatter radar (ISR) for diagnosis, aided by our own and Arecibo optical instruments. Under the ExB drifts the microwave-induced ionospheric ducts in the form of filaments are expected to produce dashed lines in the RTI plots [see Figure 11], contrasting the slanted stripes corresponding to HF wave-excited parallel-plate waveguides [see Figures 8(a) and 8(b)]. In conclusion, the use of the proposed environmentally friendly system consists not only of exploring a renewable resource to power the transmission of signals, but also of preventing any significant perturbations to the environment from injected wave interactions.

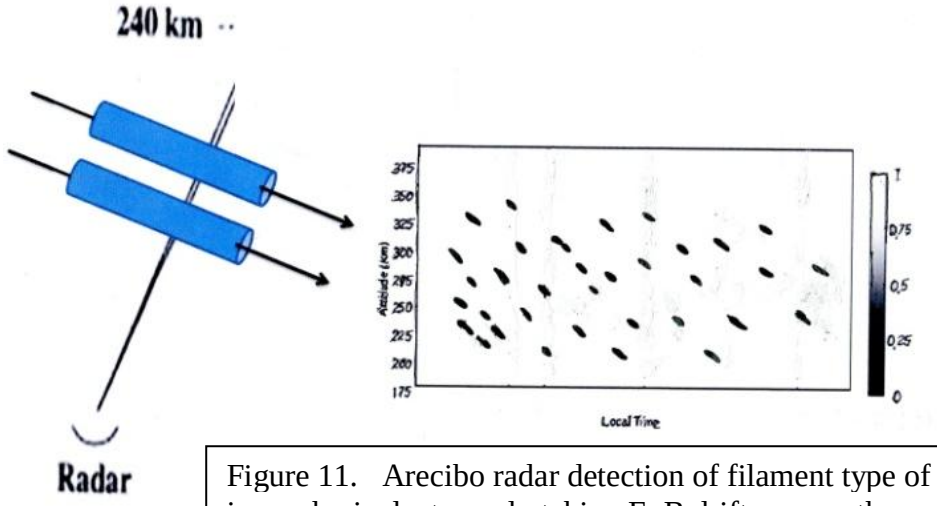

Figure 11. Arecibo radar detection of filament type of ionospheric ducts, undertaking ExB drifts across the radar beam, seen as dashed lines in RTI (range time intensity) plots.

Acknowledgments. This work was supported by AFOSR grant FA9550-09-1-0391. This paper was presented by the first author L.N. Whitehurst as a poster paper for student paper contest as well an oral paper per a session organizer's invitation at the 39th IEEE International Conference on Plasma Science, Edinburgh, Scotland, 9 - 12 July 2012.

References

Andreev, V., V. Khvostikov, and A. Vlasov. "Solar Thermophotovoltaics", *Springer Series in Optical Sciences*. 130. (2007): 175-197.

Bermel, P. et al. "Design and global optimization of high-efficiency thermophotovoltaic Systems", *Optics Expres,*. 18.103 (2010): A314-34.

Celanovic, F. et al. "1D and 2D Photonic Crystals for Thermophotovoltaic Applications", *SPIE*. 5450.1 (2004): 416-22.

Cohen, J. A., R. Pradipta, L. M. Burton, A. Labno, M. C. Lee, B. J. Watkins, C. Fallen, S. P. Kuo, W J Burke, D Mabius, and B Z See, "Generation of ionospheric ducts by the HAARP HF heater", Phys. Scr. **T142** (2010) 014040 (7pp) doi:10.1088/0031-8949/2010/T142/014040.

El-Sharkawi, Mohamed. *Electric Energy: An Introduction*. 2nd ed., CRC Press, 2009.

Lee, M.C., R.J. Riddolls, and D.T. Moriarty, "Laboratory studies of some ionospheric plasma effects caused by lightning induced whistler waves", J. Atmos. Solar-Terres. Phys., 60, 965, 1998a.

Lee, M.C., R.J. Riddolls, W.J. Burke, M.P. Sulzer, S.P. Kuo, and E.M.C. Klien, "Generation of large sheet-like ionospheric plasma irregularities at Arecibo", Geophys. Res. Lett., 25, 3067, 1998b.

Pradipta, R., J. A. Cohen, M. C. Lee, A. Labno, L. M. Burton, R. J. Riddolls, O. V. Batishchev, A.J. Coster,W.J. Burke, M. J. Starks, M. P. Sulzer and S. P. Kuo, "Space plasma disturbances caused by NAU-launched whistler waves", Phys. Scr. T132 (2008), 014031, doi:10.1088/0031-8949/2008/T132/014031.

Rumyantsev, V.D, et al. "Structural Features of a Solar TPV System", Freiburg: AIP, 79-87, 2004.

Whitehurst, L.N. and M.C. Lee, "Solar Powered Microwave Transmission and Interactions with Atmospheric Plasmas", Student Paper Contest, 39th IEEE International Conference on Plasma Science. Edinburgh, Scotland, UK, 9-12 July, 2012.

Appendix E.

Large plasma filaments and geomagnetic field fluctuations excited concomitantly by solar powered microwave transmissions

L N Whitehurst[1], M C Lee[1,2] and R Pradipta[2]

[1] Department of Electrical and Computer Engineering, Boston University, Boston, MA 02215, USA
[2] Space Propulsion Lab, Massachusetts Institute of Technology (MIT), Cambridge, MA 02139, USA

E-mail: xxx

Received 23 July 2012
Accepted for publication 24 July 2012
Published xxx
Online at stacks.iop.org/PhysScr/T149/000000

Abstract
We investigate large-scale, filament-type of ionospheric plasma turbulence produced by a ground-based solar-powered microwave transmission system. It is shown that microwaves can interact with the ionosphere, primarily, in the E region. Electron collisions play key roles in the generation of large-scale fluctuations in ionospheric plasma density and geomagnetic fields via a thermal filamentation instability. The threshold wave field intensities are found to be of $\sim 1\ \mathrm{V\ m^{-1}}$ for the instability. Possible radar detection of microwave-induced ionospheric plasma effects is discussed and planned for our future Arecibo experiments in Puerto Rico.

PACS number: 52.50.−Sw

(Some figures may appear in colour only in the online journal)

1. Introduction

We propose a solar-powered microwave transmission system for remote sensing and communications purposes (Whitehurst and Lee 2012). This work consists of two parts: (i) proof of concept to operate solar-powered microwave transmissions and (ii) investigation of microwave interactions with atmospheric plasmas. While we will report the concepts and designs of the solar-powered system elsewhere, our research on large-scale ionospheric plasma turbulence caused by injected microwaves will be presented in this paper. The basic mechanism responsible for the concerned microwave–ionospheric interactions is the thermal filamentation instability (Lee *et al* 1998 and references therein). It generates large-scale plasma sheets in the form of parallel-plate waveguides during ionospheric heating by high-frequency (HF) waves at frequencies of a few MHz (Lee *et al* 2012). By contrast, in our current study of microwaves operating at a few GHz to interact with ionospheric plasmas, we expect that filament-type of structured plasma density irregularities will form along the geomagnetic fields. Their radii are estimated to range from hundred meters to a few kilometers.

The concerned microwave–ionospheric interactions involve a plasma instability termed 'thermal filamentation instability', because thermal pressure force is the dominant nonlinear force to drive the instability and cause plasma density irregularities and geomagnetic field fluctuations. We will examine the key role played by electron collision frequency in creating the thermal source as well as its other roles in damping mechanisms to impose thresholds for exciting the instability. This paper is organized as follows. Discussed in section 2 is the mechanism leading to the simultaneous generation of plasma density irregularities and geomagnetic field fluctuations during microwave interactions with the ionosphere. It involves a three-wave interactions process.

Although the birefringent effect is not important in microwave ionospheric propagation, the excited plasma density irregularities associated with nearly zero-frequency modes are highly field-aligned. In section 3 we evaluate the microwave-induced ionospheric plasma effects, and assess damping mechanisms which impose the instability thresholds. The estimates of threshold instabilities will be based on to understand why ionospheric E region rather than F region is primarily affected by the microwave illumination. How to diagnose microwave-created ionospheric plasma effects will be addressed in section 4. A summary and conclusions are finally given in section 5.

1402-4896/00/000000+05$33.00

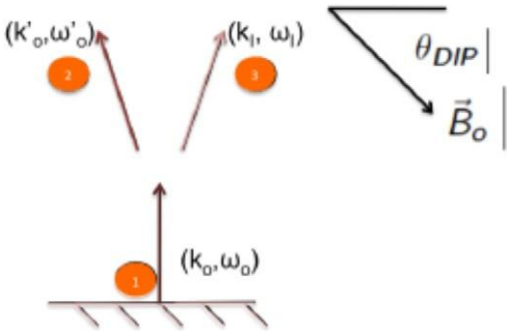

Figure 3. Three-wave interaction involving the incident wave (k_o, ω_o), the daughter HF wave (k^t, ω^t) and the low-frequency electrostatic plasma mode (k_l, ω_l).

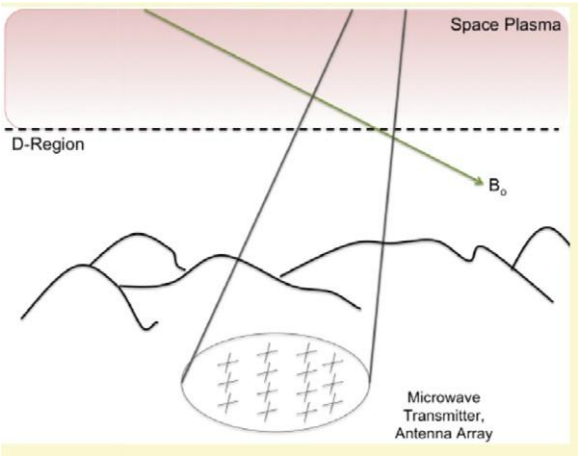

Figure 1. Initial operation of the system. An antenna array transmits microwave radiation.

electric Gauss' Law:

$$\nabla \cdot E_{app} = -\frac{e}{\varepsilon_o}\delta n_e.$$

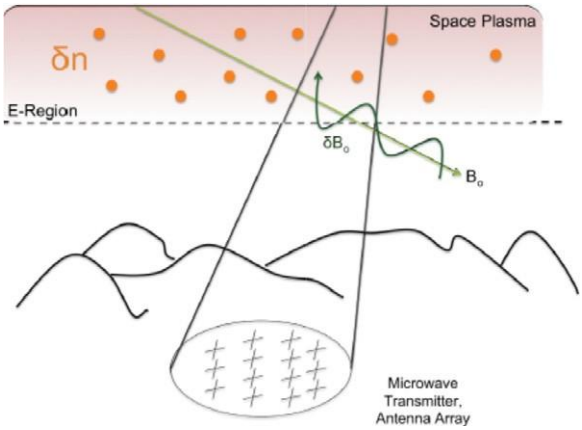

Figure 2. The system can consequently produce fluctuations of δn and δB_o.

2. Microwave interactions with ionospheric plasmas

Illustrated in figure 1 is an antenna array transmitting microwave radiation into the atmosphere. Here, the Earth's magnetic field is represented by $\mathbf{B_o}$ and the lower boundary of the ionospheric D region is by the dashed line. Figure 2 shows a representation of how the atmospheric plasmas can respond to microwave transmissions. We expect with supported theoretical analysis that this transmission can consequently produce plasma density irregularities (δn), represented by the orange dots and geomagnetic field fluctuations (δB_o) represented by the dark green waves along the magnetic field line. These waves, also known as micropulsations, can travel in either direction along the geomagnetic field.

2.1. Simultaneous generation of δn and δB_o

In the presence of microwave electric fields electrons experience nonlinear forces, which can give rise to a time-average apparent electric field (E_{app}). The apparent electric field stems primarily from two kinds of nonlinear forces, the radiation pressure force (f_r) and the thermal pressure force (f_{th}). They act on electrons additively leading to electron plasma density fluctuations, δn_e according to the

Radiation pressure (P_r) is equal to the time-average Poynting vector (P_{ave}) divided by the speed of light in vacuum (see, e.g., Shen and Kong 1995), and the force caused by this pressure is given by $\mathbf{f_r} = -\nabla(P_r)$. Thermal pressure force $\mathbf{f_{th}} = -\nabla(n_e k_B \delta T_e)$ where n_e, k_B and δT_e stand for the background plasma density, Boltzmann constant and the temperature perturbations due to electron heating. In other words, electron collisions cause temperature perturbations (δT_e) that lead to the thermal pressure force. More details on electron collisions and temperature effects are explained in section 3. Under the $\mathbf{E_{app}} \times \mathbf{B_o}$ drift of electrons an electric current $(\delta \mathbf{J}_{E\times B})$ results, which produces Earth magnetic field fluctuations $(\delta \mathbf{B_o})$ according to the Ampere's law:

$$\nabla \times \delta B_o = \mu_o \delta J_{E\times B}.$$

2.2. Three-wave interaction

The aforementioned physical processes can be described in terms of a three-wave interaction process. Figure 3 shows that the incident (mother) microwave denoted by its wave vector $(\mathbf{k}_o)$ and wave frequency (ω_o), generates a daughter HF wave (k_o^t, ω_o^t) and a daughter low-frequency plasma mode (k_I, ω_I). The low-frequency plasma mode is an electrostatic wave associated with δn_e, having a nearly zero frequency. After this low-frequency mode is induced, the $\mathbf{E_{app}} \times \mathbf{B_o}$ drift of these perturbed electrons (δn_e) yields the current perturbations (δJ) that then lead to the magnetic field fluctuations (δB_o).

For this three-wave interaction process, there are two matching conditions to be satisfied. One is the wave-frequency matching condition, which requires the incident 'mother' wave frequency be equal to the sum of the daughter wave

o
ι

and plasma mode frequencies ($\omega_o = \omega^t + \omega_I$). The other is the wave-vector matching condition ($\mathbf{k_o} = \mathbf{k_o} + \mathbf{k_I}$).

2.3. Configurations of induced plasma density irregularities

In our earlier experiments at Arecibo, Puerto Rico (Lee *et al* 1998, Pradipta *et al* 2008) ionospheric density fluctuations (or known as irregularities), in the form of parallel-plate waveguides, were generated by HF heater waves via the thermal filamentation instability. They were

$\mathbf{B_o}$

Figure 4. 'Filament' type structure of microwave-generated ionospheric ducts/waveguides.

detected by 430 MHz radar and seen as slanted stripes on the range-time-intensity (RTI) plot (see figure 3 of Lee *et al* 1998). Further investigation on the thermal filamentation instability in generating HF wave-induced ionospheric ducts (i.e. parallel-plate waveguides) have been conducted at Gakona, Alaska using High-frequency Aurora Active Research Program (HAARP) HF heater after Arecibo HF heater was damaged by Hurricane Georges in 1998. Our recent HF wave injection experiments at Gakona, Alaska, supported by multi-diagnostic instruments including MUIR (at 446 MHz) radar, magnetometer, digisonde and GPS satellites, not only successfully reproduced Arecibo results but also confirmed the prediction of the simultaneous generation of ionospheric plasma density irregularities (δn_e) and geomagnetic field fluctuations (δB_o) (Cohen *et al* 2010).

The reason for the two types of HF heater waves to generate different configurations of ionospheric ducts/parallel plate waveguides is given here. Near their reflection heights O- and X-mode HF heater waves propagate across and along the geomagnetic field, respectively. The O- and X-mode HF heater wave-created large plasma sheets are associated with electrostatic density irregularities (δn_e) with wave vectors, represented by k° and k^x, respectively. Note that k° and k^x are $_I$ $_I$ perpendicular and parallel to the meridian plane, respectively, indicating that the induced plasma sheets are within and orthogonal to the meridian plane correspondingly (see figure 1 of Lee *et al* 1998).

However, the microwaves (e.g. 2.45 GHz) under the current investigation have wave frequency exceeding the electron cyclotron frequency (~1 MHz) by three orders of magnitude. Hence, the birefringent effect (i.e. splitting of two

component waves from its linearly polarized mode) is negligible. Therefore, $k_{\parallel}$ of induced large-scale filed-aligned modes can be any direction around the geomagnetic
field. We then expect that microwave-generated ionospheric ducts/waveguides have the 'filament type of structure,' as delineated in figure 4, awaiting corroboration in our future experiments.

3. Evaluations of microwave-induced ionospheric effects

3.1. Mechanisms imposing instability thresholds

The concerned plasma instability induced by microwaves has a threshold imposed by electron collisions and diffusion

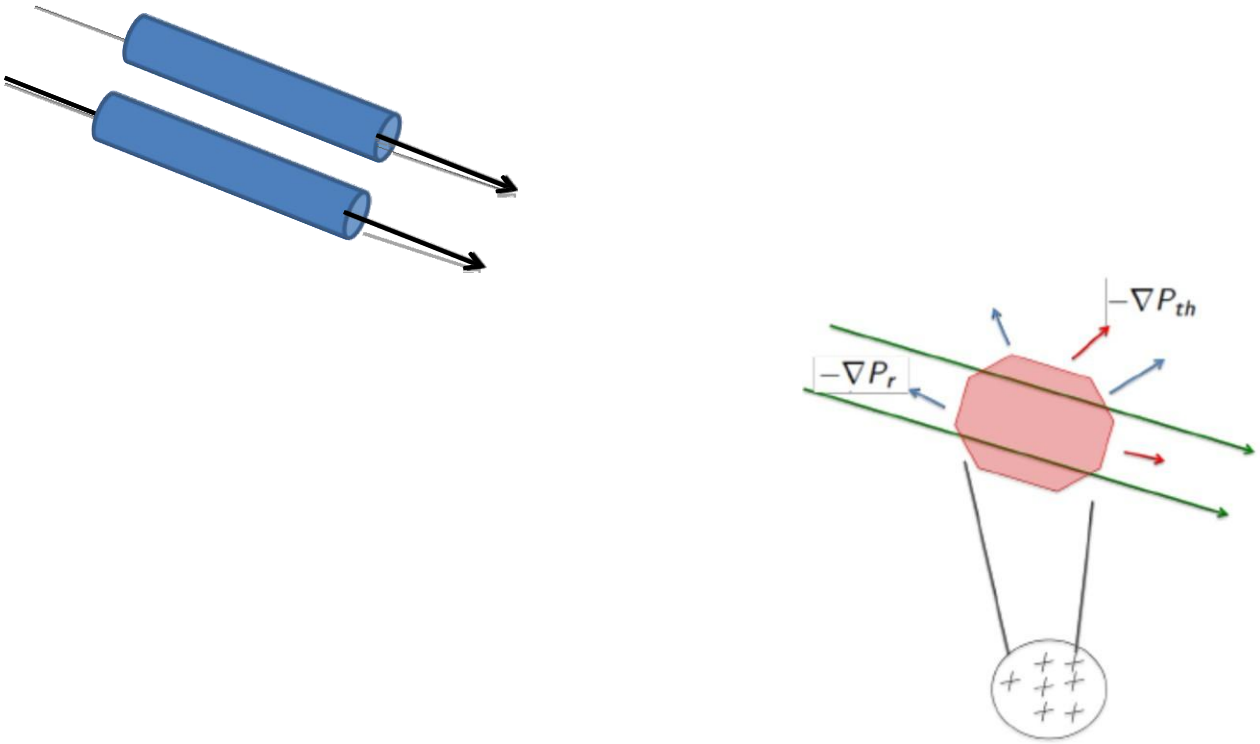

Figure 5. Microwave antenna array illuminates the ionosphere, leading to thermal pressure force and radiation pressure force acting on electrons.

loss. In figure 5, the region under illumination by microwave radiation is represented by the red-shaded area. In this region, as aforementioned, there are two kinds of forces acting on electrons, the thermal pressure force denoted by the red arrows and the radiation pressure force by the blue arrows. Under the influence of these forces, electron collisions play several different roles in the microwave illuminated ionosphere, as elaborated here with the aid of figure 5.

Firstly, electron collisions produce a heat source that gives rise to the thermal pressure force. Secondly, they impose a damping mechanism on the excited low-frequency mode. Finally, they can reduce the heat conduction loss along the Earth's magnetic field. This last aspect can be understood as follows. The microwave-illuminated ionospheric region is full of heated electrons surrounded by many neutral particles, especially, in ionospheric E region. The motion of hot electrons along the Earth's magnetic field will be hindered by those neutrals, as depicted in figure 6. Heated electrons moving to escape the area will be reflected back, heat conduction loss can, therefore, be reduced by electron collisions. Electrons can easily move along magnetic field lines, therefore, heat conduction loss of electrons occurs mainly along geomagnetic field lines. Consequently, diffusion loss reduces the effect of the thermal pressure force, and thus, also is a factor to impose the instability threshold.

Due to the crucial roles of electron collisions in microwave–ionospheric plasma interactions, we examine the sources for electron collisions (ν_e) as follows. It consists of two parts, electron–neutral collision (ν_{en}) and electron–ion collisions (ν_{ei}), that is, $\nu_e = \nu_{en} + \nu_{ei}$. In the E region (90–120 km above Earth's surface), the electron–neutral collisions (ν_{en}) dominate, while in the F region (above 120 km from Earth's surface), electron–ion collisions (ν_{ei}) dominate. Based on table 1, we expect that the ionospheric

E region is the main ionospheric region of concern. This is because, for approximately same electron densities (n_e), electron collisions (ν_e) in the E region are much higher than those in the F region.

Table 2. Assessment of damping mechanisms.

	Collisional	Cross-field damping	Parallel damping	thermal diffusion
				$\frac{m_e}{M_i}$
	$k_\perp^2 v_{te}^2$			
	ω_{ce}^2			
	$k_\parallel^2 v_{te}^2$			
	ν_{ei}^2			
E region	$\sim 2.0 \times 10^{-5}$	$\sim 7.0 \times 10^{-9}$	$\sim 1.0 \times 10^{-10}$	
F region	$\sim 3.3 \times 10^{-5}$	$\sim 7.0 \times 10^{-9}$	$\sim 1.0 \times 10^{-4}$	

Where $\frac{m_e}{M_i}$ for NO+ (E region), $\frac{m_e}{M_i}$ for O+ (F region), $\frac{\omega_{ce}}{2\pi} = 1.3\,\text{MHz}$, $v_{te} = 1.3 \times 10^5\,\text{m s}^{-1}$ (for $T_e = 1000\,\text{K}$), ν_e (E region)=1 MHz, ν_e (F region)=1 kHz.

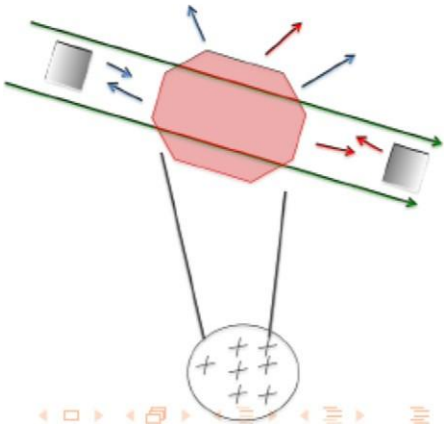

Figure 6. Reflection of electrons back into the region of illumination reduces heat conduction loss.

excitation of large-scale ionospheric ducts, in the range of scale lengths from hundred meters to kilometers.

3.2.1. Ionospheric E region. We assume the excitation

Table 1. Electron densities (n_e), dominant electron collision frequencies (ν_{en} or ν_{ei}) and neutral densities (n_n) in ionospheric E

of 500 meter-scale ducts (i.e., $\lambda_\perp$

$= 5\,\text{km}$, $\lambda_{||}$

$= \sim 14\,\text{km}$)

---

and F regions (Rishbeth and Garriott 1969).

	E region (90–120 km)	F region (120 km–above)
	$\nu_{en} \sim 10^6$ Hz	$\nu_{ei} < 10^3$ Hz

to assess those damping mechanisms under the typical E region conditions: $m_e/M_i\ (NO^+) = 1/(30 \times 1840)$, $v_{te} = 1.3 \times 10^5\,\text{m s}^{-1}$ (for $T_e = 1000$ K), $\omega_{ce}/2\pi = 1.3$ MHz, and $\nu_e = 1.0$ MHz. Then, we obtain (i) $m_e/M_i = 2.0 \times 10^{-5}$,

$n_e \sim 10^{9-10}\,\text{m}^{-3}$	$n_e \sim 10^{11}\,\text{m}^{-3}$	

(ii) $k^2 v^2/\omega^2$

7.0

10^{-9} and (iii) $k^2 v^2/\nu^2$

1.0

10^{-10}

$n_n \sim 1.2 \times 10^{19}$	$n_n \sim 7.6 \times 10^{15}\,\text{m}^{-3}\,\text{m}^{-3}$	

$\perp$ te

ce = ×

|| te e = ×

3.2. Assessments of damping mechanisms

As discussed in the previous section, electron collisions play multiple roles in exciting the thermal filamentation instability during microwave interactions with ionospheric plasmas. On the one hand electron collisions create the thermal source for the instability; on the other hand they impose collisional damping. However, electron collisions can reduce diffusion loss, especially the parallel diffusion loss. We estimate the

(listed in table 2 above). One can see that collisional damping is the dominant mechanism among those three.

3.2.2. Ionospheric F region. Now we examine those damping mechanisms under the following typical F region conditions, to assess the excitation of 500 meter-scale ducts: $m_e/M_i\ (O^+) = 1/(16 \times 1840)$, $v_{te} = 1.3 \times 10^5\,\text{m s}^{-1}$ (for $T_e = 1000$ K), $\omega_{ce}/2\pi = 1.3$ MHz, and $\nu_e = 1.0$ kHz. Then, we obtain (i) $m_e/M_i = 3.3 \times 10^{-5}$ (slightly greater than that in E region), (ii) $k^2 v^2$ 2 −9

$\perp$ te$/\omega_{ce} = 7.0 \times 10$

(same as that in

key damping mechanisms as follows. They are (i) collisional

E region) and (iii) k^2v^2 ^{2} $^{-4}$

$_{||\ te}/\nu_e = 1.0 \times 10$

(much greater than

damping, (ii) cross-field diffusion and (iii) parallel thermal diffusion loss, represented, respectively, by the expressions

that in E region) (listed in table 2 above). It is seen that the parallel diffusion loss even exceeds the collisional damping

of (i) m_e/M_i, (ii) $k^2 v^2/\omega^2$

$[= (2\pi)^2(r_{ce}/\lambda$

$)^2]$ and

for the excitation of kilometer-scale modes. These results

$_{\perp\ te\quad ce\qquad\qquad\qquad\perp}$

(iii) $k_{||}^2 v_{te}^2/\nu_e^2$

$[= (2\pi)^2(\lambda_{mfp})/\lambda_{||})^2]$ where m_e/M_i, k

$_\perp$ show that the thermal filamentation instability of microwaves cannot occur in ionospheric F region primarily because of the

$(= 2\pi/\lambda_\perp)$, $k_{||}$ $(= 2\pi/\lambda_{||})$, $\lambda_\perp$, $\lambda_{||}$, ν_{te}, ω_{ce}, r_{ce}, ν_e and λ_{mfp} are electron to ion mass ratio, irregularity perpendicular wave number, irregularity parallel wave number, perpendicular scalelength, parallel scalelength, electron thermal velocity, electron cyclotron frequency, electron gyro-radius, electron collision frequency and electron mean free path, respectively.

For 'coherent' microwave interactions with ionospheric plasmas, $\lambda_\perp$ and $\lambda_{||}$ are the expected scale lengths of those microwave wave-induced filament-shaped ducts. However, it should be pointed out that the parallel scale length ($\lambda_{||} =$

larger parallel diffusion loss.

3.3. Estimates of instability thresholds

If electron collisions impose the primary damping mechanism, the threshold field $(|E_{th}|)$ to excite the thermal filamentation instability is given by $|eE_{th}/mc| = 0.85\times (f_o/f_{pe})(2\pi/\lambda_\perp)(v_{te})(2m/M_i)1/2$ where the aforementioned E region parameters are adopted, i.e. $\lambda_\perp = 5$ km,

$2\pi/k_{||})$ is determined by the cross-section of the microwave

$\nu_{te} = 1.3 \times 105\,\mathrm{m\,s}^-$

^{1}, m/M_i

$(NO^+) = 1/(30 \times 1840)$, c

beam. For example, if we assume that the linear dimension (D) of the microwave wave cross-section in the ionosphere is 10 km, and the microwave beam has an angle of 60° with respect to the Earth's magnetic field, then, the parallel scale length of induced ionospheric ducts is $\lambda_{||} = D/\sin(60°) = \sim$ 14 km. Given the microwave beam-imposed $\lambda_{||} = \sim$14 km, the highly field-aligned ionospheric ducts would not have a

perpendicular scale length ($\lambda_\perp$) exceeding 5 km. We adopt relevant plasma parameters to evaluate these damping factors in ionospheric E and F regions separately below, for the

is the speed of light in vacuum, and the microwave frequency (f_o) and electron plasma frequency (f_{pe}) are taken to be

2.45 GHz and 2 MHz, respectively (Lee 2009). Then, the threshold field $|E_{th}|$ is found to be $\sim 0.5\,\mathrm{V\,m^{-1}}$. Because the threshold field is inversely proportional to the perpendicular

scale length ($\lambda_\perp$) of the excited density/magnetic field fluctuations/irregularities, i.e. $|E_{th}| \propto 1/\lambda_\perp$, it requires higher thresholds to excite the smaller-scale instabilities, for example, $5\,\mathrm{V\,m^{-1}}$ for 500 meter-scale and $50\,\mathrm{V\,m^{-1}}$ for 50 meter-scale modes.

the ionospheric E region, but not in the ionospheric F region primarily because of different parallel diffusion loss.

The prominent role of electron collisions can be seen in the parallel diffusion process, described by k^2v^2/v^2

|| te e

||

$[= (2\pi)^2(\lambda_{mfp})/\lambda)^2]$ where λ

mfp

is the mean-free path. In the F region, $v_e \approx v_{ei}$ (electron–ion collision frequency), e.g. ~1 kHz and the corresponding $\lambda_{mfp} \sim 130$ m. By contrast, $v_e \approx v_{ei}$ (electron–neutral collision frequency), e.g. ~1 MHz in the E region, thus, $\lambda_{mfp} \sim 0.13$ m. One can see that large electron collision frequency will effectively reduce the parallel diffusion loss. For comparison, the cross-field

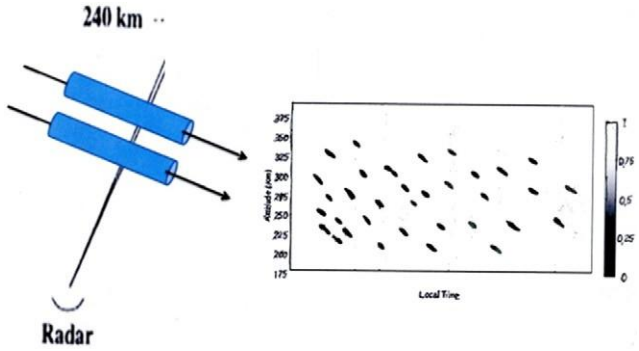

diffusion is given by $k^2 v^2/\omega^2$

$[= (2\pi)^2(r_{ce}/\lambda$

$)^2]$ where

Figure 7. Arecibo 430 MHz radar detection of filament-type of δn,

r is the electron

⊥ te ce

⊥

the

For

ce gyro-radius and $\lambda_\perp$

scalelength.

which undertakes E × B drifts across the radar beam, would be seen as dashed lines in the RTI plots.

large-scale modes the ratio $r_{ce}/\lambda_\perp$

can be rather small, leading

4. Diagnoses of predicted ionospheric plasma effects

As delineated in figure 4, we expect that the microwave- generated ionospheric ducts/waveguides have the 'filament type of structure', for corroboration in our future Arecibo experiments. The proposed Arecibo radar diagnosis of predicted ionospheric plasma effects is briefly described below (Whitehurst and Lee 2012). Arecibo 2.38 GHz is operated in full power as the 'microwave pump' to heat the ionosphere. The heated ionospheric E region is expected to have a dimension of a few kilometers along the geomagnetic field for a magnetic dip angle of 45°. The subsequent diagnostics can be carried out by injecting the 430 MHz radar beam from the large spherical dish. This can be simply described using the dual beam scheme for ionospheric heating as well as remote sensing, even if the 2.38 GHz microwave and the 430 MHz radar beam are injected from separate transmitters. The predicted filament-like plasma density irregularities can be detected by Arecibo 430 MHz radar in the following. They would appear as dashed lines in the RTI (range-time-intensity) plots delineated in figure 7, provided that quasi-dc electric fields due to dynamo effect appear above Arecibo, leading to E × B drifts of the filament-like structures.

This feature is distinctively different from the slanted stripe structures in the RTI plots, resulting from detection of HF (i.e. a few MHz) heater-excited sheet-like (i.e. parallel-plate type) irregularities, as observed in our 1997 Arecibo experiments (see figure 3 of Lee *et al* 1998). Moreover, we can use GPS satellites, optical instruments and GeoMagnetic Observatory System to detect the microwave-induced filaments of plasma density irregularities in our future experiments at Arecibo, Puerto Rico.

5. Summary and conclusions

We briefly summarize the main results as follows. The theoretical study we carried out for microwave interactions with space plasmas shows that electron collisions play multi-roles. Electron collisions create the thermal source during microwave–ionospheric interactions to drive the thermal filamentation instability. Meanwhile, they impose collisional damping as the major mechanism to impose the thresholds for the excitation of the thermal instability. It is expected that significant microwave interactions can occur in

to negligible cross-field diffusion loss.

To avoid possible disturbances to the Earth's atmospheric environment, high-power microwave transmission should not exceed certain power limits. For example, the wave field intensity in the ionosphere should not be greater than the threshold field intensity ($\sim 0.5\ \mathrm{V\ m^{-1}}$). It is predicted that filament-like plasma density irregularities can be excited by microwaves in contrast to the generation of parallel-plate structures by HF waves for future experiments to corroborate. We plan to test our predicted microwave wave–ionospheric E region interactions, using Arecibo microwave radar at 2.38 GHz and UHF radar at 430 MHz aided by our own and Arecibo optical instruments.

Acknowledgments

This work was supported by AFOSR grant FA9550-09-1-0391. A portion of this paper was presented by M C Lee as an invited paper and by R Pradipta *et al* in a poster paper at the Third International Conference on 'Turbulent Mixing and Beyond', Abdus Salam International Centre for Theoretical Physics (ICTP), Trieste, Italy, 21–28 August 2010.

References Q2

Cohen J A *et al* 2010 Generation of ionospheric ducts by the HAARP HF heater *Phys. Scr.* **T142** 014040 (7pp) doi:10.1088/0031-8949/2010/T142/014040

Lee M C 2009 Controlled study of ionospheric plasma turbulence in radio wave injection experiments, Invited Talk in *2nd Int. Conf. on 'Turbulent Mixing and Beyond' Abdus Salam International Centre for Theoretical Physics (ICTP)* Trieste, Italy, 27 July-7 August 2009

Lee M C *et al* 2012 Investigation of naturally occurring and radio wave-induced ionospheric plasma turbulence *39th IEEE Int. Conf. Plasma Science* Edinburgh, Scotland, 8-12 July 2012

Lee M C, Riddolls R J, Burke W J, Sulzer M P, Kuo S P and Klien E M C 1998 Generation of large sheet-like ionospheric plasma irregularities at Arecibo *Geophys. Res. Lett.* **25** 3067

Pradipta R *et al* 2008 Space plasma disturbances caused by NAU-launched whistler waves *Phys. Scr.* **T132** 014031 doi:10.1088/0031-8949/2008/T132/014031

Rishbeth H and Garriott O 1969 *Introduction to Ionospheric Physics* vol 14 (New York/London: Academic) pp vii–331

Shen L C and Kong J A 1995 *Applied Electromagnetism* 3rd edn (Boston, MA: PWS Publishing Co.)

Whitehurst L N and Lee M C 2012 Solar powered microwave transmission and interactions with atmospheric plasmas Student Paper Contest, *39th IEEE Int. Conf. Plasma Science* Edinburgh, Scotland, UK, 9-12 July 2012

5

Appendix F.

Direct Acceleration of Ionospheric Electrons by 40.75 kHz Whistler Waves Over Arecibo

L.A. Rooker[1], M.C. Lee[1,2], R. Pradipta[2], L.M. Ross[1,3], B.Z. See[1], M.J. Sulzer[4], C. Tepley[4], S. Gonzalez[4], N. Aponde[4], S.P. Kuo[5]

1. Department of Electrical & Computer Engineering, Boston University, Boston, MA 02215, USA
2. Space Propulsion Lab, Massachusetts Institute of Technology (MIT), Cambridge, MA 02139, USA
3. M.I.T. Lincoln Laboratory, Lexington, MA 02421, USA
4. Arecibo Observatory, Arecibo, PR 00612, USA
5. Polytechnic Institute of New York University, Brooklyn NY 11201, USA

Abstract

A new mechanism is proposed for the direct acceleration of ionospheric electrons by whistler waves. It is suggested as the key process responsible for our reported enhanced plasma lines detected by the Arecibo 430 MHz radar. These plasma lines are characterized by the frequency-downshifted spectra with a bandwidth of ~ 12 kHz. From the backscatter radar operation, it indicates that electrons were accelerated upward along the Earth's magnetic field by the up-going 40.75 kHz whistler waves, which were launched from the NAU transmitter. They covered a broad range of altitudes (~ 300 km) and lasted for a period of a few minutes. This mechanism leads to the energization of electrons of ~ 13 eV inferred from Arecibo experiments.

1. Introduction

In the past eight years or so, we have been conducting Arecibo experiments in Puerto Rico for the controlled study of whistler wave interactions with ionospheric plasmas [Labno et al., 2007] and inner radiation belts at L = 1.35 [Pradipta et al., 2007]. The main source for the whistler waves is a Naval transmitter code-named NAU, which is located nearby at Aguada, Puerto Rico, emitting radio waves at a power and frequency of 100 kW and 40.75 kHz, respectively. We estimated that ~7.5% of NAU transmitted power could be coupled into the ionosphere via refraction and mode conversion. Large-scale ionospheric plasma density irregularities would facilitate the entering of NAU-launched whistler waves from the neutral atmosphere into the ionosphere. These ionospheric density irregularities can occur naturally during spread F events or be induced by HF heater waves.

Large-scale ionospheric irregularities typically refer to those with scale lengths in the range of hundred meters to kilometers. In our 1997 HF heating experiments, we demonstrated that the Arecibo HF heater can create artificial ionospheric ducts for controlled conjugate whistler wave propagation between Arecibo, Puerto Rico and Trelew, Argentina [Starks et al., 2001]. These O-mode (X-mode) HF heater wave-induced ionospheric ducts appeared in the form of parallel-plate waveguides within (orthogonal to) the meridional plane [Lee et al., 1998; Cohen et al., 2010]. However, without an HF heater at Arecibo in the past decade, we have been relying on naturally-occurring ionospheric irregularities for experiments to investigate NAU-launched whistler wave interactions with space plasmas.

The Arecibo 430 MHz radar has provided powerful diagnosis of ionospheric plasma effects induced by NAU transmission directly in the ionosphere [Labno et al., 2007] or by downward streaming 390 keV electrons knocked down by NAU signals from the radiation belts [Pradipta et al., 2007]. The ionospheric plasma effects caused by NAU transmission can be analyzed from the measurements of enhanced plasma lines as illustrated in Figure 1. From the backscatter radar operation, if plasma lines arise from radar-detected beam modes associated with downward streaming electrons, then the preferentially detected plasma waves are expected to yield frequency-upshifted plasma lines due to the Doppler effect. However, as shown in Section 2, enhanced plasma lines with frequency-downshifted spectra were exclusively measured in our summer 2008 experiments. The characteristic features of these frequency-downshifted plasma lines are highlighted in Section 3. A new mechanism to understand this intriguing phenomenon and to explain how NAU-launched whistler waves can accelerate ionosphere electrons upward along the Earth's magnetic field is presented in Section 4. Discussions are given and conclusions are finally drawn in Section 5.

2. Enhanced Plasma Lines in Ionospheric F region

As reported in our earlier work [Labno et al., 2007], we believe that NAU launched whistler waves are intense enough to excite lower hybrid waves and field-aligned zero-frequency plasma density striations via a four wave interaction process in ionospheric F region. This process can be understood in terms of a diagram shown in Figure 2. The required wave frequency and wave vector matching conditions are given below.

$$\omega_o = \omega^{+}_{\ell h} - \omega_s, \quad \omega_o = \omega^{-}_{\ell h} + \omega^{*}_{s}, \quad \mathbf{k_o} = \mathbf{k_+} - \mathbf{k_S}, \quad \mathbf{k_o} = \mathbf{k_-} + \mathbf{k_S} \qquad (1)$$

where (ω_o, $\mathbf{k_o}$) stands for the VLF whistler wave, ($\omega^{-}_{\ell h}$, $\mathbf{k_-}$) for the Stokes lower hybrid waves, ($\omega^{+}_{\ell h,}$ $\mathbf{k_+}$) for the anti-Stokes lower hybrid waves, and (ω_s, $\mathbf{k_S}$) for the zero-frequency field-aligned density irregularities.

Note that the wave vector ($\mathbf{k_S}$) of the zero-frequency mode has two components, one across ($\mathbf{k_{S\perp}}$) and the other along ($\mathbf{k_{S\|}}$) the geomagnetic field. It is justified for Labno et al. [2007] to assume that $\mathbf{k_+} \approx \mathbf{k_S}$ and $\mathbf{k_-} \approx -\mathbf{k_S}$ in the wave frequency and wave vector matching conditions [Eq. (1)], because meter-scale density irregularities have their $k_{S\|} >> k_o$ of the 40.75 kHz whistler wave. Hence, as depicted in Figure 2, the excited lower hybrid waves in either scenario/case can have both upward and downward wave vectors for Stokes or anti-Stokes components. It means that electrons can be accelerated equally likely upward and downward according to the mechanism proposed by Labno et al. [2007]. This mechanism explains well the detection of enhanced plasma lines in the F region with both frequency-upshifted and frequency-downshifted features.

However, enhanced plasma lines with frequency-downshifted spectra were exclusively measured in our summer 2008 experiments at Arecibo with the radar transmitted vertically via the

stationary linefeed. Plasma line measurements were recorded using a coded-long pulse technique to detect whistler wave-plasma interactions in the altitude range of 90 to 645 km. Additionally, ionograms were recorded every five minutes to monitor the background plasma conditions. A VLF receiver was deployed to track whether the NAU transmitter was on or off. NAU-generated 40.75 kHz waves were detected continuously during the entire experiment. Displayed in Figure 3 is a series of enhanced plasma line data recorded on August 4/5, 2008.

3. Characteristic Features of Enhanced Plasma Lines

These frequency-upshifted plasma lines have outstanding features distinctively different from those observed in our December 2004 experiments [Labno et. al., 2007], as highlighted below.

(1) In our earlier experiments Arecibo radar could only detect "upshifted" plasma lines, corresponding to plasma modes generated by down-going electrons [Labno et. al., 2007]. Now although the radar has the capability to detect both upshifted and downshifted plasma lines, we only measured "downshifted" plasma lines in our Summer 2008 experiments.

(2) These "downshifted" plasma lines have a rather narrow frequency bandwidth (~12 kHz) around 4.5 MHz compared to 1.5 MHz of those plasma lines centered at 4 MHz reported in Labno et al. [2007]. These "downshifted" plasma lines have significantly weaker intensities.

(3) They covered a much broader range of altitudes (~ 300 km) than that of F-region plasma lines (~ 120 km) seen in Dec. 2004 experiments.

(4) They last for a much longer period of time (> a few minutes) than those (< 10 seconds) reported in Labno et al. [2007].

(5) They occurred during the continuously descending of F-region layer in the process of strong developing spread F [see attached RTI plot in Figure 4].

Contrastingly, F-region plasma line enhancement was detected on Dec. 20/21 & Dec. 26, 2004 [Labno et al., 2007] when the F-region layer was quite stable.

(6) We have ASIS (showing 6300 A and more intense 5577 A airglows) and Fabry-Perot data, indicate eastward and downward plasma drifting.

4. A New Source Mechanism

Based on above noticed features from radio and optical diagnostics, we propose the following source mechanism, as depicted in Figure 5.

The distinctive difference between this new mechanism and that of Labno et al. [2007] has the following four aspects.

(1) Wave vector matching conditions

In this new mechanism: $\mathbf{k}_{+||} = \mathbf{k}_o$, $\mathbf{k}_{+\perp} = \mathbf{k}_S$, and $\mathbf{k}_{-||} = \mathbf{k}_o$, $\mathbf{k}_{-\perp} = -\mathbf{k}_S$,

while in Labno et al [2007]: $\mathbf{k}_{+||} = \mathbf{k}_S$, and $\mathbf{k}_{-||} = -\mathbf{k}_S$.

(2) Scale lengths of excited lower hybrid waves and zero-frequency modes

In this proposed mechanism: ten-meter (e.g., 15 m) scale electrostatic wave/modes are excited, while in Labno et al [2007]: meter-scale (e.g., 1.5 m) wave modes are excited.

(3) Preferred directions to accelerate ionospheric electrons

In this new physical process electrons are preferentially accelerated upward with the up-propagating NAU-launched whistler waves, as depicted in Figure 5. Contrastingly, electrons can be equally likely accelerated in upward and downward directions, as illustrated in Figure 2.

(4) Energies of accelerated electrons

Based on the frequency spectra of measured plasma lines, the proposed mechanism accelerates ionospheric electrons in the phase energy range of ~ $13.0 \pm 1.2 \times 10^{-5}$ eV, while the mechanism of Labno et al. [2007] energizes electrons in the range of 7.2 – 15 eV.

In summary, the proposed mechanism is the direct acceleration of electrons by the parallel whistler wave electric field. This mechanism can explain the upward streaming electrons that can only lead to the radar detection of "downshifted" plasma lines with narrow frequency bandwidth. This process occurs in a much broader range of altitudes (several hundred km). Thus, NAU whistler waves will deposit significant energy in F region before they propagate into radiation belts.

4. Discussions and Conclusions

We propose that upward propagating, NAU launched, 40.75 kHz, whistler waves can accelerate ionospheric electrons upwards along the background magnetic field via a new source mechanism. This process can cause the downshifted plasma line enhancement detected by the Arecibo 430 MHz radar. This new mechanism has a striking feature distinguishing it from that of Labno et al. [2007], that is, the excited Stokes and anti-Stokes lower hybrid waves have their parallel wave vectors equal to the upward whistler wave vector. Hence, it is a "direct acceleration of electrons by whistler waves", contrasting to the mechanism discussed in Labno et al., wherein the wave vectors of whistler wave-excited lower hybrid waves are same as those of concomitantly excited zero-frequency field-aligned modes.

The marked difference between these two mechanisms can also be understood in terms of the scale lengths of their generated lower hybrid waves and zero-frequency modes. While meter-scale (e.g., 1.5 m) electrostatic plasma modes are produced by Labno et al.'s mechanism, the new mechanism creates corresponding plasma mode with ten-meter scale (e.g., 15 m). Consequently, the parallel phase velocities of excited lower hybrid waves to accelerate electrons are ~ 6.1 x 10^5 m/sec in the case of Labno et al. and ~ 1.4 x 10^7 m/sec in our case. Compared to the typical thermal velocity (~ 1.3 x 10^5 m/sec), it is seen that the meter-scale lower hybrid waves can yield bulk acceleration of ionospheric electrons, while the ten-meter scale waves can only accelerate fewer tail electrons. This is consistent with the observations that enhanced plasma lines in Labno et al. are much more intense than those in our case displayed in Figure 3. Finally, we notice that the process discussed in Labno et al. [2007] did not occur in our Aug. 2008 experiments, namely, we did not measure frequency-upshifted plasma lines. This puzzlement can be understood from the fact that the background plasma was so turbulent during

our 2008 experiments. This fact was supported by the RTI plots showing the continuous descending of F-region layer [see Figure 4], as well as both the Fabry-Perot and ASIS (all sky imaging system) data indicating the eastward and downward plasma drifts over Arecibo. Therefore, it is rather difficult for 40.75 kHz whistler waves to excite meter-scale electrostatic plasma modes, which require much higher thresholds in the four wave interaction process.

In conclusion, the proposed mechanism can be based on to explain reasonably the detection of enhanced plasma lines with frequency-downshifted spectra only in our 2008 Arecibo experiments. In the comparison with our earlier experiments to record frequency-upshifted plasma lines [Labno et al., 2007], we can understand how distinctively different features of enhanced plasma lines are caused by these two mechanisms. The favorable operation of these mechanisms depends on the background ionospheric plasma conditions. The one discussed in Labno et al. [2007] has more severe requirements for its occurrence than the proposed one.

Acknowledgments. This work was supported by AFOSR grant FA9550-09-1-0391. A portion of this paper was presented by the first author L.A. Rooker for student paper contest at the 39th IEEE International Conference on Plasma Science, Edinburgh, Scotland, 9 - 12 July 2012. L.A. Rooker's summer research and travel was supported by Lutchen Fellowship of College of Engineering, Boston University.

References

Carlson, H. C., V. B. Wickwar, and G. P. Mantas, "Observations of fluxes of suprathermal electrons accelerated by HF excited instabilities", J. Atmos. Terr. Phys., 44, 1089, 1982.

Cohen, J. A., R. Pradipta, L. M. Burton, A. Labno, M. C. Lee, B. J. Watkins, C. Fallen, S. P.

Kuo, W J Burke, D Mabius, and B Z See, "Generation of ionospheric ducts by the HAARP HF heater", Phys. Scr. **T142** (2010) 014040 (7pp) doi:10.1088/0031-8949/2010/T142/014040.

Labno, A., R. Pradipta, M. C. Lee, M. P. Sulzer, L. M. Burton, J. A. Cohen, S. P. Kuo, D. L. Rokusek, "Whistler-mode wave interactions with ionospheric plasmas over Arecibo", Journal of Geophysical Research, 112, A03306, doi:10.1029/2006JA012089, 2007.

Lee, M.C., Riddolls R J, Burke W J, Sulzer M P, Kuo S P and Klien E M C, "Generation of large sheet-like ionospheric plasma irregularities at Arecibo", Geophys. Res. Lett., **25** 3067, 1998.

Pradipta, R., A. Labno, M. C. Lee, W. J. Burke, M. P. Sulzer, J. A. Cohen, L. M. Burton, S. P. Kuo, D. L. Rokusek, "Electron precipitation from the inner radiation belt above Arecibo", Geophysical Research Letters, 34, L08101, doi:10.1029/2007GL029807, 2007

Starks, M.J., M.C. Lee, and P. Jastrzebski, "Interhemispheric propagation of VLF transmissions in the presence of ionospheric HF heating", Journal of Geophysical Research,106, 5579, 2001.

Figure Captions

Figure 1. Detection of enhanced plasma lines generated by downward streaming electrons in backscatter radar operation mode, satisfying Bragg scattering condition, i.e., $k_{ES} = 2\ k_{radar}$. The phase energy (E_φ) of accelerated electrons can be inferred [Carlson et al., 1982].

Figure 2. Illustration of the four-wave interaction process for the VLF whistler-mode wave (ω_o, $\mathbf{k_o}$) to parametrically excite Stokes ($\omega^-_{\ell h}$, $\mathbf{k}_-$) and anti-Stokes ($\omega^+_{\ell h,}$ $\mathbf{k}_+$) lower hybrid waves together with the zero-frequency, (ω_s, $\mathbf{k_S}$) field-aligned, density irregularities. The excited lower

hybrid waves have a single frequency equal to the VLF whistler wave frequency, but a spectrum of wavelengths.

Figure 3. Compilation of 3D (altitude-frequency-intensity) plots to show plasma line enhancement features. From top left to right we have data recorded at 23:00 (LT), 23:31 (LT), and 00:00 (LT) on Aug. 4/5, 2008, respectively. From bottom left to right, we have data recorded at 00:30 (LT), 01:00 (LT), and 01:31 (LT) on Aug. 5, 2008, respectively.

Figure 4. The Range-Time-Intensity (RTI) plot of backscattered radar echoes showing continuous descending of ionospheric layers during F-region plasma line measurements, which result in data gaps as white stripes on the RTI plot.

Figure 5. Depiction of four-wave interaction process leading to acceleration of electrons upwards along the magnetic field line due to NAU launched whistler waves.

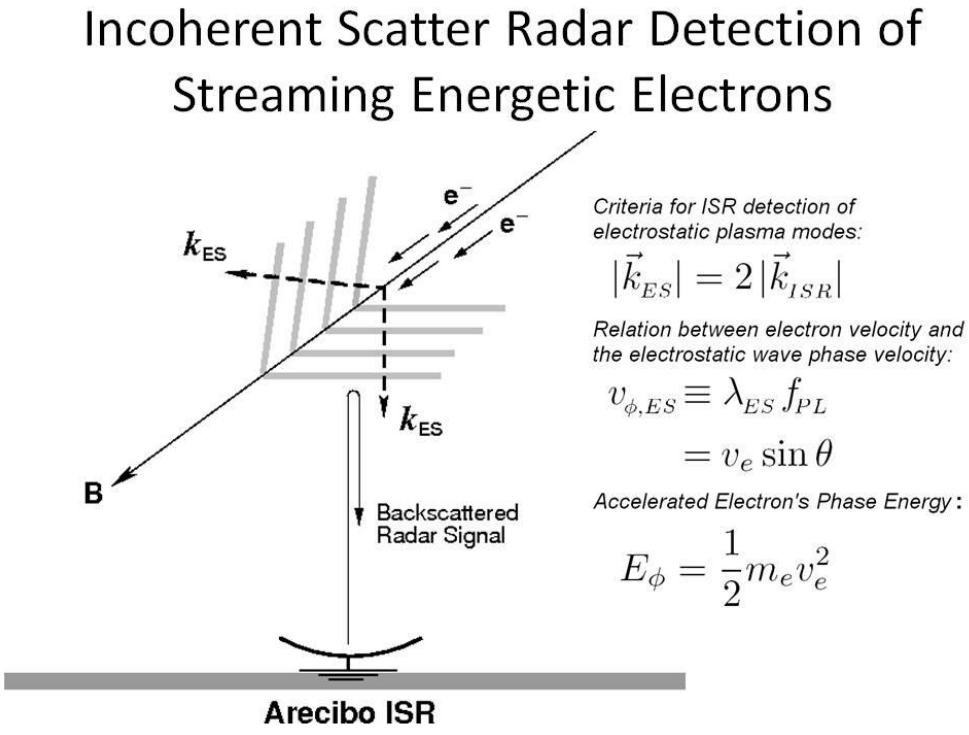

Figure 1. Detection of enhanced plasma lines generated by downward streaming electrons in backscatter radar operation mode, satisfying Bragg scattering condition, i.e., $k_{ES} = 2\ k_{radar}$. The phase energy (E_φ) of accelerated electrons can be inferred [Carlson et al., 1982].

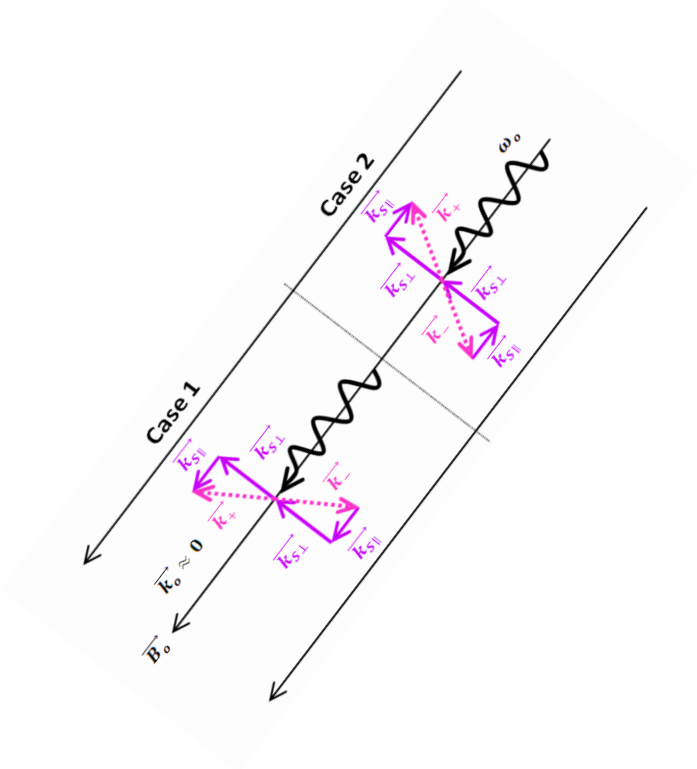

Figure 2. Illustration of the four-wave interaction process for the VLF whistler-mode wave (ω_o, $\mathbf{k_o}$) to parametrically excite Stokes ($\omega^-_{\ell h}$, $\mathbf{k}_-$) and anti-Stokes ($\omega^+_{\ell h,}$ $\mathbf{k}_+$) lower hybrid waves together with the zero-frequency, (ω_s, $\mathbf{k_S}$) field-aligned, density irregularities. The excited lower hybrid waves have a single frequency equal to the VLF whistler wave frequency, but a spectrum of wavelengths.

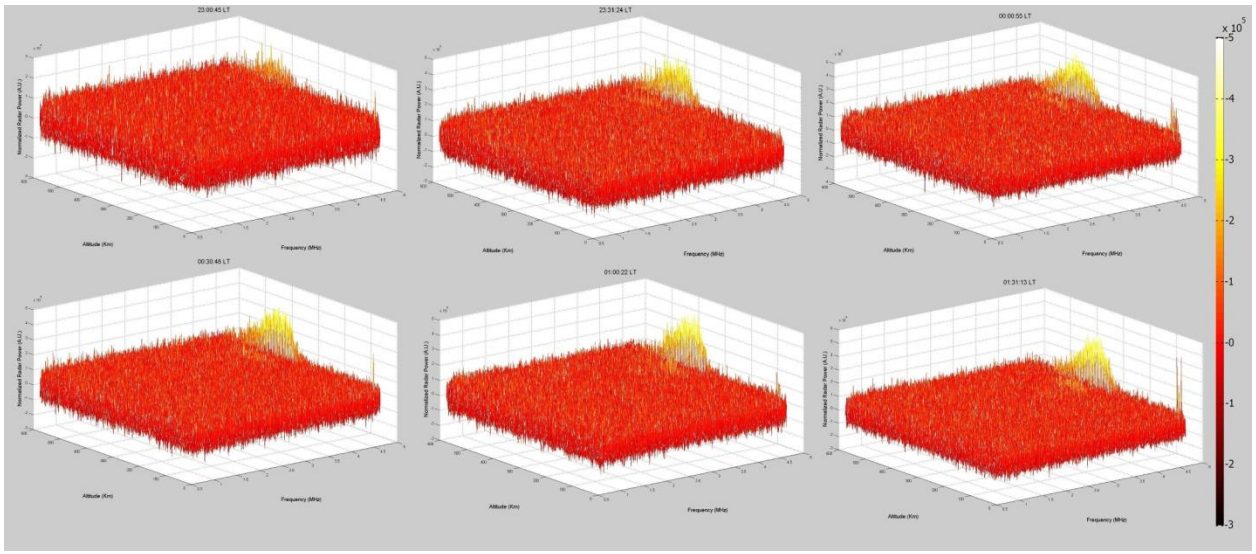

Figure 3. Compilation of 3D (altitude-frequency-intensity) plots to show plasma line enhancement features. From top left to right we have data recorded at 23:00 (LT), 23:31 (LT), and 00:00 (LT) on Aug. 4/5, 2008, respectively. From bottom left to right, we have data recorded at 00:30 (LT), 01:00 (LT), and 01:31 (LT) on Aug. 5, 2008, respectively.

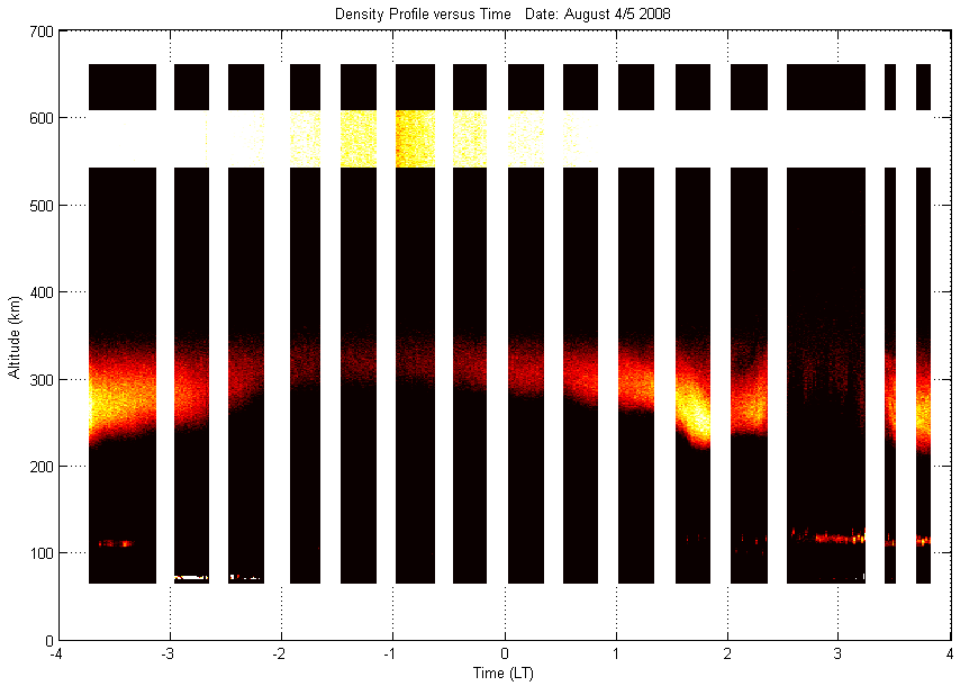

Figure 4. The Range-Time-Intensity (RTI) plot of backscattered radar echoes showing continuous descending of ionospheric layers during F-region plasma line measurements, which result in data gaps as white stripes on the RTI plot.

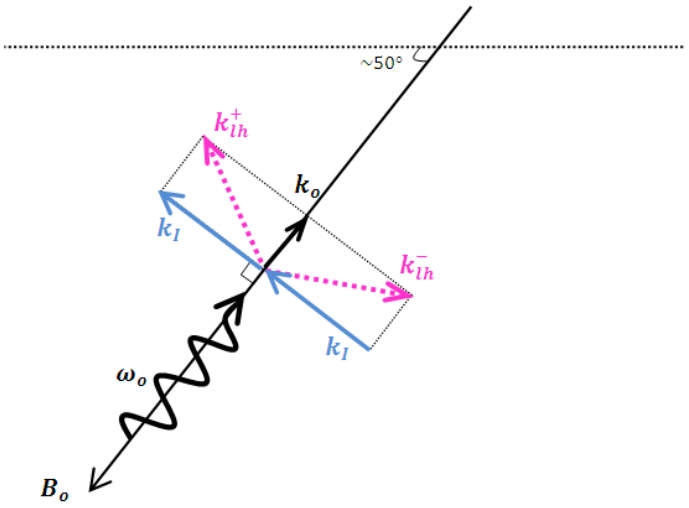

Figure 5. Depiction of four-wave interaction process leading to acceleration of electrons upwards along the magnetic field line due to NAU launched whistler waves.

Appendix G.

Generation and Detection of Whistler Wave Induced Space Plasma Turbulence

L.A. Rooker[1], M.C. Lee[1,2], R. Pradipta[2]

1. Boston University, Boston, MA 02215, USA
2. Massachusetts Institute of Technology, Cambridge, MA 02139, USA

Abstract

We report on HF wave injection experiments using beat wave technique to study the generation of VLF whistler waves in the ionosphere above Gakona, Alaska. This work is aimed at investigating whistler wave interactions with ionospheric plasmas and radiation belts. Beat wave technique involves injecting two X-mode waves at a difference frequency in the VLF range using the HAARP heating facility. A sequence of beat wave-generated whistler waves at 2, 6.5, 7.5, 8.5, 9.5, 11.5, 15.5, 22.5, 28.5, and 40.5 kHz were detected in our 2011 experiments. We present MUIR (446 MHz) radar measurements of ion

lines as the primary diagnosis of ionospheric plasma effects caused by beat wave-generated whistler waves. Magnetometer and digisonde were used to monitor the background ionospheric plasma conditions throughout the experiments. Our theoretical and data analysis show that VLF whistler waves can effectively interact with ionospheric plasmas via two different four-wave interaction processes leading to energization of electrons and ions. These preliminary results support our Arecibo experiments to study NAU-launched 40.75 kHz whistler wave interactions with space plasmas.

1. Introduction

It has been observed in our Arecibo experiments that NAU-launched whistler waves can interact with energetic electrons trapped in the inner radiation belts at L = 1.35 [Pradipta et al., 2007] as well as accelerate electrons in the ionosphere via a four-wave interaction process [Labno et al., 2007]. We recently conducted experiments at Gakona using two HF X-mode waves to explore the beat wave technique for the controlled study of VLF whistler wave interactions with ionospheric plasmas and the outer radiation belts at L = 4.9. A sequence of beat wave-generated whistler waves at 2, 6.5, 7.5, 8.5, 9.5, 11.5, 15.5, 22.5, 28.5, and 40.5 kHz had been successfully detected. Their intensities were greater than those produced by conventional HF wave-modulation of electrojet currents. We present data analysis and theoretical study to show the effectiveness of the newly developed beat wave generation technique for the controlled study of whistler wave interactions with space plasmas. The sequential presentations are (1) detection of beat wave generated whistler waves and (2) whistler wave interactions with ionospheric plasmas and outer radiation belts.

The rest of the paper is organized as follows. In Section 2 we briefly discuss the beat wave generation technique and the theoretical basis. The detection of VLF waves and data recorded in our 2011 experiments using this technique is presented in Section 3. The data includes ground-based measurements of VLF signals, magnetometer, and radar-detected ion lines. These sets of data provide evidence for us to suggest, in Sections 4 and 5, that generated whistler waves can interact with ionospheric plasmas over Gakona via two different kinds of four-wave interactions.

Discussions on whistler wave interactions with outer radiation belts and conclusions are finally drawn in Section 6.

2. Beat Wave Generation of Whistler Waves

We have been conducting experiments to generate VLF whistler waves in the ionosphere above Gakona, Alaska using the HAARP IRI heater array in the past few years [Lee et al., 2010]. In order to create VLF

waves via the beat wave technique, the HF heater array simultaneously transmits two X-mode waves with a difference frequency in the VLF range. For example, transmitting one wave at 3.2 MHz and the other at 3.202 MHz creates an artificial antenna in the ionosphere via ponderomotive force that radiates at the difference frequency of 2 kHz. The force on an electron due to the two HF injected waves is given by:

$$\overrightarrow{F_e} = -e\widehat{E_1}E_1\cos\left[\omega_1 t - \boldsymbol{k_1}\cdot(\vec{r}+\Delta\overrightarrow{x_2})\right] - e\widehat{E_2}E_2\cos\left[\omega_2 t - \boldsymbol{k_2}\cdot(\vec{r}+\Delta\overrightarrow{x_1})\right]$$

where (ω_1, $\mathbf{k_1}$) and (ω_2, $\mathbf{k_2}$) denote the two HF injected waves characterized by their wave frequencies and wave vectors; $\Delta\mathbf{x}$ represents the displacement of the electron oscillating in one wave electric field, as it experiences the force $\mathbf{F_e}$ from the other wave electric field. The quasi-DC component of the experienced electric force $\mathbf{F_e}$ is that at the difference frequency (ω_1 - ω_2) given by:

$$\overrightarrow{F_{NID}} = -\widehat{E_1}(\boldsymbol{k_1}\cdot\widehat{E_2})\frac{e^2E_1E_2}{2m_e\omega_2^2}\sin[(\omega_1-\omega_2)t-(\boldsymbol{k_1}-\boldsymbol{k_2})\cdot\vec{r}\,] + \widehat{E_2}(\boldsymbol{k_2}\cdot\widehat{E_1})\frac{e^2E_1E_2}{2m_e\omega_1^2}\sin[(\omega_1-\omega_2)t-(\boldsymbol{k_1}-\boldsymbol{k_2})\cdot\vec{r}\,]$$

.

It is the ponderomotive force (or loosely called radiation force) responsible for generating the VLF whistler waves from the two injected HF heater waves. It indicates that the efficiency decreases with the difference frequency (ω_1 - ω_2).

3. Detection of Beat Wave Generated VLF Whistler Waves

Beat wave-generated VLF whistler waves with frequencies at 2, 6.5, 7.5, 8.5, 9.5, 11.5, 15.5, 22.5, 28.5, and 40.5 kHz were detected using a VLF receiver setup a few miles away from the HAARP IRI heater array. Figure 1 shows the detection of two cycles of 11.5, 15.5, 22.5, 28.5, and 40.5 kHz waves created using beat wave technique on July 23, 2011 in Gakona, Alaska. Whistler wave field intensity versus wave frequency is given in Figure 2.

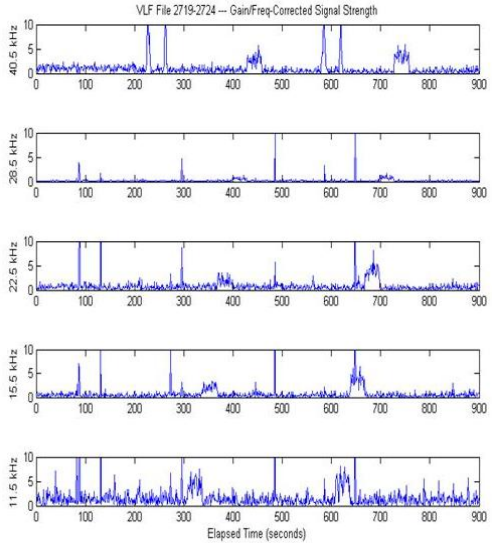

Figure 1. Detection of beat wave generated VLF whistler waves at 11.5, 15.5, 22.5, 28.5, and 40.50 kHz.

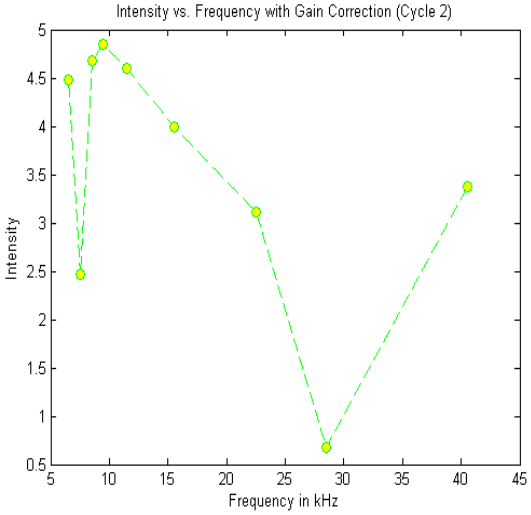

Figure 2. Whistler wave intensity versus wave frequency of those generated VLF whistler waves, showing monotonically decreasing intensity, in General, up to 28.5 kHz.

Generally, the generation efficiency is consistent with expected dependence of ponderomotive force on the difference frequency (ω_1 - ω_2) up to 28.5 kHz. The discrepancy from the expected monotonic decreasing of wave intensity may be attributed to possible beat wave interactions with electrojet currents. We notice that the presence of electrojet currents in our experiments, marked in green rectangular box in Figure 3, may affect beat wave generation of whistler waves as well as the background plasma conditions. Shown in Figure 4 is an enhanced zero-frequency mode, seen as a central line in the radar detected ion line spectra, which was very likely induced by the electroject current. We will look into field-aligned, (Birkeland) current-induced, low-frequency plasma modes in our summer experiments [Rooker et al., 2012]. This problem will be further addressed in later sections for radar detection of ion lines.

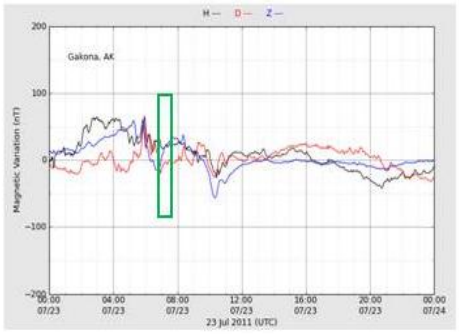

Figure 3. Magnetometer data recorded on July 23, 2011 from 7- 7:30 UT.

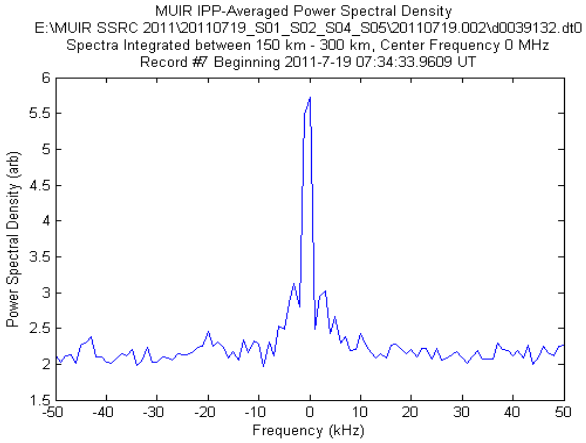

Figure 4. (Left) Ion lines record during beat wave experiments.

As mentioned earlier beat wave-generated VLF waves are intense enough to cause significant impacts on ionospheric plasmas. Estimated wave field intensities are 1 mV/m, which exceeds the thresholds required for the four-wave interaction process discussed in Labno et al. [2007]. We discuss this process and a new one, which will lead to direct acceleration of ionospheric electrons

4. Ionospheric Electron Acceleration via Four-Wave Interaction Processes

Illustrated in Figure 5 is the four-wave interaction process considered in Labno et al. [2007], which satisfies the following wave vector and wave frequency matching conditions.

$$\omega_o = \omega^{+}_{\ell h} - \omega_{s,} \quad \omega_o = \omega^{-}_{\ell h} + \omega^{*}_{s,} \quad \mathbf{k_o = k_+ - k_S,} \quad \mathbf{k_o = k_- + k_S}$$

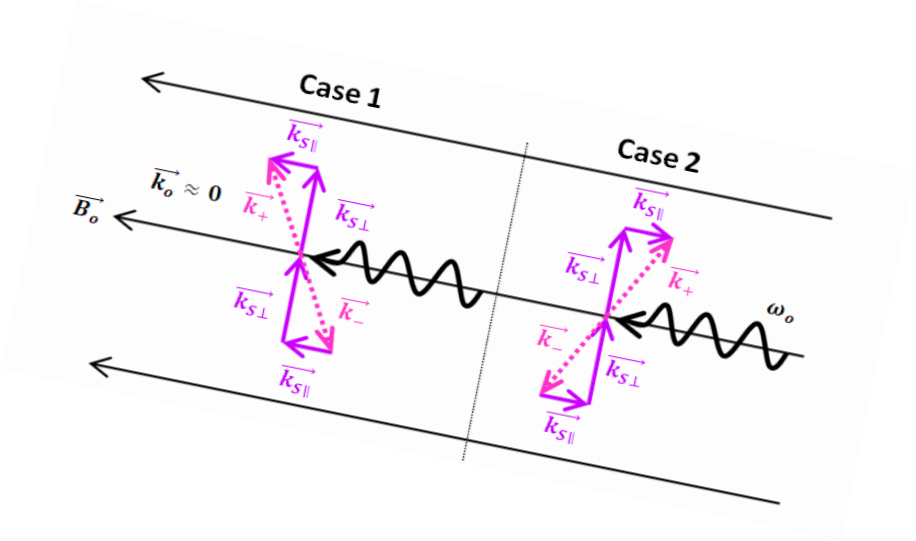

Figure 5. A four-wave interaction process showing that VLF whistler-mode wave (ω_o, $\mathbf{k_o}$) can parametrically excite Stokes ($\omega^-_{\ell h}$, $\mathbf{k}_-$) and anti-Stokes ($\omega^+_{\ell h,}$ $\mathbf{k}_+$) lower hybrid waves together with zero-frequency (ω_s, $\mathbf{k_S}$) field-aligned density irregularities. The excited lower hybrid waves have a single frequency equal to the VLF whistler wave frequency and a spectrum of wavelengths.

In Labno et al's work, the excitation of meter-scale lower hybrid waves explained the ionospheric electron acceleration of up to ten eV inferred from plasma line measurements. In this process $\mathbf{k_o} << \mathbf{k_S}$, thus k_+ (k_-) ≈ k_S. Hence, the excited lower hybrid waves are equally likely to propagate upwards or downwards along the background magnetic field, as illustrated in Figure 5. Indeed, these electrostatic waves can accelerate electrons in the ionosphere resulting in simultaneous upshifted and downshifted ion line enhancement, as seen in our experiments [see Figure 4]. However, we examine a four-wave interaction process that Labno et al. [2007] did not investigate and find a new electron acceleration process to be discussed in next section.

5. New Mechanism Leading to Direct Whistler Acceleration of Electrons

We consider the excitation of lower hybrid waves having whistler wave vector as their parallel wave vector and purely irregularity wave vector as their perpendicular wave vector [see the differences in the dotted lines in Figure 5 and in Figure 6(a) denoting excited Stokes and anti-Stokes lower hybrid waves]. Then, our theoretical analysis shows that electrons can be accelerated upward by beat wave-generated

whistler waves, which preferentially propagate upward [Rooker, report for Lutchen Fellowship, 2012; Rooker and Lee, 2012]. Our ion line data support this expectation that up-streaming electrons yield frequency-downshifted ion lines, as displayed in Figure 6(b).

[6(a)] [6(b)]

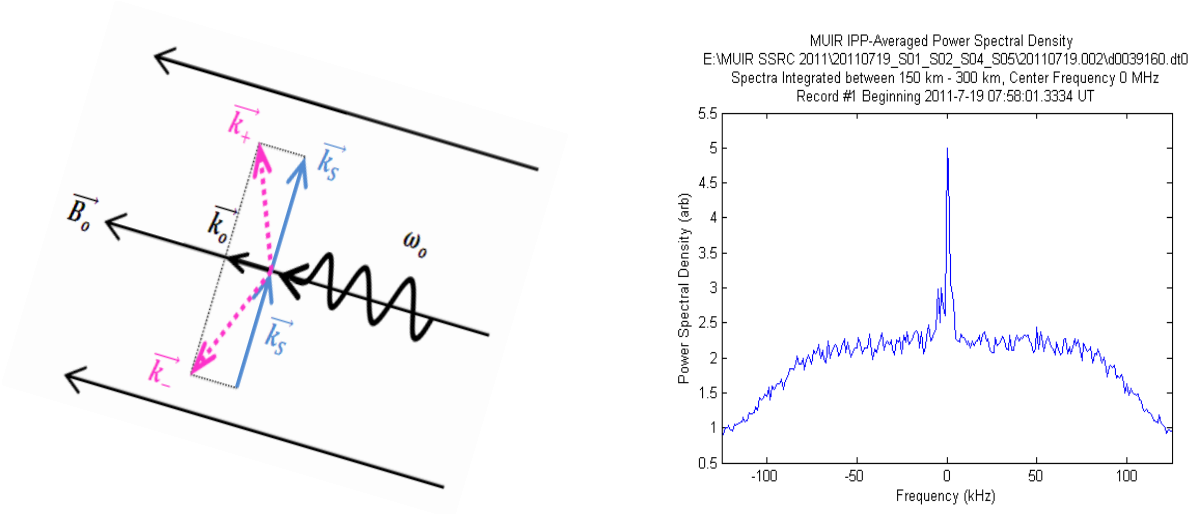

Figure 6. Illustration of upward electron acceleration by up-propagating whistler waves, and corresponding induced frequency-downshifted ion line enhancement due to Doppler effect.

6. Discussions and Conclusions

We have successfully demonstrated the beat wave generation of VLF whistler waves using two HF heater waves at Gakona, Alaska. This research is aimed at the controlled study of whistler wave interactions with (1) ionospheric plasmas and (2) energetic particles trapped in the radiation belts. Unlike the HF amplitude modulation process of generating whistler waves, the beat wave technique does not require the presence of a background electrojet. Therefore, whistler waves can be generated in regions at lower latitudes, such as Arecibo, Puerto Rico. Additionally, beat wave technique can generate electromagnetic waves in a broader range of frequencies (e.g., from a fraction of 1 Hz to kHz) than previous methods. However, in our reported experiments, we do not expect to see ionospheric plasma effects due to

energetic charged particles precipitated from outer radiation belts over Gakona. The reason is given below.

Consider the whistler wave-particle resonant interaction condition,

$$\omega_o + k_{\|} v_{\|} = \omega_{ce} [1 - (v_{\|}^2 + v\perp^2)/ c^2]^{½},$$

where ω_o and ($k_{\|}$) k_o denote, respectively, frequency and (parallel) wave number of the whistler-mode wave, and the dispersion relation: $(ck_o/\omega_o)^2 = 1- \omega_{pe}^2/[\omega_o (\omega_o -\omega_{ce})]$. Here, ω_{ce} and ω_{pe} represent the angular cyclotron and plasma frequencies of cold plasmaspheric electrons; $v_{\|}$ and $v\perp$ represent the velocity components of radiation belt electrons parallel and perpendicular to the magnetic field; c is the speed of light in a vacuum [Pradipta et al., 2007]. For simplicity, assuming that the whistler wave propagates along the geomagnetic field, we can determine $k_{\|}$ from the whistler wave dispersion relation. We found that whistler wave interactions with energetic electrons at high latitudes decrease drastically as frequency increases due to background plasma conditions in radiation belts. Therefore, whistler waves in the ELF range are expected to interact more effectively with the electrons trapped in the outer radiation belt than VLF whistler waves can.

We have analyzed a new four-wave interaction process wherein whistler waves can accelerate ionospheric electrons directly along the geomagnetic field during their upward propagation. This process results in frequency-downshifted ion lines, as we have indeed observed in Gakona experiments. Furthermore, we can base on this mechanism to understand the measured plasma lines at Arecibo, which have only frequency-downshifted spectra caused by NAU-launched 40.75 kHz whistler waves [Rooker, report for Lutchen Fellowship, 2012; Lee et al., 2012]. In our future Gakona experiments, we will examine effects of electrojet currents on beat wave-generated whistler waves, possibly excitation of low-frequency plasma modes, and changes in background plasma conditions. We should finally mention that we used uncoded long pulse radar technique to record ion lines in our experiments. But, in our planned experiments for this upcoming summer at Gakona, we will adopt the coded long pulse technique to measure plasma lines for further investigation of whistler wave-plasma and whistler wave-particle interactions [Rooker et al., 2012].

Acknowledgments. This work was supported by AFOSR grant FA9550-09-1-0391. A portion of this paper was presented by M.C. Lee as an invited paper at the 3rd International Conference on "Turbulent Mixing and Beyond", Abdus Salam International Centre for Theoretical Physics (ICTP), Trieste, Italy, 21 - 28 August 2010.

References

Labno, A., R. Pradipta, M. C. Lee, M. P. Sulzer, L. M. Burton, J. A. Cohen, S. P. Kuo, D. L. Rokusek, "Whistler-mode wave interactions with ionospheric plasmas over Arecibo", Journal of Geophysical Research, 112, A03306, doi:10.1029/2006JA012089, 2007.

Lee, M.C., "Generation and detection of whistler wave-induced space plasma turbulence", invited talk, 3rd International Conference on "Turbulent Mixing and Beyond", Abdus Salam International Centre for Theoretical Physics (ICTP), Trieste, Italy, 21 – 28 August 2010.

Lee, M.C., L.N. Whitehurst, L.A. Rooker, R. Pradipta, J.A. Cohen, M.J. Sulzer, B.J. Watkins, M.J. Starks, W.J. Burke, K.M. Groves, S.P. Kuo, "Investigation of Naturally Occurring and Radio Wave-induced Ionospheric Plasma Turbulence", 39th IEEE International Conference on Plasma Science, Edinburgh, Scotland, 8 - 12 July, 2012.

Pradipta, R., A. Labno, M. C. Lee, W. J. Burke, M. P. Sulzer, J. A. Cohen, L. M. Burton, S. P. Kuo, D. L. Rokusek, "Electron precipitation from the inner radiation belt above Arecibo", Geophysical Research Letters, 34, L08101, doi:10.1029/2007GL029807, 2007

Rooker, L.A. et al., Proposal for summer Gakona 2012 experiments, July 30 – August 9, 2012.

Rooker, L.A. and M.C. Lee (Advisor), Lutchen Fellowship Report, College of Engineering, Boston University, 2012.

Rooker, L.A. and M.C. Lee, "Beat Wave Generation Experiments for Study of VLF Whistler Wave Interactions with Ionospheric Plasmas and Radiation Belts", 39th IEEE International

Conference on Plasma Science, Edinburgh, Scotland, UK, 9-12 July, 2012.

Appendix H.

Simultaneous Observation of Wideband HF Attenuation and Enhanced VLF Generation

Spencer Kuo[1], M. C. Lee[2,3], and Arnold Snyder[4]

[1]Polytechnic Institute of New York University, 6 MetroTech Center, Brooklyn NY 11201

[2]Boston University, Boston, MA 02215

[3]Massachusetts Institute of Technology, Cambridge, MA 02139

[4]NorthWest Research Associates, P.O. Box 530, Stockton Springs, ME 04981

Abstract

Summer nighttime and daytime VLF wave generation comparison experiments were conducted on July 25 and July 27, 2011, respectively, using two CW HF X-mode waves with eleven VLF frequency differences from 2 to 21.5 kHz. The background magnetic variations were at comparable levels, but the D region absorption was significant and increasing in the daytime experiment when wideband disappearance of the ionogram echoes was also observed. VLF signals were detected from 2 to 7.6 kHz in both experiments, showing an inverse frequency dependence of intensity, although signal intensity (except at 5.5 kHz) detected at nighttime was stronger than the corresponding one detected in the daytime before the occurrence of wideband absorption. However, VLF signals from 11.5 to 21.5 (except at 19.6 kHz) were also

generated in the daytime experiment concurrent with the disappearance of the O-mode ionosonde echoes from 2 to 4 MHz. The concurrence of wideband disappearance of the ionogram echoes, the unexpected generation of VLF waves at higher frequencies, and the increasing D region absorption throughout the experiment may be explained by the generation of large scale density irregularities, which scatter the ionosonde signals as well as couple with the modulated electrojet to generate whistler waves. A theoretical formulation of the coupling mechanism for the whistler wave generation is presented.

1. Introduction

Ionospheric heating by powerful HF waves transmitted from the ground have been an active research area over the past four decades. Early experiments immediately led to the observations of many unexpected phenomena, such as wideband attenuation of the ionosonde signals and artificially induced spread-F that were then realized to be associated with the generation of density irregularities in the background plasma.

A major and relatively new facility for conducting ionospheric heating experiments is available in Gakona, Alaska, as part of the High Frequency Active Auroral Research Program (HAARP) [*Kossey et al*., 1999]. The HAARP HF transmitting system is a phased-array antenna of 180 elements. Each element is a crossed dipole, which radiates circularly polarized wave up to 20 kW in the frequency band from 2.8 MHz to 10 MHz. The antenna gain, which increases with the radiating frequency, varies from 15 dB to 30 dB. Thus an effective radiated power (ERP) of 90 dBW will be available in heating experiments. In the HAARP heating experiments, HF induced

artificial spread-F has been observed [e.g., *Kuo and Snyder*, 2010]. However, there was no report on the observation of HF induced wideband attenuation of the ionosonde signals.

Electrojet modulation as a mechanism for the ELF/VLF wave generation has been studied extensively in high latitude heating facilities. Normally, an amplitude modulated HF waveform is transmitted to modulate the electrojet [*Stubbe et al*., 1981, 1982; *Rietveld et al.*, 1989; *Kuo et al*., 2003]. Transmitting two CW HF waves with a small frequency difference can also modulate the electrojet in a similar way for VLF wave generation; moreover, this beat wave approach can also generate VLF waves in the absence of a background ionosphere current [*Kuo et al*., 2011].

Radiation intensity from the electrojet modulation mechanism is inversely dependent on the heater frequency. However, the beat wave generation occurs in the F region well above the electrojet. As shown later the beat wave generation mechanism depends more strongly on the heater frequency than the electrojet modulation mechanism.

In this work, both nighttime and daytime experiments using beat wave modulation of the electrojet for VLF wave generation were conducted. A relatively high heater frequency of 4.2 MHz was chosen to reduce the beat wave generation in the F region; thus the detected VLF radiation on the ground was generated mainly by the modulated electrojet. Surprisingly, HF induced wideband attenuation of the ionosonde signals manifested by nearly total disappearance of ionogram echoes in the heater-on ionograms was observed in the daytime experiment. Presented in Sec. 2 is a description of the experiments and the background conditions during the experiments. Results showing heating effect on the O-mode ionosonde echoes are presented and discussed in Sec. 3. The results of radiation generated from 2 kHz to

21.5 kHz and the frequency dependency of the radiation intensity are presented in Sec. 4. A whistler wave generation mechanism for the detected VLF radiation is presented in Sec. 5. This work is summarized in Sec. 6.

2. Background Conditions and Experiments

Experiments on VLF wave generation by the interference of two HF waves in the ionosphere were performed during both summer nighttime and daytime at Gakona, Alaska. The nighttime experiment (with Earth shadow heights of approximately 60 km) was performed on July 25, 2011 from UTC 09:40 to 10:20 (01:40 to 02:20, Alaska daylight time). Meridional midnight at Gakona, Alaska, in the last week of July of the year, nominally occurs at UTC 10:00. The daytime experiment was performed on July 27 from UTC 01:38 to 02:26 (17:38 to 18:26 of July 26, Alaska daylight time).

The background conditions on the two days monitored by the 30 MHz riometer are presented in Figs. 1a and 1b, in which a rectangular box in each plot marks the experimental period. The 30 MHz riometer absorption measurements inside the box are minimal (~ 0 dB) on July 25 and maximal (~ 0.5 dB) on July 27. These results suggest that a D layer was absent in the nighttime experiment (July 25) and present in the daytime experiment (July 27). It is noted that D region absorption on July 27, as shown in Fig. 1b, increases continuously until the end of the experiment.

The background magnetic field variation $\Delta\mathbf{B}$ was monitored by the fluxgate magnetometer located at Gakona. The Gakona magnetometer records for the two days are presented in Figs. 1c and 1d, in which again the rectangular boxes mark the experimental period for each day, as

well as with expanded plots in Figs. 1e and 1f. As shown, the Gakona geomagnetic field was relatively stable and had approximately 25 nT deviation from the background geomagnetic field during each of the two experiments. The magnetometer records suggest a low level "background ionospheric current" was present on both days during the experiment periods.

The reflection height of the 4.2 MHz X-mode wave can be referred to that of the 3.43 MHz O-mode wave. The Gakona ionosonde records show that in the two experiments, foF2 is larger than 3.43 MHz; indicating that the HF reflection height was below the F peak (foF2 layer).

The experiments were conducted with the X-mode HF heating waves directed along the geomagnetic zenith and run for 5 minute periods for 9 cycles. In each 5-minute period, there were 90 seconds between the beat frequency "long tones 1 and 2" with 60 seconds each. In this 90 second gap, there were beat frequency short tones (30 seconds) and beat frequency ramps (60 seconds). Following beat frequency long tone 2, the heater was off, i.e., the heater's RF output was disabled completely, for 15 seconds, followed by 30 seconds of AM short ramps and 30 seconds of ramps, and then 15 seconds off.

The beat frequency "long tones" applies a beat wave scheme for VLF generation at a single beat frequency for the 60 second period. The 12x15 array of the HAARP HF transmitter was split into two 6x15 sub-arrays, one sub-array transmitted at 4.2 MHz and the other at 4.2 MHz + f, where f was changed sequentially in the order of 1 kHz, 2 kHz, 3.5 kHz, 5.5 kHz, 7.6 kHz, 9.5 kHz, 11.5 kHz, 13.6 kHz, 15.5 kHz, 17.5 kHz, 19.6 kHz, and 21.5 kHz; and repeating the sequence to 9.5 kHz; both subarrays were operated at CW, full power (1.8 MW each). In each beat frequency short tones or AM short ramps, (sqrt-sine) amplitude modulated HF heater was transmitted at

full power (3.6 MW) by the full HF heater array. The frequencies of the amplitude modulation (AM) cover all of the 12 frequencies with 2.5 seconds for each frequency.

The VLF radiation was monitored by BAE Systems's VLF receiver, which didn't record when HAARP was transmitting ramps. The VLF receiver recorded North-South (N-S), East-West (E-W), and vertical components of the VLF wave magnetic field. The experiment was also monitored by the HAARP digisonde. The digisonde was run in a relatively fast mode that acquired one to four ionograms every minute starting on the minute during the heater on and off periods. The heater-off ionograms (those presented in Columns B and C of Fig. 4) are acquired with 50 kHz steps from 500 kHz to 5000 kHz. Each frequency step is 130 milliseconds and each ionogram takes 11.7 seconds to acquire. The heater-on ionograms presented in Column A/D of Fig. 4 are acquired with 50/25 kHz steps from 1500/500 kHz to 6000/6500 kHz. Each frequency step is 260/210 milliseconds and each ionogram takes 23.7/50.4 seconds to acquire.

3. Observation of Wideband Attenuation of O-mode Ionosonde Echoes

In the experiment on July 25, there is no absorption recorded by the 30 MHz riometer as shown in Fig. 1a. It is consistent with the appearance of second hop ionogram echoes in the digisonde ionograms which nevertheless, indicate that a thin E layer was still present in this nighttime experiment. Two sets of heater on-off ionograms are presented in Fig. 2. Some noticeable changes, manifesting the heating effect, include 1) echoes from the E layer disappear when the heater was on, and 2) the echoes below and near the HF reflection height (corresponding to the O-mode ionosonde frequency of 3.43 MHz) were fading as the experiment continued. The

results indicate that the heating effect was prominent locally in the two end frequency regions of the ionosphere covered by the HF heater.

The ionograms recorded during the July 27 experiment have more dramatic changes during the heater-on periods as noted below. First, the ionograms before and after the experiment are presented in Figs. 3a and 3b for references. The true height distribution of the ionogram echoes is also plotted in the ionogram. The 0130 UT ionogram was recorded right after the O-mode heater of 4.5 MHz (CW full power and directed at 1 min 9.9 off zenith and 188.8 azimuth) was turned off and the 0230 UT ionogram was recorded when the O-mode heater of 4.5 MHz (CW full power and directed at 3 min 16.6 off zenith and 223.9 azimuth) was turned on. Thus, the ionogram in Fig. 3a should be generally free of heater affects. On the other hand, the ionogram in Fig. 3b is affected by the heater. As shown, the number of echoes in Fig. 3b reduces considerably; in particular, the F2-layer ionogram echoes are suppressed. The electron density distributions are presented in Fig. 3c. As shown, an E layer was present and expanding downward into the upper D-layer throughout the experiment. There were no significant changes in the F region electron density distribution.

We next present a sequence of 23 ionograms in Fig. 4 for a comparison to reveal the heating effect. Ionograms presented in Columns A and D were recorded during the heater on periods and in Columns B and C were recorded during the heater off periods. The 11 heater-on ionograms were recorded after turning on the heater for 30 s, and the 12 heater-off ionograms were recorded right after turning off the heater. Heating leads to the decrease of the ionogram echo amplitude and only the strongest echoes are recorded. Thus the heating effect can be manifested by the disappearance of ionogram echoes in the heater-on and heater-off

ionograms. In fact, the heater-on ionograms recorded 15 minutes after the start of the experiment (i.e., at 01:51:31 and later) already show wideband disappearance of echoes.

The gain control of the receiver of the digisonde is affected by the heater only during the heater on period; hence, the off ionograms (and their associated echo amplitudes) are not impacted directly by the heater through the digisonde receiver. However, the off ionograms presented in Columns B and C of Fig. 4 were acquired beginning the moment the heater turns off, these ionograms could still be impacted by the heater through heater-induced ionospheric modification (such as density irregularities) which did not disappear immediately after the heater turned off. But the heating effect on the echoes might not be uniform throughout the acquiring period because each ionogram took 11.7 seconds to acquire. Nevertheless, the number of echoes in each off ionogram presented in Columns B and C of Fig. 4 is strongly impacted by the heating-induced ionospheric perturbations. As shown in Fig. 5 the echo number in each off ionogram is much less than the echo numbers 1021 and 402 of the two ionograms recorded before and after the experiment, presented in Figs. 3a and 3b. It is noted that the ionogram of Fig. 3b is affected by the O-mode heater, which produces much less heating effect in the lower ionosphere than that of the X-mode heater.

Comparing the on/off/off/on ionograms in each row, one can see that the two on inongrams and two off ionograms are quite similar to each other, but the on/off ionograms are quite different. It suggests that the heating effect on echoes decays in time faster than the frequency sweeping rate of the ionosonde.

Moving down along each column of Figure 4, one observes clearly a decrease in the number of ionogram echoes in both on and off ionograms. The ionogram echoes disappear almost completely in the on ionograms of the last three rows (i.e., from 01:56 to 02:06 UT). This represents wideband absorption on the HF signals. The number of the ionogram echoes in the off ionogram summarized in Fig. 5 shows a gradual decrease of the echoes over a 25-minute period. This trend also represents a form of wideband absorption observed at these lower HF frequencies. Because the heating effect on echoes of the off ionograms decays in time faster than the frequency sweeping rate of the digisonde, the impact of heating dominating on the lower frequency side of the ionogram is indicated in Fig. 4.

The observation suggests that the 15 second heater-off period between two heater-on periods was not long enough for the ionosphere to recover fully from the perturbation; hence the ionosphere becomes preconditioned to ease the excitation of subsequent heater-induced perturbations.

From 02:08:00 to 02:11:30, the transmission direction of the HF heating waves was changed from along the geomagnetic zenith to vertical, allowing the prior heated region of the ionosphere to recover fully; consequently, the number of echoes in the heater-off ionograms also recovered.

The record of the riometer indicates that the D region absorption starts increasing from the beginning of the experiment. Though it is difficult to verify if such an increase of absorption is attributed to the heaters or a combination of a naturally occurring absorption event and the heaters, it is, however, consistent with the increase of the heating effect with time as

demonstrated in heater on/off cycles. This wideband attenuation phenomenon persists throughout the remaining experiment period, though some echoes from the E layer were occasionally present.

Wideband attenuation of ionosonde signals is generally attributed to the presence of medium- to large- scale density irregularities (i.e., a few tens of meters to a few kilometrs) in the background ionosphere [*Fejer*, 1979]. These irregularities scatter the ionosonde signals out of the transmit beam to reduce or even eliminate backward scattering or reflection [*Cohen et al.*, 2010]. There are several mechanisms which can generate density irregularities by the HF heaters [*Kuo and Schmidt*, 1983; *Lee and Kuo*, 1983]. A likely one is the nonlinear thermal instability [*Kuo et al*., 1999a], which produces periodic density irregularities in the D and lower E regions of the ionosphere. Both elastic and inelastic electron-neutral collision frequencies are electron temperature dependent and modified by the HF heating. Such temperature dependence provides a feedback channel to the heating, leading to the excitation of a thermal instability and the subsequent nonlinear evolution of the produced density perturbation after exceeding a threshold. The spatial distribution of the periodic density irregularities is parallel to, rather than perpendicular to, the geomagnetic field [*Lee et al.*, 1998; *Cohen et al.*, 2010], which for Gakona, AK is 14^{o} off the zenith. The combination of the increasing D region absorption to weaken the ionosonde signals and the scattering of the ionosonde signals by the produced periodic density irregularities causes the disappearance of ionogram echoes over a wideband. Moreover, the heater-induced thermal pressure force at the beat frequency can drive a whistler mode current in the periodic density irregularities [*Kuo et al*., 1999b; *Kuo and Koretzky*, 2001].

4. Generation of VLF Waves

The nonlinear coupling for wave beating is inversely proportional to the square of the heating wave frequency. Moreover, the VLF signal intensity received on the ground is inversely proportional to the square of the distance from the source current, which is located generally near the HF reflection height. Thus the beat wave intensity depends strongly on the heater frequency.

The heater configurations used in the two experiments on July 25 and 27 were identical: 4.2 MHz, X-mode, full power, and along the magnetic zenith. Thus the VLF wave intensity was dependent only on the ionosphere conditions. The reflection height of the 4.2 MHz X-mode heater refers to the height of the 3.43 MHz O-mode ionosonde echo. The ionograms presented in Figs. 2 and 3 show that the virtual height (~ 350 km) of the O-mode ionosonde echo at 3.43 MHz in the July 25 experiment is much higher than that (~ 220 km) in the July 27 experiment. On the other hand, the record of the riometer shown in Fig. 1 suggests that the heater energy to be significantly absorbed in the D region in the July 27 experiment. In other words, the ionosphere conditions in both experiments do not favor the beat wave generation in the F region.

However, a background ionospheric current was present on both days during the experiment periods. It could be modulated by the two HF heaters at the beat frequency (frequency difference). The VLF radiation intensity will have inverse frequency dependence similar to that generated via the electrojet modulation by an amplitude modulated HF heater. A comparison

of the magnetic amplitudes of the VLF waves generated in July 25 and 27 experiments is presented in Fig. 6. As shown, the VLF wave amplitude is indeed inversely proportional to the frequency from 2 to 7.6 kHz on both days. The wave amplitude on July 27 is smaller than the corresponding one on July 25 (except for the one at 5.5 kHz) because of the D region absorption. The VLF waves at beat frequencies larger than 7.6 kHz were not generated on July 25. On the other hand, VLF waves at beat frequencies larger than 9.5 kHz were generated (except for the one at 19.6 kHz) on July 27. During this period, wideband disappearance of the O-mode ionosonde echoes also occurred. It was shown that thermal instability [*Kuo et al*., 1999a] excited by the HF heaters in the D and lower E region could evolve nonlinearly to form periodic density irregularities having a broad spatial spectrum to scatter O-mode ionosonde signals over a wideband. These density irregularities could also couple to the temporally modulated electrojet (background current) to produce a whistler mode current and the associated whistler (VLF) wave at the beat frequency [*Kuo et al*., 1999b; *Kuo and Koretzky*, 2001]. A similar process for VLF wave generation by an intensity modulated HF heater was analyzed and revealed experimentally by *Kuo et al.* [2008]. In the second cycle of the experiments, the experiment time was enough only for repeating four beat frequencies at 1, 2, 3.5 and 5.5 kHz, i.e., the experiment was stopped after generating 5.5kHz signal. The result of the July 27 experiment shows that the VLF wave generated in the second cycle has a similar frequency dependency as that generated in the first cycle, but has slightly smaller amplitude. However, the wave intensities in the second cycle of the July 25 experiment drop considerably. The drop of the generated VLF wave intensity may be caused by the background change due to the HF heating and/or the natural decay of the ionosphere near meridional midnight.

5. Whistler Wave Generation Mechanism

Ohmic heating by two HF waves of slightly different frequencies modulates the electrojet current in time. The elevated electron temperature evolves nonlinearly into kilometer-scale periodic distribution along the geomagnetic field, which modifies the electron-ion recombination rate to form density irregularities. The density irregularities convert the temporal modulated electrojet current into space-time dependent current. As the frequency and wave number of the induced current wave satisfies the dispersion relation of the whistler wave, this current is a whistler mode current that generates whistler wave directly.

5.1. Electrojet

The polar electrojet current is driven by a dc electric field $\mathbf{E}_0 = \hat{x} E_0$ in collisional plasma which is embedded in a background magnetic field $\mathbf{B}_o = -\hat{z} B_0$. Electrons in the electrojet have a fluid velocity

$$\mathbf{u}_e = -(eE_0/m)(\hat{x}\,\nu_{en} - \hat{y}\,\Omega_e)/(\nu_{en}^2 + \Omega_e^2) \qquad (1)$$

where Ω_e is the electron gyrofrequency. Then the electron electrojet current density is obtained to be

$$\mathbf{J}_e = -en_0\mathbf{u}_e = (n_0e^2E_0/m)(\hat{x}\,\nu_{en} - \hat{y}\,\Omega_e)/(\nu_{en}^2 + \Omega_e^2) = \underline{\sigma} \cdot \mathbf{E}_0 \qquad (2)$$

where the conductivity tensor $\underline{\sigma} = \sigma [\hat{x}\hat{x} + \hat{y}\hat{y} + (\Omega_e/\nu_{en})(\hat{x}\hat{y} - \hat{y}\hat{x})]$ and the conductivity $\sigma = n_0 e^2 \nu_{en} / m(\nu_{en}^2 + \Omega_e^2)$ is electron temperature dependent through the dependency $\nu_{en} \propto T_e^{5/6}$ [*Gurevich*, 1978].

5.2. HF heating and modulation

When the HF heater array is split into two sub-arrays, transmitting CW X-mode HF waves at two slightly different frequencies f_{01} and f_{02}, where $f_{01} = f_0$, $f_{02} = f_0 + f$, and f is the beat-wave frequency in the VLF range, the total heater wave field $\mathbf{E}_p$ becomes

$$\mathbf{E}_p = \mathbf{E}_{p1} + \mathbf{E}_{p2} = (\hat{x} - i\hat{y})(E_{p0}/2)[1 + e^{-i(\omega t - \psi)}]\exp[i(k_0 z - \omega_0 t)] + \text{c.c.} \quad (3)$$

where E_{p0} is the field amplitude of each heater beam. ψ is the phase difference of two HF waves transmitted by the two sub-arrays. ω_0 and k_0 are the heater radian frequency and wavenumber. The electrons respond at the velocity

$$\mathbf{v}_{pe} = -i\,(\hat{x} - i\hat{y})\,[(eE_{p0}/2m_e)/(\omega_0 - \Omega_e)][1 + e^{-i(\omega t - \psi)}]\exp[i(k_0 z - \omega_0 t)] + \text{c.c.} \quad (4)$$

In the presence of HF heating, the electron thermal energy equation [*Braginskii*, 1965; *Gurevich*, 1978] is given by

$$\partial T_e/\partial t + (2T_e/3)\nabla\cdot\mathbf{v}_e + \delta(T_e)\nu_e(T_e)(T_e - T_n) + \text{ionization loss}$$

$$= (2/3n_0)(Q + \nabla\cdot \underline{\kappa}_e\cdot\nabla T_e) + \text{solar heat input} \quad (5)$$

where n_0 is the plasma density, $\mathbf{v}_e$ is the electron fluid velocity, $\delta(T_e)$ is the average relative energy fraction lost in each collision, $\nu_e(T_e)$ is the effective collision frequency of electrons with neutral particles (it accounts for both elastic and inelastic collisions), T_n is the temperature of

the background neutral particles; the ionization loss becomes significant as electrons are heated up to high temperature; $Q \cong \nu_{en} n_0 m[u_e^2 + \langle |v_{pe}|^2 \rangle]$ is the total Ohmic heating power density in the background plasma and contributed by the electrojet current and by the HF heater waves, $\mathbf{K}_e$ is the thermal conduction tensor, and m is the electron mass; the ionization loss term on the left hand side (LHS) of (4) will be neglected.

In VLF range, $\delta(T_e)\nu_e(T_e) << \omega$, the induced electron temperature perturbation at the modulation frequency ω is determined from (5) to be

$$\delta T_e = (4/3)m(\nu_{en0}/\omega_1)\, v_q^2 \sin(\omega t - \psi) \qquad (6)$$

where $v_q^2 = (eE_{p0}/m)^2/[(\omega_0 - \Omega_e)^2 + \nu_{en0}^2]$ and $\nu_{en0} = \nu_{en}(T_{e0})$. With the aid of (6), expanding $\nu_{en} = \nu_{en0}(T_e/T_{e0})^{5/6}$ in (1) yields the modulated electron fluid velocity

$$\delta \mathbf{u}_e = -(A/e)[\hat{\mathbf{x}} + \hat{\mathbf{y}}\, 2\nu_{en0}/\Omega_e] \sin(\omega t - \psi)\, \mathrm{Rect}[(z-z_0)/\Delta z]. \qquad (7)$$

and an oscillation current

$$\Delta \mathbf{J}_e = n_0 A[\hat{\mathbf{x}} + \hat{\mathbf{y}}\, 2\nu_{en0}/\Omega_e]\sin(\omega t - \psi)\mathrm{Rect}[(z-z_0)/\Delta z] = \Delta \mathbf{J}_{e\omega} e^{-i\omega t}\, \mathrm{Rect}[(z-z_0)/\Delta z] + \text{c.c.} \quad (8)$$

Here, $A = (10e^2E_0/9m)(\nu_{en0}^2/\omega\Omega_e^2)(v_q^2/v_{te}^2)$ and $v_{te} = (T_{e0}/m)^{1/2}$ is the electron thermal speed; we assume that the electrojet extends in altitude from z_1 to z_2; $z_0 = (z_1 + z_2)/2$ and $\Delta z = z_2 - z_1$; the unit rectangular function $\mathrm{Rect}(x) = 1$ for $|x| \le ½$ and 0 otherwise; $\Delta \mathbf{J}_{e\omega} = i\, e^{i\psi}(n_0 A/2)[\hat{\mathbf{x}} + \hat{\mathbf{y}}\, 2\nu_{en0}/\Omega_e]$. This oscillation current is equivalent to a dipole radiator, the magnetic flux density of the radiation is given by

$$\Delta \mathbf{B}_\omega = i\, V (\mu_0/4\pi r)(\mathbf{k} \times \Delta \mathbf{J}_{e\omega}) \exp(ikr) + \text{c.c.} \qquad (9)$$

where $V = \Delta z\, \Delta A$ is the volume of the modulated electrojet.

5.3. Density irregularities

As the electron temperature perturbation grows, the background plasma density also varies accordingly, through the dependence of the electron-ion (NO^+ and O_2^+) recombination rates on the electron temperature, with the relation [*Gurevich*, 1978]

$$n(T_e) / n(T_{e0}) \cong (0.6\, \chi^{0.7} + 0.4\, \chi^{1.2})^{1/2} \qquad (10)$$

where $\chi = T_e/T_{e0}$; the 3 to 2 ratio of the daytime densities of O_2^+ and NO^+ is assumed. Therefore, the spatial spectrum of the density irregularities is determined directly by the steady state electron temperature perturbation.

Eq. (5) is solved for the steady state situation by setting the time derivative term on its LHS equal to zero. Again, the second term on the LHS of (5) is derived, from the continuity equation ($\nabla \cdot n_e \mathbf{v_e} = 0$) and momentum equation ($-\nabla p_e - m n_e \nu_{en} \mathbf{v_e} \cong 0$) of electrons and the ratio of specific heats for electrons $\gamma_e = 3$, to be $(2T_e/3)\nabla \cdot \mathbf{v_e} = -(2m\nu_{en})^{-1}(dT_e/dz)^2$. This term and the thermal diffusion term on the RHS of (5) can be combined into a single diffusion term, leading to

$$\begin{aligned}(0.6\, \chi^{0.7} + 0.4\, \chi^{1.2})^{-1/2} \chi^{-1/4}\, d_\eta\, (0.6\, \chi^{0.7} + 0.4\, \chi^{1.2})^{1/2}\, \chi^{5/12}\, d_\eta\, \chi \\ = -a\, \chi^{5/6} - 30.26(1 - t_n) + \{\chi^{5/6} + 8.38\, \chi^{-1/2} \\ + \chi^{-5/2}[14.73\, e^{6.98(1-1/\chi)} + 0.1\, e^{13.88(1-1/\chi)}]\}(\chi - t_n) \qquad (11)\end{aligned}$$

where $\eta = (m/1.05M_n)^{1/2}(\nu_{e0}/v_{te})z$, $d_\eta = d/d\eta$, $a = (M_n/3m)[(u_e^2 + \langle|v_{pe}|^2\rangle)_0/v_{te}^2] \cong (2M_n/3m)[eE_{p0}/m(\omega_0 - \Omega_e)v_{te}]^2$ and $t_n = T_n/T_{e0} = 0.2$ is assumed. The last term on the RHS of (11) corresponds to the collision damping term in (5), which consists of three terms contributed by elastic collision and inelastic collisions of rotational and vibrational excitations, respectively. The periodic solutions of (11) [*Kuo and Koretzky*, 2001] lead to density irregularities, $\Delta n(z) = \int n(k)\, e^{ikz}\, dk/2\pi$ + c.c., as manifested by (10).

5.4. Whistler wave generation

The mixing of the velocity perturbation (7) with the electron density perturbation $\Delta n(z) = \int n(k)\, e^{ikz}\, dk/2\pi$ + c.c. of the irregularities produces a space-time dependent current density distribution in the electrojet as

$$\mathbf{J}_{eW} = \mathrm{Rect}[(z-z_0)/\Delta z][\hat{\mathbf{x}} + \hat{\mathbf{y}}\, 2\nu_{en0}/\Omega_e]A \sin(\omega t - \psi) \int n(k) \exp(ikz)\, dk/2\pi + \text{c.c.} \quad (12)$$

This source current drives VLF plasma waves propagating downward and upward along the geomagnetic field. If the wave number k of the spectral peak of Δn and the modulation frequency ω satisfy the dispersion relation of the whistler wave, $\mathbf{J}_{eW}$ becomes a mode current generating whistler waves directly.

Combining the electron momentum equation and Maxwell's equations leads to

$$[(\partial_t + \Omega_e\hat{\mathbf{z}}\times + \nu_{en0})(c^2\nabla^2 - \partial_t^2) - \omega_{pe}^2\partial_t^2]\mathbf{E}_W = c^2\mu_0(\partial_t + \Omega_e\hat{\mathbf{z}}\times + \nu_{en0})\partial_t\mathbf{J}_{eW} \quad (13)$$

where "×"represents the operation of cross product.

Substituting $\mathbf{E}_W = \int\{\mathbf{E}_+(k)\exp[i(kz + \omega t)] - \mathbf{E}_-(k)\exp[i(kz - \omega t)]\}dk/2\pi$ + c.c. into (13), with the aid of (12) and the dispersion relation $\omega = k^2c^2\Omega_e/\omega_{pe}^2$ of the whistler mode, obtains

$$E_{\pm x}(k) + i\,\delta_\pm E_{\pm y}(k)$$

$$= -\delta_\pm(\omega\mu_0 A\Delta z/2k^2)\int n(k')\exp[i(k - k')z_0]\mathrm{sinc}[(k - k')\Delta z/2]\,dk'/2\pi \qquad (14)$$

$$E_{\pm y}(k) - i\,\delta_\pm E_{\pm x}(k) \cong 0 \qquad (15)$$

where the subscripts "±" stand for down- and up-propagating waves; $\delta_\pm = \pm 1$; $\omega^2 << k^2c^2 << \omega_{pe}^2$ and $\nu_{en0}/\Omega_e << 1$ are assumed. The generated wave has circular polarization as expected. The periodic density irregularities generated/enhanced by the HF heater have a broad spectrum [*Kuo et al*., 1999a]; however, the dispersion relation of the whistler mode $\omega_1 = k_1^2c^2\Omega_e/\omega_{pe}^2$ imposes a condition to select a line at k_1 in the coupling. Thus $n(k) \cong \Delta n 2\pi\delta(k-k_1)$ is assumed and the down-propagating whistler wave fields generated by a mode current are obtained to be $\mathbf{E}_W = (\hat{x} - i\hat{y})E(k)\exp[-i(kz + \omega t)]$ + c.c. and $\mathbf{B}_W = -[(\omega_{pe}^2/\Omega_e\omega)^{1/2}/c]\,\hat{z} \times \mathbf{E}_W$; where $E(k) = E_+(k)\Delta k \approx i(kc^2\mu_0\Omega_e/2\omega_{pe}^2)\,A\,\Delta z\,\Delta n$.

The wavelength of the whistler wave is governed by the relation $\lambda = (c/f_{pe})(f_{ce}/f)^{1/2}$; let f = 10 kHz, f_{ce} = 1.4 MHz, and f_{pe} ~ 2 MHz (i.e., $n_e \sim 5 \times 10^4$ cm^{-3} indicated in Fig. 3), we have λ ~ 1.8 km. Therefore, the required scale lengths of the periodic density irregularities for converting the modulating current into whistler mode current are in the range of a few km, which overlaps with the scale length range of the irregularities effectively causing attenuation of the ionosonde signals.

6. Summary and Discussion

A comparison of a nighttime (July 25) and a daytime (July 27) experiment on VLF wave generation through electrojet modulation by HF heaters is presented. The electrojet was modulated by two CW HF heaters of slightly different frequencies, rather than by a single AM HF heater. In both experiments, the background magnetic variations were at comparable levels. However, the D region absorption was significant in the daytime experiment. As a result, the VLF signals at 2, 3.5 and 7.6 kHz detected in the nighttime experiment were stronger than the corresponding ones detected in the daytime experiment. The frequency dependence of the signal intensity has a similar characteristic, i.e., inversely proportional to the signal frequency, to that generated by using a single AM heater to modulate the electrojet. At this moment we should point out that six experiments were conducted from July 20 to July 27, 2011. But, among them only one daytime experiment was performed on July 27. In this experimental period, the D region absorption was present, and wideband absorption of ionosonde echoes appeared only in heater on periods. It indicates that the occurrence of wideband absorption requires a threshold, which can be exceeded by the combined effect of D region absorption and heater wave-induced ionospheric irregularities.

Signals at higher frequencies, i.e., from 9.5 to 21.5 kHz, were not detected in the nighttime experiment. Therefore, one would not expect to detect signals at those frequencies in the daytime experiment. On the contrary, quality signals at frequencies from 11.5 to 21.5 kHz, except the one at 19.6 kHz which was overshadowed by the high noise level, were detected in the daytime experiment. Concurrently, wideband disappearance of the O-mode ionosonde

echoes was observed in heater on periods. This is the first report on such an observation in HAARP heating experiments. Moreover, the record of the riometer shows a continuous increase of the D-region absorption in the experiment period. These correlations lead to the conclusion that a nonlinear thermal instability [*Kuo et al*., 1999a] was excited in the July 27 daytime experiment. As shown in Sec. 5, the thermal instability produces periodic density irregularities distributed parallel to the geomagnetic field. These irregularities scatter the weakened ionosonde signals (due to significant D region absorption) out of the transmit beam to reduce or even eliminate echoes, but also convert the modulated electrojet into whistler modes and accounts for the generation of VLF waves in the unexpected frequency range, consistent with previous experimental results [*Kuo et al.*, 2008].

Each VLF signal in Fig. 6 was generated for one minute duration, which is long enough to average out the background noise. In the future experiment, if the VLF is chosen in the range with very low background noise and an average is not necessary, then a plot of frequency-time spectra of VLF waves may be feasible to show the stability and quality of the wave generation.

ACKNOWLEDGMENTS

We are grateful to Paul Kossey, AFRL, for suggestions on the experiments and to John Labenski, BAE Systems-Technology Solutions, for recording VLF radiation. This work was supported by the High Frequency Active Auroral Research Program (HAARP), AFRL and by the Office of Naval Research, Grant No. ONR-N00014-10-1-0856, and ONR grants N00014-07-1-0999 as well as by AFOSR grant FA9550-09-1-0391. Part of the financial support was arranged through NorthWest Research Associates, Inc. under Air Force Research Laboratory contract FA8718-08-C-0049.

REFERENCES

Braginskii, S. I. (1965), *Transport Processes in a Plasma*, in Reviews of Plasma Physics, Vol. 1, edited by M. A. Loentovid, Consultant's Bur., New York.

Cohen, J.A., R. Pradipta, L.M. Burton, A Labno, M.C. Lee, B.J. Watkins, C. Fallen, S.P. Kuo, W.J. Burke, D. Mabius, and B.Z. See (2010), Generation of ionospheric ducts by the HAARP HF heater, *Phys. Scr.*, *T142*, (7pp) doi:10.1088/0031-8949/2010/T142/014040.

Fejer, J. A. (1979), Ionospheric modification and parametric instabilities, *Rev. Geophys.*, *17*, 135.

Gurevich, V. A. (1978), *Nonlinear Phenomena in the Ionosphere*, Chap. 2, Springer-Verlag, New York.

Kossey, P., J. Heckscher, H. Carlson, and E. Kennedy (1999), HAARP: High Frequency Active Auroral Research Program, *J. Arct. Res. U. S.*, *1*, 1.

Kuo, S. P. and G. Schmidt (1983), Filamentation instability in magneto plasmas, *Phys. Fluids*, *26*, 2529.

Kuo, S. P., S. H. Lee, D. Bivolaru, P. Kossey, M. C. Lee, R. J. Riddolls, and D. Sentman (2003), Experimental and numerical studies on ELF/VLF wave generation by amplitude-modulated HF heating waves, *Phys. Scr.*, *67*, 448.

Kuo, S. P., E. Koretzky, and M. C. Lee, (1999a), Plasma density enhancement and generation of spatially periodic irregularities in the ionospheric E-region by powerful HF waves, *Geophys. Res. Lett., 26(7)*, 991-994.

Kuo, S. P., E. Koretzky, and M. C. Lee, (1999b), A new mechanism of whistler wave generation by amplitude-modulated HF waves in the polar electrojet, *Geophys. Res. Lett., 26(12)*, 1677-1680.

Kuo, S. P. and E. Koretzky, (2001), Generation of density irregularities and whistler waves by powerful radio waves in the polar ionosphere, *Phys. Plasmas*, *8(1)*, 277-284.

Kuo, S. P., Yen-Liang Wu, R. Pradipta, J. A. Cohen, and M. C. Lee (2008), VLF wave generation by amplitude-modulated HF heater waves at Gakona, Alaska, *Geophys. Res. Lett.*, *35*, L13101 (1-5), doi:10.1029/2008GL034414.

Kuo, S. P. and Arnold Snyder, (2010), Observation of artificial Spread-F and large region ionization enhancement in an HF heating experiment at HAARP, *Geophys. Res. Lett.*, *37*, L07101, doi:10.1029/2010GL042656.

Kuo, S. P., Arnold Snyder, Paul Kossey, Chia-Lie Chang, and John Labenski, (2011), VLF wave generation by beating of two HF waves in the ionosphere, *Geophys. Res. Lett.*, *38*, L10608, doi:10.1029/2011GL047514.

Lee, M. C. and S. P. Kuo, (1983), Excitation of upper hybrid waves by a thermal parametric instability, *J. Plasma Physics*, *30(3)*, 463-478.

Lee, M. C., R.J. Riddolls, W.J. Burke, M.P. Sulzer, S.P. Kuo and E.M.C. Klien (1998),

Generation of large sheet-like ionospheric plasma irregularities at Arecibo *Geophys. Res.Lett., 25*, 3067.

Rietveld, M., P. Stubbe, and H. Kopak (1989), On the frequency dependence of ELF/VLF waves produced by RF ionospheric heating, *Radio Sci*., *24*, 270.

Stubbe, P., H. Kopka, and R. L. Dowen (1981), Generation of ELF and VLF waves by polar electrojet modulation: experimental results, *J*. *Geophys*. *Res*., *86*, 9073.

Stubbe, P., H. Kopka, M. T. Rietveld, and R. L. Dowen (1982), ELF and VLF wave generation by modulated HF heating of the current carrying lower ionosphere, *J*. *Atoms*. *Terr*. *Phys*., *44*, 1173.

FIGURE CAPTIONS

Fig. 1 Records of riometer and magnetometer on (a) and (c) July 25 and (b) and (d) July 27, 2011; rectangular boxes mark the experiment periods. Geomagnetic variations during the experiment periods on (e) July 25 and (f) July 27.

Fig. 2 O-mode ionosonde echoes recorded during heater off/on/on/off periods in the July 25 nighttime experiment.

Fig. 3 The background electron density distribution before and after the daytime experiment on July 27.

Fig. 4 Disappearance of the ionogram echoes over a wideband while the heating experiment was progressing; suggesting development of heater induced density irregularities; the heater on/off schedule is shown on the left hand side.

Fig. 5 Numbers of the ionogram echoes in the off ionograms presented in Columns B and C of Fig. 4.

Fig. 6 A Comparison of magnetic amplitudes of VLF waves generated on 7-25 and 7-27; the period is indicated in the 7-27 experiment when the disappearance of wideband ionogram echoes coincides with the generation of VLF waves

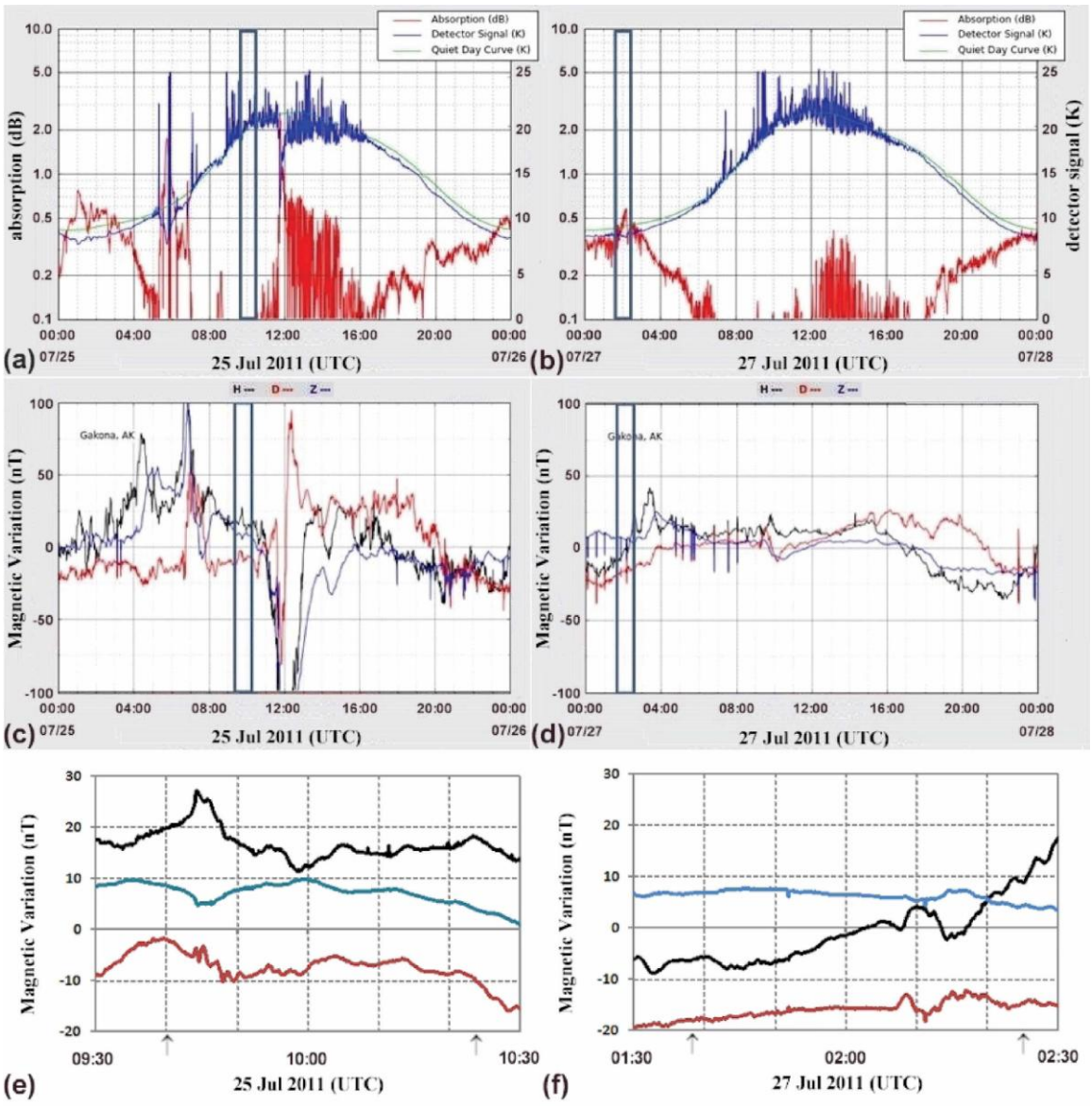

Fig. 1 Records of riometer and magnetometer on (a) and (c) July 25 and (b) and (d) July 27, 2011; rectangular boxes mark the experiment periods. Geomagnetic variations during the experiment periods on (e) July 25 and (f) July 27.

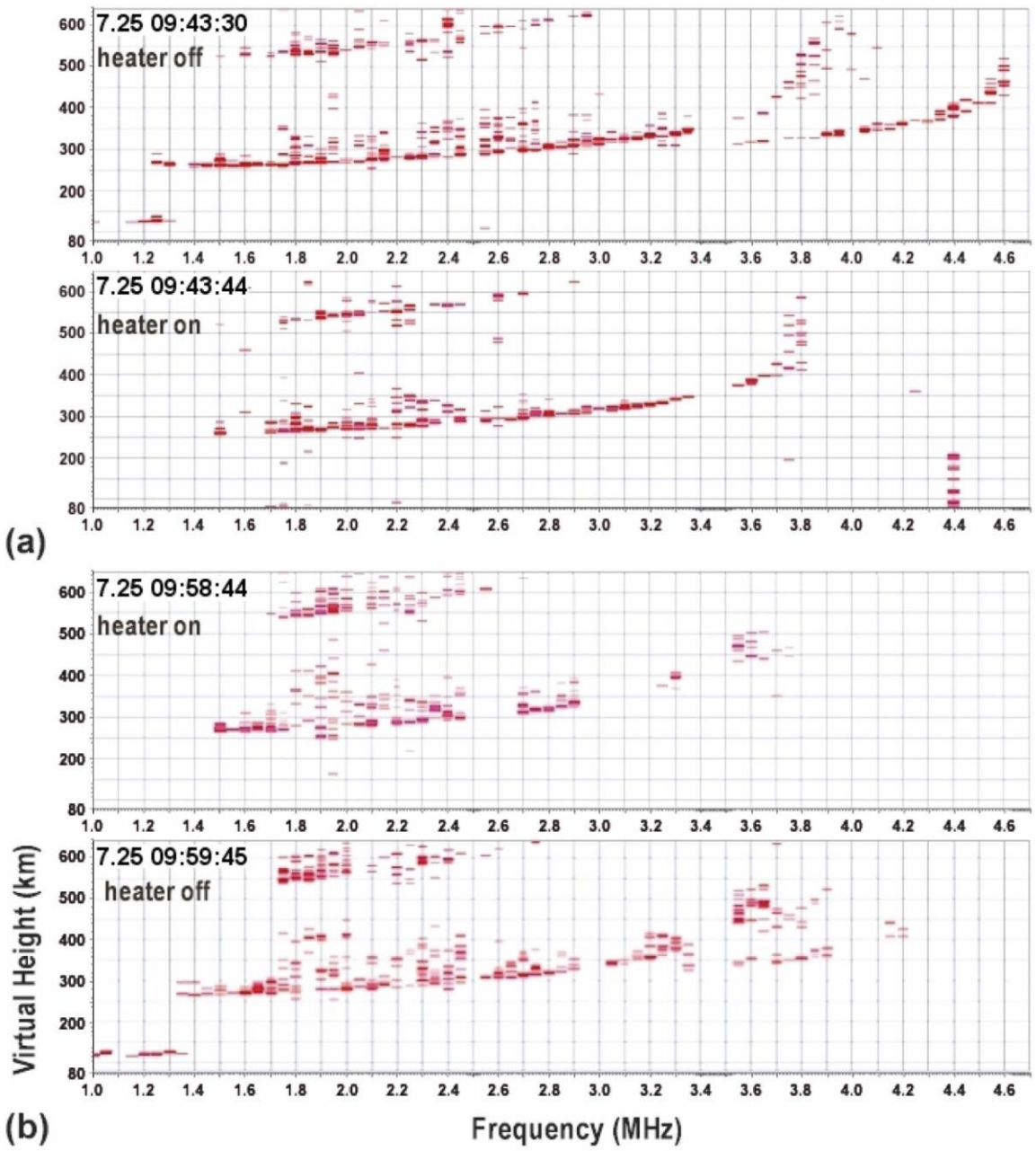

Fig. 2 O-mode ionosonde echoes recorded during heater off/on/on/off periods in the July 25 nighttime experiment.

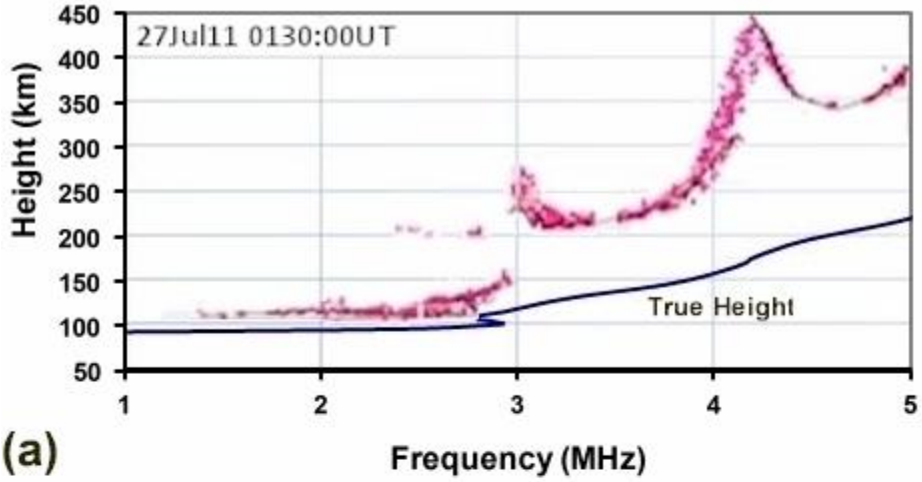

(a)

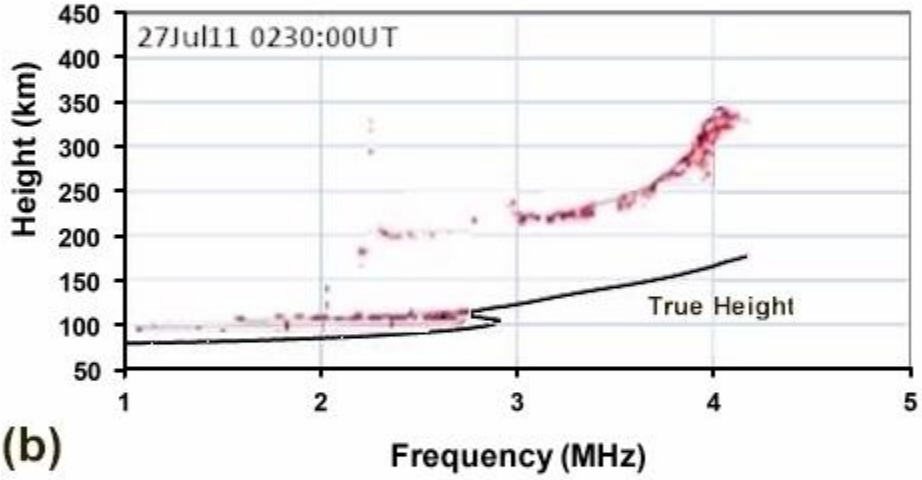

(b)

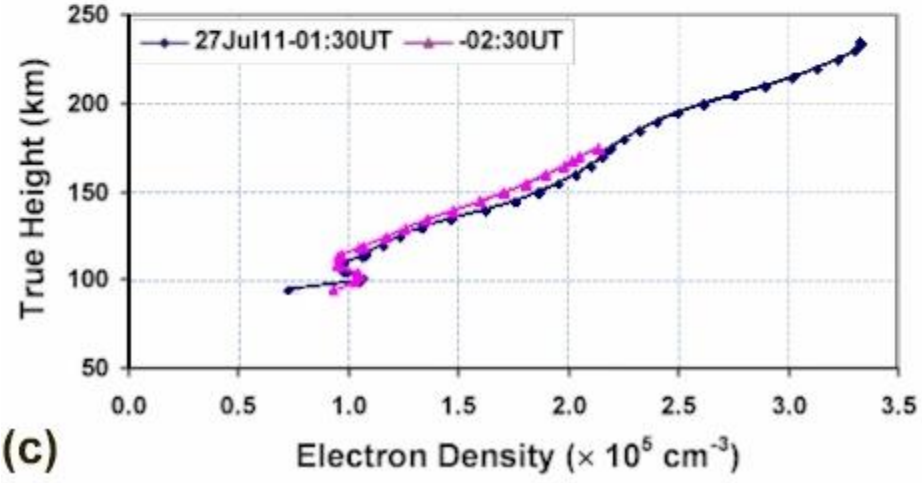

(c)

Fig. 3 (a) and (b) The ionograms and (c) the background electron density distributions before and after the daytime experiment on July 27.

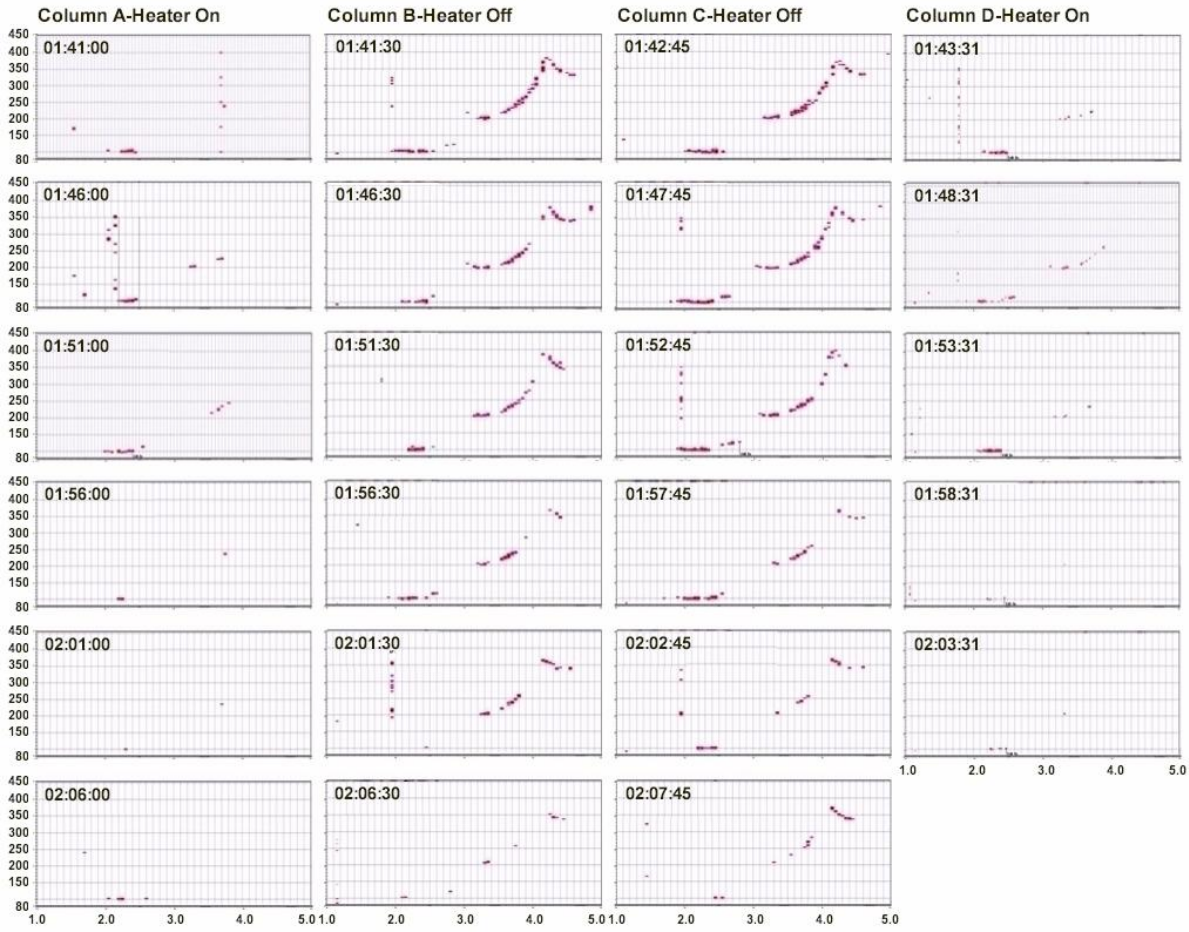

Fig. 4 Disappearance of the ionogram echoes over a wideband while the heating experiment was progressing; suggesting development of heater induced density irregularities; Columns A and D show heater-on ionograms and Columns B and C show heater-off ionograms.

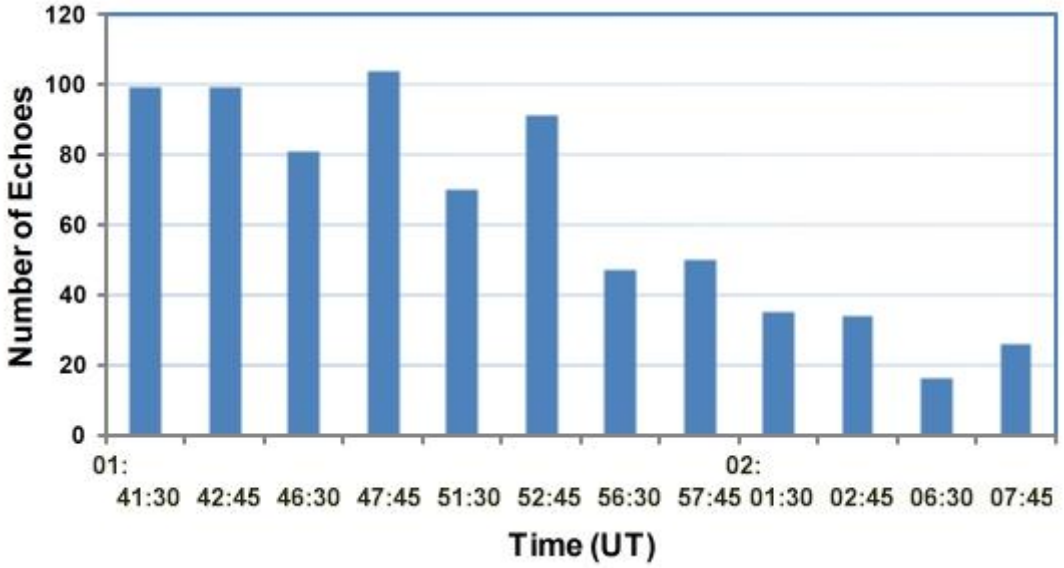

Fig. 5 Numbers of the ionogram echoes in the off ionograms presented in Columns B and C of Fig. 4.

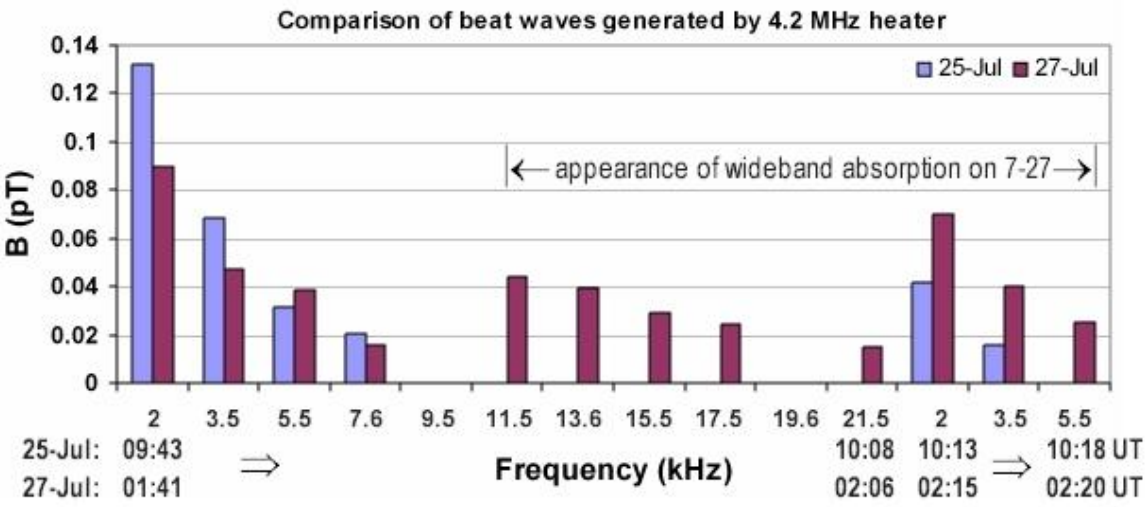

Fig. 6 A Comparison of magnetic amplitudes of VLF waves generated on 7-25 and 7-27; the period is indicated in the 7-27 experiment when the disappearance of wideband ionogram echoes coincides with the generation of VLF waves.

Appendix I.

Whistler Wave-induced Ionospheric Plasma Turbulence: Source Mechanisms and Remote Sensing

R. Pradipta[1], L.A. Rooker[2], L.N. Whitehurst[2], M.C. Lee[1,2], M.P. Sulzer[3], S. Gonzalez[3], C. Tepley[3], N. Aponte[3], B.Z. See[2], K.P. Hu[2], L.M. Ross[2]

1. Massachusetts Institute of Technology, Cambridge, MA 02137, USA

2. Boston University, Boston, MA 02215, USA

3. Arecibo Observatory, Arecibo, PR 00612, USA

Abstract

We report a series of experiments conducted at Arecibo Observatory in the past, aimed at the investigation of 40.75 kHz whistler wave interactions with ionospheric plasmas and the inner radiation belts at L = 1.35. The whistler waves are launched from a Naval transmitter (code-named NAU) operating in Aguadilla, Puerto Rico at the frequency and power of 40.75 kHz and 100 kilowatt, respectively. Arecibo radar, CADI, and optical instruments were used to monitor the background ionospheric conditions and detect the induced ionospheric plasma effects. Four-wave interaction processes produced by whistler waves in the ionosphere can excite lower hybrid waves, which can accelerate ionospheric electrons. Furthermore, whistler waves propagating into the magnetosphere can trigger precipitation of energetic electrons from the radiation belts.

Radar and optical measurements can distinguish wave-wave and wave-particle interaction processes occurring at different altitudes. Electron acceleration by different mechanisms can be verified from the radar measurements of plasma lines. To facilitate the coupling of NAU-launched 40.75 kHz whistler waves into the ionosphere, we can rely on naturally occurring spread F irregularities to serve as ionospheric ducts. We can also use HF wave-created ducts/artificial waveguides, as demonstrated in our earlier Arecibo experiments and recent Gakona experiments at HAARP. The newly constructed Arecibo HF heater will be employed in our future experiments, which can extend the study of whistler wave interactions with the ionosphere and the magnetosphere/radiation belts as well as the whistler wave conjugate propagation between Arecibo and Puerto Madryn, Argentina.

1. Introduction

We have been conducting a series of experiments at Arecibo Observatory, using the Naval VLF transmitter located at Aguadilla, Puerto Rico, aimed at studying whistler wave propagation and interactions with space plasmas. This Naval transmitter, code named NAU, emits VLF waves at a power and frequency of 100 kW and 28.5 kHz (earlier)/40.75 kHz (current), respectively, providing the source of whistler-mode signals. These experiments are based on the theoretical study of Lee and Kuo [1984a & 1984b] that whistler waves can interact with ionospheric and magnetospheric plasmas. Our experiments were also motivated by the so-called "explosive spread F" phenomenon first reported by Woodman and LaHoz [1976] in experiments carried out at Jicamarca Radio Observatory. This phenomenon has been associated with the occurrence of lightning [Woodman and La Hoz, 1976; Woodman and Kudeki, 1984]. A characteristic feature of this phenomenon is a train of short-lived, backscatter radar echoes with a period of ~6 sec,

which occurred at two altitudes in F region. A theory was subsequently presented by Liao et al. [1989], based on a four-wave interaction process [Lee and Kuo, 1984a], to interpret that "explosive spread F" was caused by lightning-induced whistler waves. It was suggested that the Jicamarca 50 MHz radar detected whistler wave-excited field-aligned, zero-frequency modes and lower hybrid waves.

Although NAU transmitter provides a source of 28.5 kHz/40.75 kHz whistler waves for our Arecibo experiments, it operates routinely for communication purposes, but not for scientific research. Thus, to have a controlled study of whistler wave interactions with space plasmas, we used HF heater waves to create ionosphere ducts to facilitate the coupling of NAU signals from neutral atmosphere into the ionosphere. These experiments were inspired by our earlier Arecibo experiments [Lee et al., 1992], suggesting that heater generated large-scale ionospheric irregularities could support conjugate 28.5 kHz whistler mode propagation between Puerto Rico and Argentina along the L=1.35 magnetic flux tube. In our heating experiments performed during July 22 - August 1, 1997 at Arecibo Observatory, ionospheric ducts in the form of parallel-plate waveguides were created by the Arecibo HF heater. They were detected by the Arecibo 430 MHz radar and seen as slanted stripes in the radar range-time-intensity (RTI) plots [Lee et al., 1998]. Enhanced coupling of NAU signals at 28.5 kHz was seen in the conjugate whistler wave propagation experiments conducted, subsequently, between Arecibo, Puerto Rico and Trelew, Argentina [Starks et al., 2001] using matched filter technique [Starks and Lee, 2000].

After Arecibo HF heater was damaged by Hurricane Georges in 1998 and dismantled, we have been relying on naturally occurring ionospheric irregularities during spread F process for the

controlled study of NAU-launched 40.75 kHz whistler wave interactions with ionospheric plasmas and inner radiation belts above Arecibo. The experiment setup is described in Section 2. Discussed in Section 3 are whistler wave interactions with the ionospheric plasmas. Two kinds of four wave interactions processes are examined. They yield distinctively different ionospheric effects in F region, which can be distinguished by plasma line measurements using the Arecibo 430 MHz radar. Presented in Section 4 are whistler wave interactions with inner radiation belts to cause the precipitation of energetic electrons of ~ 0.4 MeV into the lower ionosphere, leading to detection of E region plasma line enhancement. Future experiments using the newly constructed Arecibo HF heater to extend our research is briefly addressed in Section 5. Summary and conclusion are finally given in Section 6.

2. Experiment Setup at Arecibo

Illustrated in Figure 1 is the experiment setup at Arecibo, showing that an O-mode wave injected vertically from the Arecibo HF heater can generate ionospheric ducts in the form of large plasma sheets (i.e., parallel-plate waveguides) within the meridional plane, as demonstrated in our 1997 Arecibo experiments [Lee et al., 1998] as well as our Gakona experiments [Cohen et al., 2008]. The radar detection of these plasma sheets yields slanted stripes in RTI plots during ExB plasma drifts across the radar beam [see Figure 2]. Interestingly enough, our recent work predicts that microwaves can produce a filament-type of ionospheric ducts [Whitehurst et al., 2012a] as delineated in Figure 3, which can be corroborated in future experiments at Arecibo.

As shown in Figure 1, a large fraction of incident NAU VLF wave power is reflected and propagates as subionospheric signals in the Earth-ionosphere waveguide along path 2. In the absence of ionospheric irregularities a smaller fraction estimated to be ~7.5% [[Pradipta et al.,

2007] enters the ionosphere and propagates in the whistler mode along the geomagnetic field lines as denoted as Path 1. Those radio wave-induced ionospheric ducts can facilitate the entering of NAU signals into the ionosphere. Along the L=1.35 magnetic field line, NAU signals at 28.5 kHz (earlier) or 40.75 kHz (current) are always greater than the lower hybrid resonance frequency in the ionosphere. Hence, the signals could most likely propagate as unducted whistler-modes from Puerto Rico to reach the ionosphere above Trelew (earlier) or Puerto Madryn, Argentina. That is, they should only experience one hop with a possible specular reflection at the ionosphere in the conjugate hemisphere. However, we also observed cases in our 1997 experiments that NAU whistler waves propagated in a duct [Starks et al., 2001].

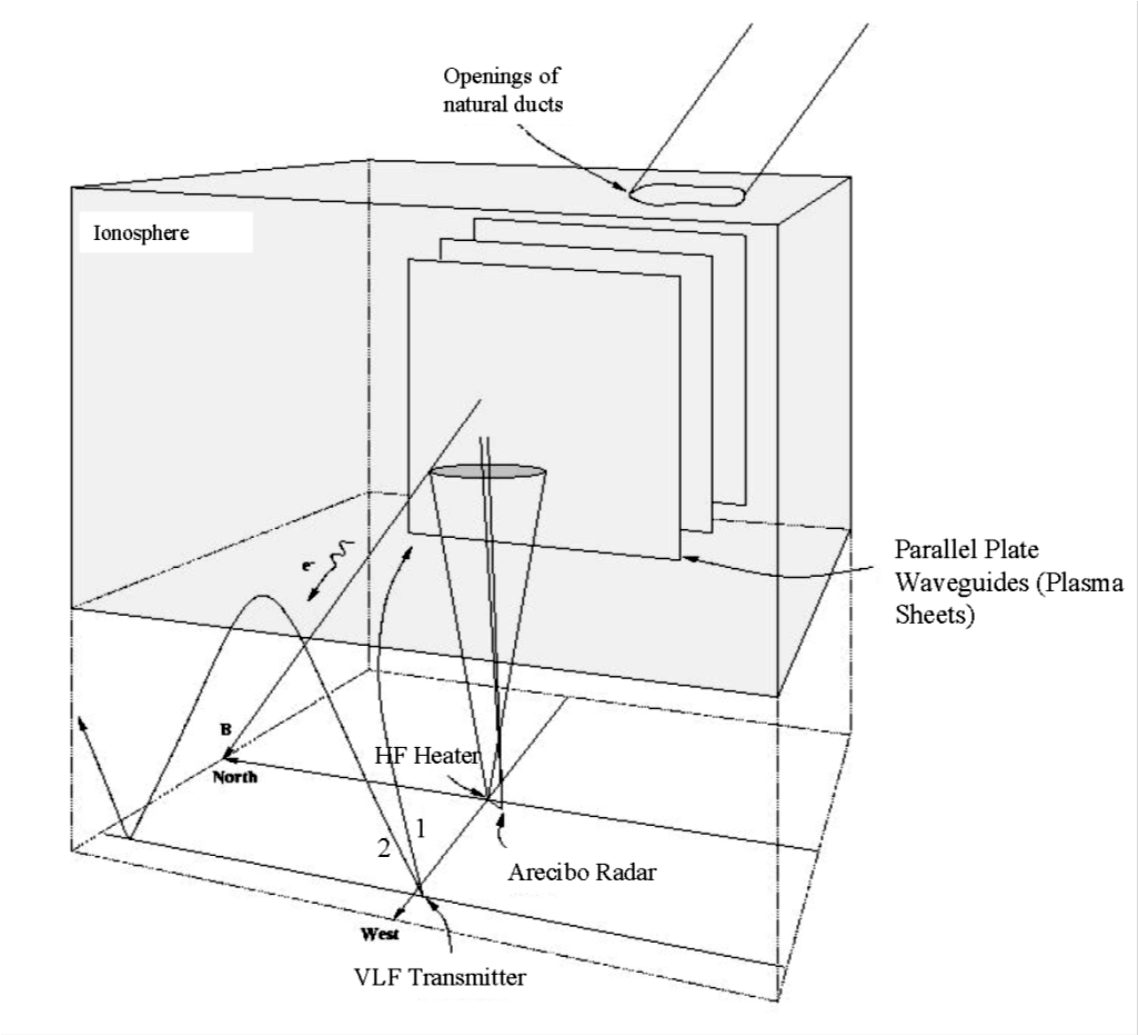

Figure 1. Schematic illustration of HF ionospheric heating experiments at Arecibo. It shows the guiding of the 28.5 kHz waves by large-scale sheet-like ionospheric irregularities and the subsequent coupling into natural ducts, as well as the radar diagnoses of the induced ionospheric effects. Ducted whistler waves and subionospheric VLF wave propagation paths are labeled as 1 and 2, respectively.

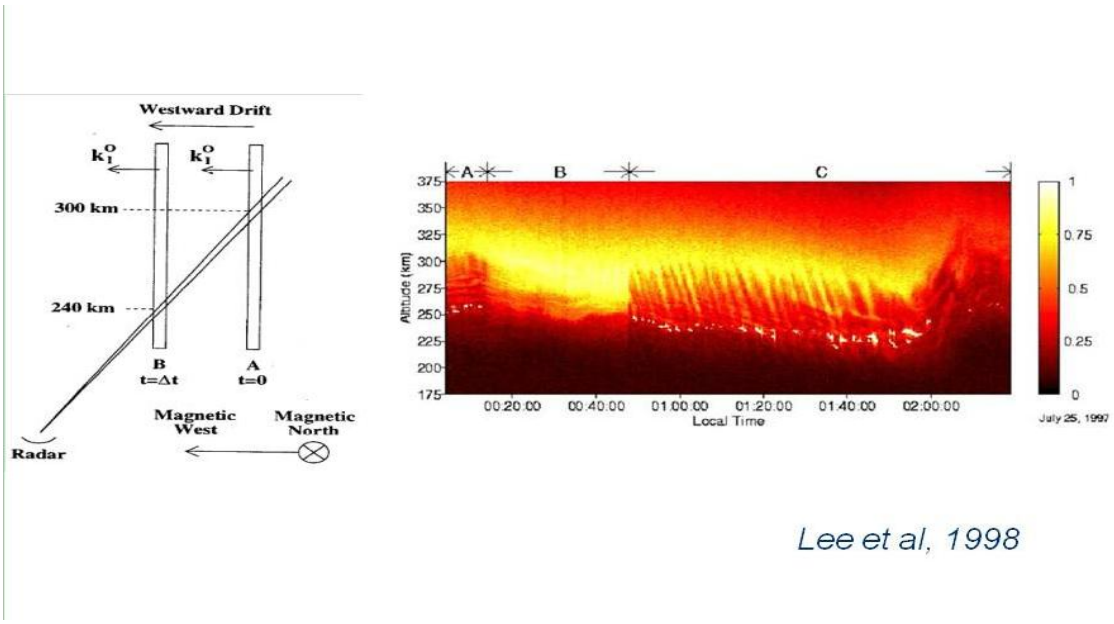

Figure 2. Arecibo 430 MHz radar-detection of large plasma sheets, undertaking ExB drifts across the radar beam, seen as dashed lines in RTI (range time intensity) plots.

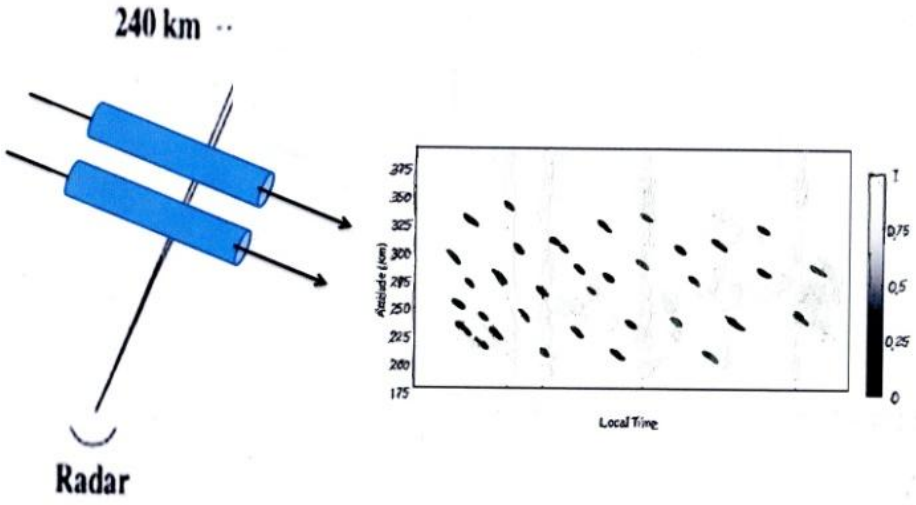

Figure 3. It is expected that Arecibo 430 MHz radar can detect filament type of microwave-excited ionospheric ducts, undertaking ExB drifts across the radar beam, seen as dashed lines in RTI plots.

Since Arecibo HF heater was damaged by hurricane in 1998, we have been conducting whistler wave experiments in the past decade in the presence of spread F events, which are associated with the occurrence of naturally occurring ionospheric irregularities. The experiment setup is basically the same as that described earlier in Figure 1. Discussed separately below are NAU whistler wave interactions with ionospheric plasmas above Arecibo and with the inner radiation belts along the L = 1.35 field line.

3. Whistler Wave Interactions with the Ionosphere

3.1. Excitation of Meter-scale Electrostatic Waves

We have estimated that a small percentage of the radiated power from NAU emissions can couple into the ionosphere and that the electric field amplitudes of 40.75 kHz whistler-mode waves would reach 1 mV/m in the F region [Labno et al., 2007]. These whistler waves are intense enough to cause four wave interactions process, exciting meter-scale lower hybrid waves and zero-frequency field-aligned density irregularities. This process satisfies the following wave frequency matching and wave vector matching conditions expressed by (1a) and (1b), respectively [Labno et al., 2007].

$$\omega_o = \omega^{+}_{\ell h} - \omega_{s,} \quad \omega_o = \omega^{-}_{\ell h} + \omega^{*}_{s}, \tag{1a}$$

$$\mathbf{k_o} = \mathbf{k_+} - \mathbf{k_S}, \quad \mathbf{k_o} = \mathbf{k_-} + \mathbf{k_S} \tag{1b}$$

where (ω_o, $\mathbf{k_o}$) represents the NAU-generated whistler wave, ($\omega^-_{\ell h}$, $\mathbf{k}_-$) the Stokes lower hybrid waves, ($\omega^+_{\ell h,}$ $\mathbf{k}_+$) the anti-Stokes lower hybrid waves, and (ω_s, $\mathbf{k_S}$) the zero-frequency field-aligned density striations. This process can be understood in terms of the schematic given in Figure 4. Note that the 40.75 kHz whistler wavelength is about 300 m, while the excited lower hybrid waves and zero-frequency modes are meter-scale electrostatic modes. Therefore, $k_o << k_+ \approx k_- << k_S$. And, although the lower hybrid waves have a single frequency equal to the NAU whistler wave frequency (i.e., 40.75 kHz), they possess a spectrum of wavelengths.

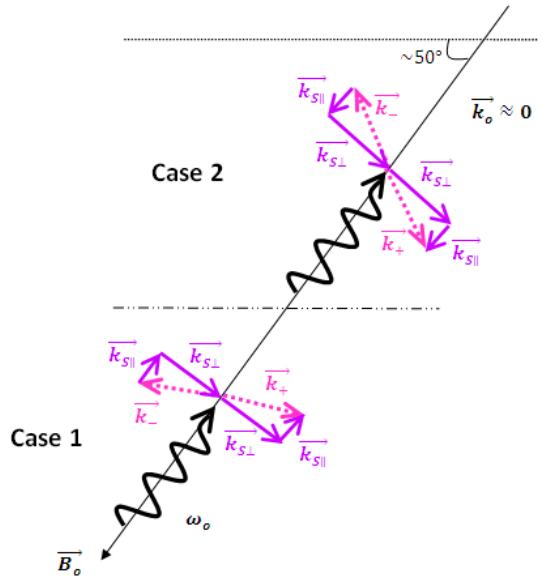

Figure 4. Schematic of the four-wave interaction process for the NAU 40.75 kHz whistler-mode wave (ω_o, $\mathbf{k_o}$) to parametrically excite meter-scale Stokes ($\omega^-_{\ell h}$, $\mathbf{k}_-$) and anti-Stokes ($\omega^+_{\ell h,}$ $\mathbf{k}_+$) lower hybrid waves together with the zero-frequency, (ω_s, $\mathbf{k_S}$) field-aligned density striations. The excited lower hybrid waves have a single frequency equal to the NAU whistler wave frequency, but a spectrum of wavelengths.

Two possible interaction configurations, labeled as two cases in Figure 4, show that it is equally likely for the excited lower hybrid waves to propagate either upward or downward. Because

lower hybrid waves can effectively accelerate electrons along the geomagnetic field, it means that electrons can be accelerated both upward and downward along the magnetic field. The upward and downward accelerated electrons subsequently give rise to plasma waves, detected by Arecibo radar as frequency-downshifted and frequency-upshifted plasma lines (PL), respectively. One set of enhanced PL in F region recorded in 2004 Arecibo experiments is shown in Figure 5 [Labno et al., 2007]. This set of PL data recorded 10 seconds apart sequentially at 20:49:07, 20:49:17, and 20:49:27 LT on December 25, 2004. It shows the occurrence of F-region PL enhancement at 20:49:17 LT, and disappearance in less than 10 seconds. The marked features of these enhanced PL are noted as follows. They appeared in the presence of spread F process at altitudes around 320 ±80 km, having a SNR of ~ 6, and a center frequency at 4 MHz with a bandwidth of ~ 1.5 MHz. This mechanism yields electron energization in the range of 7.2 – 15 eV. No F-region PL enhancement events were observed in the absence of spread F activities.

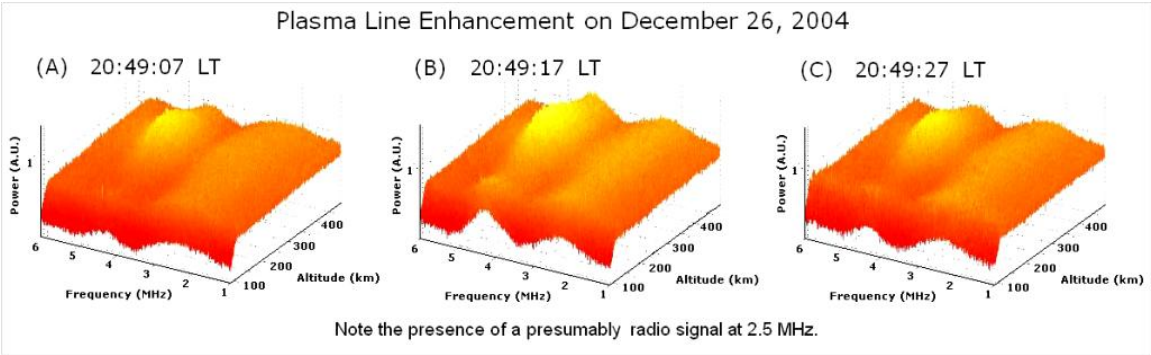

Figure 5. A set of PL data recorded 10 seconds apart sequentially at 20:49:07, 20:49:17, and 20:49:27 LT on December 25, 2004. These AFI (altitude-frequency-intensity) plots display

measured F-region PL enhancement in the presence of spread F event, when NAU transmitter was turned on [Labno et al., 2007].

3.2. Excitation of Ten Meter-scale Electrostatic Waves

A distinctively different PL enhancement in F region was observed in our 2008 Arecibo experiments. The most striking feature is that only frequency-downshifted PL were detected by Arecibo radar, implying that ionospheric electrons were solely accelerated upward along the Earth's magnetic field. A new mechanism for direct acceleration of ionospheric electrons by NAU 40.75 kHz whistler waves was recently proposed [Rooker et al, 2012a]. This mechanism also involves a four wave interaction process. While the wave frequency matching relation is same as that for the mechanism of Labno et al. [2007], the wave vector matching relation is different as depicted in Figure 6. That is, in this new mechanism: $\mathbf{k}_{+\|} = \mathbf{k}_o$, $\mathbf{k}_{+\perp} = \mathbf{k}_S$, and $\mathbf{k}_{-\|} = \mathbf{k}_o$, $\mathbf{k}_{-\perp} = -\mathbf{k}_S$. In other words, the excited lower hybrid waves have their parallel and perpendicular wave vectors equal to the whistler wave vector $\mathbf{k}_o$ and the irregularity wave vector $\mathbf{k}_S$, respectively.

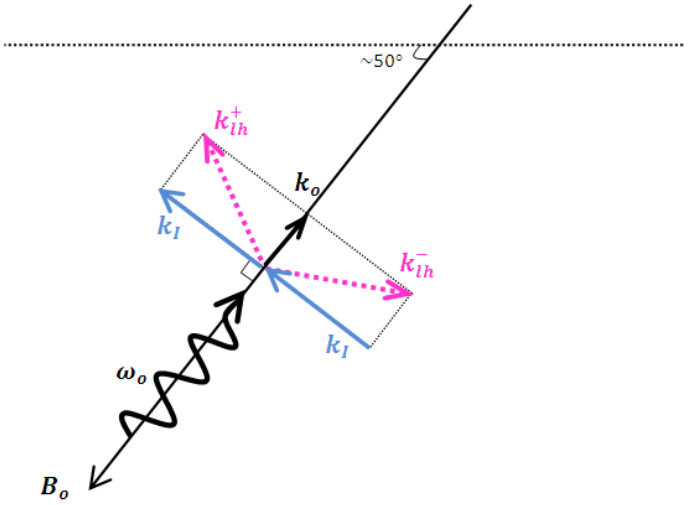

Figure 6. Depiction of the four-wave interaction process leading to upward acceleration of electrons along the magnetic field line by up-propagating whistler waves.

From the given information, viz., whistler wave frequency (40.75 kHz), electron gyro-frequency (~1.0 MHz), and electron plasma frequency (4.2 MHz), we can calculate the whistler wavelength to be ~350 m and the scale length of lower hybrid waves is about 15 m. In the experiments, coded-long pulse radar technique was used to take plasma line measurements in the altitude range of 90 to 645 km. The Arecibo CADI (Canadian Advance Digital Ionsosonde) and a VLF receiver were operated to monitor the background ionospheric conditions and the presence of NAU 40.75 kHz signals, respectively. Ionograms were generated every five minutes and NAU 40.75 kHz signals were detected continuously during the entire experiment. Displayed in Figure 7 is a series of enhanced plasma line data in the form of six AFI (altitude-frequency-intensity) plots. From top left to right the data was recorded at 23:00 (LT), 23:31 (LT), and 00:00 (LT) on Aug. 4/5, 2008, respectively. From bottom left to right, it was recorded at 00:30 (LT), 01:00 (LT), and 01:31 (LT) on Aug. 5, 2008, respectively. The six corresponding ionograms recorded to provide information on background ionosphere conditions are given in Figure 8. It can be seen from Figures 7 and 8 that following the development of spread F echoes, enhanced plasma lines intensified. It supports the expectation that spread F irregularities facilitates the entering of NAU signals into the ionosphere, which causes the four wave interactions process.

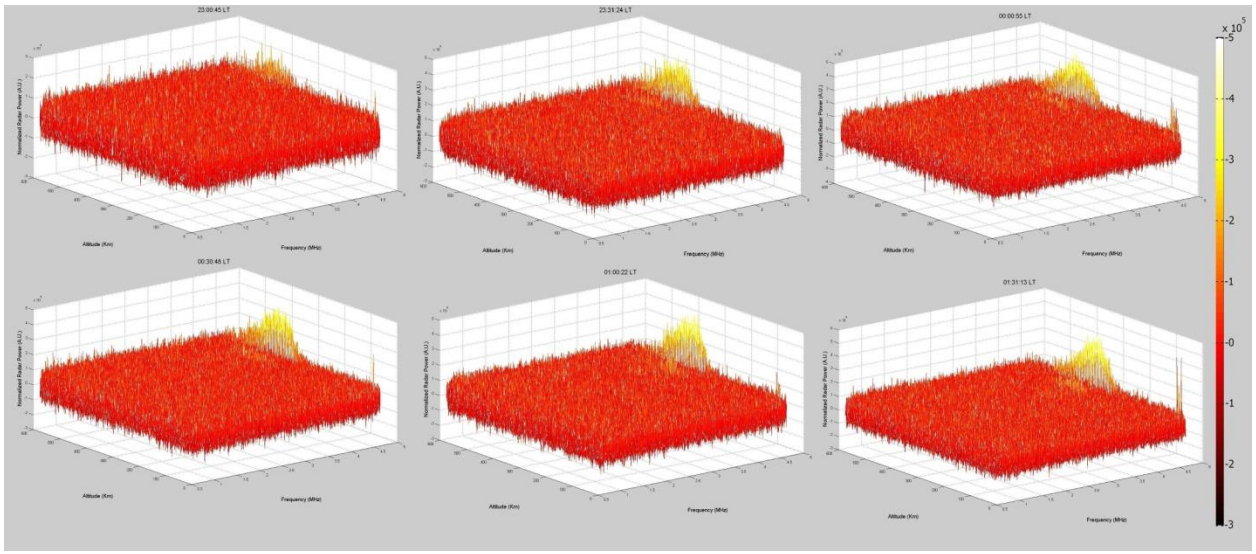

Figure 7. The AFI (altitude-frequency-intensity) plots show the characteristic features of plasma line enhancement. In the top panel from left to right we have data recorded at 23:00 (LT), 23:31 (LT), and 00:00 (LT) on Aug. 4/5, 2008, respectively. In the bottom panel from left to right, the data was recorded at 00:30 (LT), 01:00 (LT), and 01:31 (LT) on Aug. 5, 2008, respectively.

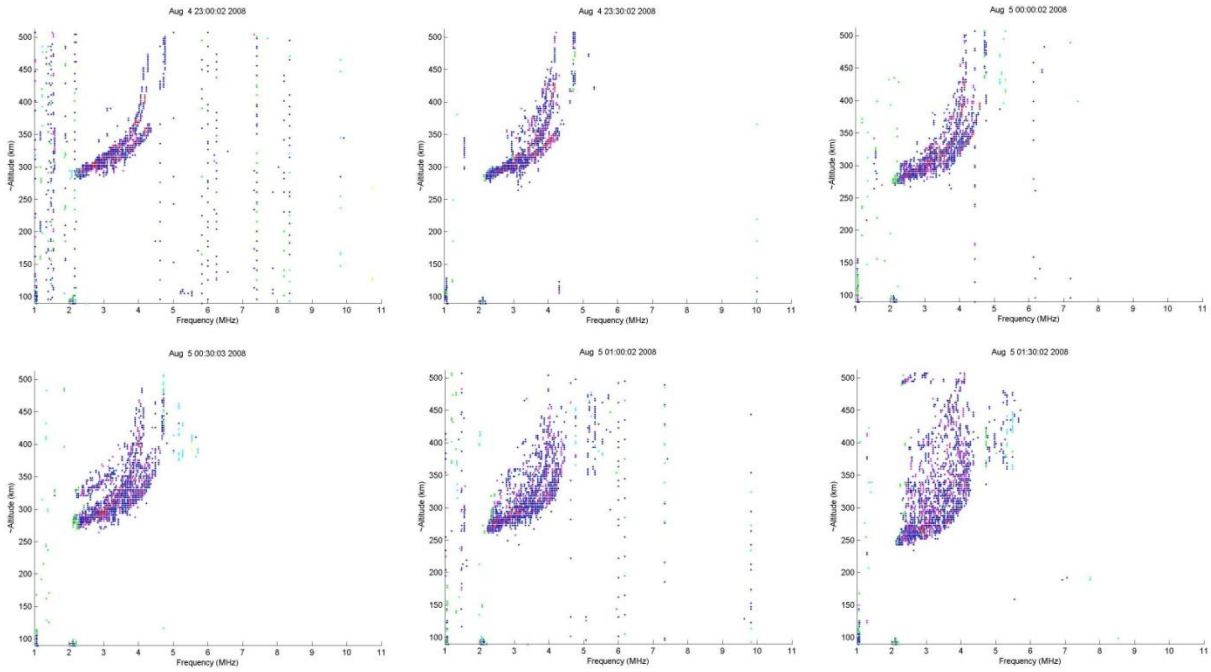

Figure 8. Corresponding to the six plasma line measurements, six ionograms were recorded every five minutes to monitor the background ionospheric conditions.

The characteristic features of these frequency-downshifted plasma lines are as follows. They covered a broader range of altitudes (~ 300 km), having a center frequency at 4.5 MHz with a rather narrow frequency bandwidth (~12 kHz). The inferred energy range of accelerated ionospheric electrons is $13.0 \pm 1.2 \times 10^{-5}$ eV. These enhanced plasma lines last for a much longer period of time (> a few minutes).

4. Whistler Wave-interactions with Radiation Belts

After NAU signals propagate upward in the whistler-mode from Puerto Rico to the conjugate location in Argentina, they interact with the inner radiation belts at L = 1.35, which causes precipitation of trapped electrons into the lower ionosphere. The precipitated energetic particles streaming along the magnetic field are detected by Arecibo radar as enhanced plasma lines in the E region with relatively narrow frequency spectra. The possible correlation between E-region plasma line enhancement and NAU operation was established in our January 1/2 2006 experiments [Pradipta et al., 2007] by happenstance.

Our VLF receiver detected no NAU signals from 22:00 on January 1 to 01:45 LT on January 2, indicating that the transmitter was turned off. From 01:45 through the end of our experiments at 06:00 LT our VLF receiver showed that the NAU transmitter had returned to continuous operations. This unexpected sequence provided us with an opportunity to test for correlation between plasma line enhancement and NAU 40.75 kHz emissions. During the entire 8 hour

period the Arecibo 430 MHz incoherent scatter radar (ISR) looked to local zenith, operating in repeated sequences of 20-minutes backscatter power and 10 minutes plasma line (PL) operations.

The timeline for the experiments conducted on the night of January 1 – 2, 2006 is presented in Figure 9. Heavy red dashed lines mark the time period for PL mode operations. NAU ON/OFF periods are indicated below the local-time axis. The bar chart display in Figure 9 clearly shows that the occurrence rate of PL enhancements at E-layer altitudes increased rapidly after NAU was turned on at 01:45 LT. The causative relationship between PL enhancement and NAU transmission-triggered electron precipitation can also be explained in terms of the average occurrence rate. It increased from 0.25 event per minute when NAU was OFF to 0.75 event per minute when NAU was ON. Displayed in Figure 10 is the plot of E Region PL Enhancement Event Rate (i.e., number of events per minute in each of the 10 minute PL measurement period) on the night of 1/2 January 2006. This alternative way to display our 1/2 Jan 2006 PL data shows that, on the average, the event rate had tripled when NAU was ON in comparison to that when NAU was OFF. We recorded 16 (1.9%) PL enhancement events while NAU signals were absent and 45 (5.35%) after transmissions resumed. This factor of 2.8 increase in PL enhancement rates between NAU On/Off periods strongly suggests that a causative relationship between them.

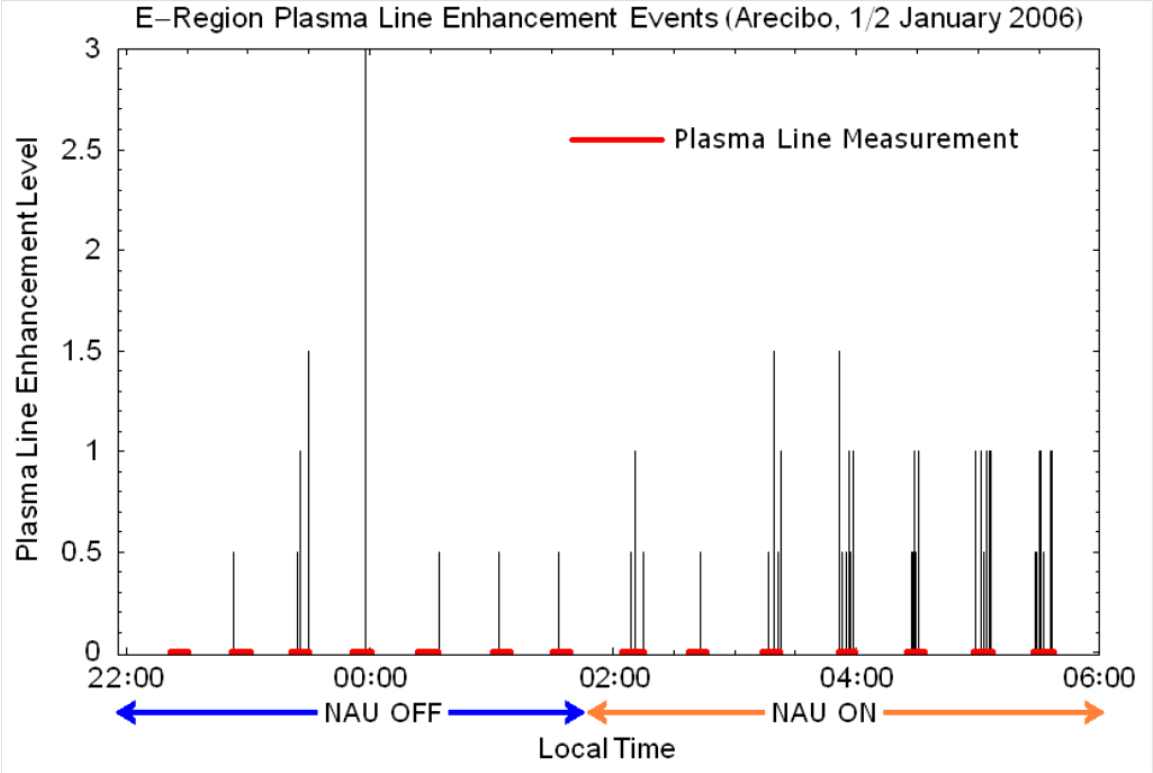

Figure 9. The occurrence rate of E-region PL enhancement increased rapidly after the NAU transmitter was turned ON. It demonstrates that significant electron precipitation can be caused by the NAU-generated 40.75 kHz whistler-mode waves, leading to prominent E region plasma effects.

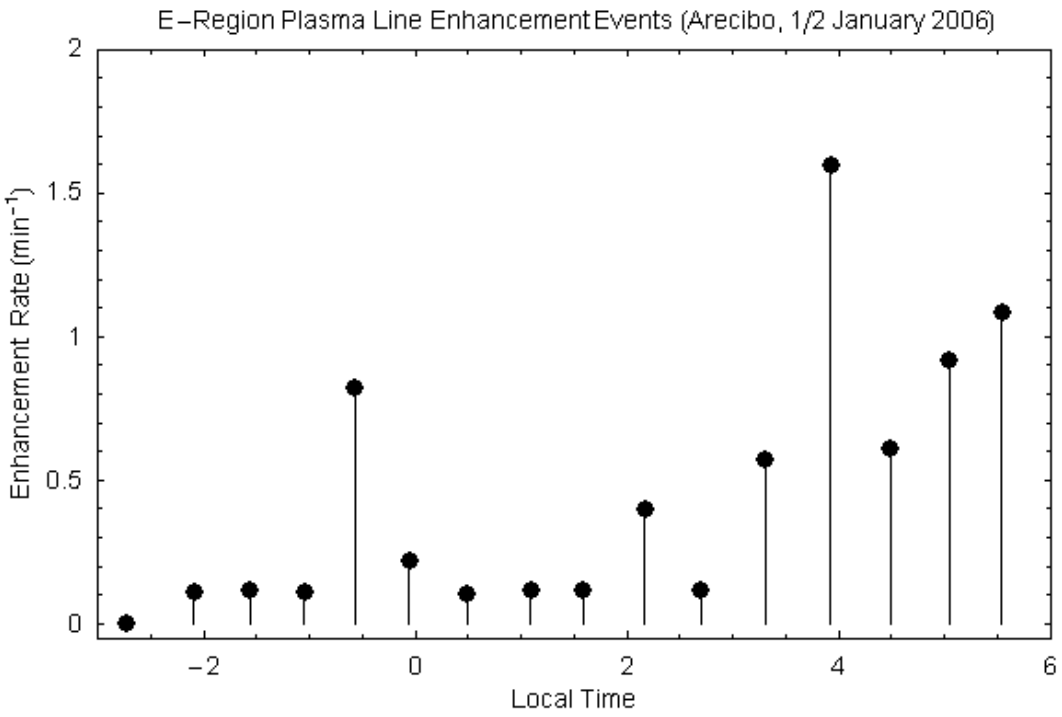

Figure 10. The plot of E Region PL Enhancement Event Rate on the night of 1/2 January 2006. This is an alternative way to display our 1/2 Jan 2006 PL data, showing that, on the average, the event rate had tripled when NAU was ON in comparison to that when NAU was OFF. It strongly suggests a causative relationship between them.

Shown in Figure 11 is a typical set of plasma line (PL) measurements in FRI spectra. From left to right the FRI plots correspond to the measurements of PL sequences beginning at 05:01:07, 05:01:17, and 05:01:27 LT on January 2, 2006. Only the middle plot shows an E-layer PL enhancement characterized by spiky bursts that last for a period of time shorter than 10 s. The enhanced PL events have a signal-to-noise ratio (SNR) of 4 to 5 and appeared at altitudes near 120 ± 20 km. Near this time neither the ISR backscatter power profile nor the ionograms showed the presence of significant E-region plasmas or sporadic E layers. The enhanced PL spectrum has center frequency of ~2.5 MHz with a ~1.5 MHz bandwidth. This data suggest that E-layer PL enhancements above Arecibo are episodic phenomena of a duration < 10 s.

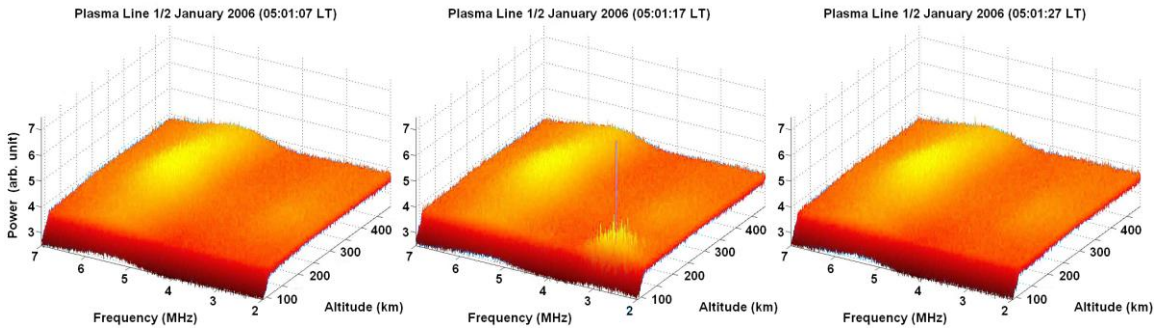

Figure 11. A set of E-region plasma line enhancement data recorded at 05:01:07, 05:01:17, and 05:01:27 LT, respectively, on January 2, 2006 when NAU transmitter was turned ON.

These characteristic features of enhanced E-region plasma lines support the following scenario [Pradipta et al., 2007]. NAU-generated 40.75 kHz whistlers interact with energetic electrons of ~ 0.4 MeV in radiation belts at L = 1.35, and subsequently cause electron precipitation into the lower ionosphere to ionize neutral particles with ionization energies of ~ 13 eV. The precipitated electrons stream along the Earth's magnetic field, giving rise to enhanced E-region plasma lines with a center frequency of 2.5 MHz and a bandwidth of 1.5 MHz. This frequency spectrum corresponds to electron energies of 2.3 – 8.5 eV, which are in good agreement with the residual energies of those precipitated electrons from the radiation belts.

5. Future Experiments

It is expected that the new Arecibo HF heater will become available for experiments soon. We will then be able to conduct aforementioned experiments using the beat wave technique. In short, we studied this technique recently in Gakona experiments for the controlled study of VLF whistler wave interactions with ionospheric plasmas and the outer radiation belts at L = 4.9 [Rooker et al., 2012b]. A sequence of beat wave-generated whistler waves at 2, 6.5, 7.5, 8.5, 9.5,

11.5, 15.5, 22.5, 28.5, and 40.5 kHz had been successfully detected. For example, transmitting one Arecibo HF wave at 5.1 MHz and the other at 5.12 MHz produces an artificial antenna in the ionosphere via ponderomotive force that radiates at the difference frequency of 20 kHz. In other words, Arecibo HF heater operated with the beat wave technique will provide a source of whistler waves in the range of VLF/LF waves (e.g., 3 - 50 kHz).

Artificial ionospheric ducts can be created by microwaves using Arecibo 2.38 GHz radar [Whitehurst et al., 2012b]. Hence, the proposed scenario is as follows. Employing the beat wave technique, we generate whistler waves at a selected frequency (e.g., 20 kHz) in the ionosphere. The Arecibo 430 MHz radar will be used to remotely diagnose the whistler wave-induced ionospheric effects, and also monitor the background ionospheric plasma conditions. Filament-type of ionospheric ducts, created by 2.38 GHz microwaves, will favorably guide whistler waves to propagate along the L = 1.35 field lines and reach the inner radiation belts. Charged particles in the radiation belts at different energies, depending on the frequency of created whistler waves, can be scattered into loss cone and, subsequently, precipitate into the lower ionosphere above Arecibo. Ionospheric effects induced by precipitated particles can be detected by the Arecibo 430 MHz radar. These experiments will extend our research for controlled study of whistler wave interactions with space plasmas.

6. Summary and Conclusion

We report a series of experiments conducted at Arecibo Observatory in the past, aimed at the investigation of NAU launched 40.75 kHz whistler wave interactions with ionospheric plasmas and the inner radiation belts at L = 1.35. Arecibo radar, CADI, and optical instruments were used to monitor the background ionospheric conditions and detect the induced ionospheric

plasma effects. Four-wave interaction processes produced by whistler waves in the ionosphere can excite lower hybrid waves, which can accelerate ionospheric electrons. Furthermore, whistler waves propagating into the magnetosphere can trigger precipitation of energetic electrons from the radiation belts. Radar and optical measurements can distinguish wave-wave and wave-particle interaction processes occurring at different altitudes. Electron acceleration by different mechanisms can be verified from the radar measurements of plasma lines. To facilitate the coupling of NAU-launched 40.75 kHz whistler waves into the ionosphere, we have relied on naturally occurring spread F irregularities to serve as the ionospheric ducts. However, artificial waveguides can be favorably generated by HF heater waves, as demonstrated in our earlier Arecibo experiments and further confirmed in our recent Gakona experiments at HAARP. The use of the newly constructed Arecibo HF heater can extend the study of whistler wave interactions with the ionosphere and the magnetosphere/radiation belts as well as the whistler wave conjugate propagation between Arecibo and Puerto Madryn, Argentina.

Acknowledgments. This paper was presented at ISEA13 as "Whistler Wave-induced Ionospheric Plasma Turbulence: Source Mechanisms and Remote Sensing" by M.C. Lee et al. The reported research was supported by AFOSR grant FA9550-09-1-0391. The Arecibo Observatory is part of the National Astronomy and Ionosphere Center (NAIC), a national research center operated by SRI International, USRA and UMET, under a cooperative agreement with the National Science Foundation (NSF).

References

Cohen, J. A., R. Pradipta, L. M. Burton, A. Labno, M. C. Lee, B. J. Watkins, C. Fallen, S. P.

Kuo, W J Burke, D Mabius, and B Z See, "Generation of ionospheric ducts by the HAARP HF heater", Phys. Scr. T142 (2010) 014040 (7pp) doi:10.1088/00318949/2010/T142/014040.

Labno, A., R. Pradipta, M. C. Lee, M. P. Sulzer, L. M. Burton, J. A. Cohen, S. P. Kuo, and D. L. Rokusek (2007), Whistler-mode wave interactions with ionospheric plasmas over Arecibo, J. Geophys. Res., 112, A03306, doi:10.1029/2006JA012089.

Lee, M.C. and S.P. Kuo, Production of lower hybrid waves and field-aligned plasma density striations by whistlers, J. Geophys. Res., 89, 10873, 1984a.

Lee, M. C., and S. P. Kuo , Excitation of magnetostatic fluctuations by filamentation of whistlers, J. Geophys. Res., 89, 2289 1984b.

Lee, M.C., K.L. Koh, K.D. Vilece, S. Basu, K.M. Groves, and M.P. Sulzer, Generation of artificial ionospheric ducts for guided VLF wave propagation, Proceedings of International Beacon Satellite Symposium, Cambridge, Massachusetts, 1992.

Lee, M.C., R.J. Riddolls, W.J. Burke, M.P. Sulzer, S.P. Kuo, and E.M.C. Klien, Generation of large sheet-like ionospheric plasma irregularities at Arecibo, Geophys. Res. Lett., 25, 3067, 1998.

Liao, C.P., J.P. Freidberg, and M.C. Lee, Ionospheric plasma modifications caused by the lightning induced electromagnetic effects, J. Atmos. Terres. Phys., 51, 751, 1989.

Pradipta, R., A. Labno, M. C. Lee, W. J. Burke, M. P. Sulzer, J. A. Cohen, L. M. Burton, S. P. Kuo, and D. L. Rokusek (2007), Electron precipitation from the inner radiation belt above Arecibo, Geophys. Res. Lett., 34, L08101, doi:10.1029/2007GL029807.

Rooker, L.A., M.C. Lee, R. Pradipta, L.M. Ross, B.Z. See, M.J. Sulzer, C. Tepley, S. Gonzalez, N. Aponde, S.P. Kuo, Direct acceleration of ionospheric electrons by 40.75 kHz whistler waves over Arecibo, Geophys. Res. Lett., 2012a, submitted.

Rooker, L.A., M.C. Lee, and R. Pradipta, Generation and detection of whistler wave induced space plasma turbulence at Gakona, Alaska, Phys. Scr., 2012b (in press).

Starks, M.J. and M.C. Lee, Matched filtering for the measurement of conjugately ducted VLF transmissions, Radio Sci., 35, 351, 2000.

Starks, M.J., M.C. Lee, and P. Jastrzebski, Interhemispheric propagation of VLF

transmissions in the presence of ionospheric HF heating, J. Geophys. Res., 106, 5579, 2001.

Whitehurst, L.N., M.C. Lee, and R. Pradipta, Large plasma filaments and geomagnetic field fluctuations excited concomitantly by solar powered microwave transmissions, Phys. Scr., 2012a (in press).

Whitehurst, L.N., M.C. Lee, and R. Pradipta, Solar powered microwave transmission for communications and remote sensing, IEEE Trans. Plas. Sci., 2012b, submitted.

Woodman and C. La Hoz, Radar observations of F region equatorial irregularities, J. Geophys. Res., 81, 5447, 1976.

Woodman, R.F. and E. Kudeki, A causal relationship between lightning and explosive spread F, Geophys. Res. Lett., 11, 12, doi:10.1029/GL011i012p01165, 1984.

AFOSR Deliverables Submission Survey

Response ID: 2163 Data

1.

1. Report Type

Final Report

2. Primary Contact E-mail

Contact email if there is a problem with the report.

mclee@MIT.EDU

3. Primary Contact Phone Number

Contact phone number if there is a problem with the report

617-353-3363

4. Organization / Institution name

Boston University

5. Grant/Contract Title

The full title of the funded effort.

Investigation of Ionospheric Turbulence and Whistler Wave Interactions with Space Plasmas

6. Grant/Contract Number

AFOSR assigned control number. It must begin with "FA9550" or "F49620".

FA9550-09-1-0391

7. Principal Investigator Name

The full name of the principal investigator on the grant or contract.

Min-Chang Lee

8. Program Manager

The AFOSR Program Manager currently assigned to the award

Dr. Cassandra Fesen

9. Reporting Period Start Date

06/01/2009

10. Reporting Period End Date

08/31/2012

11. Abstract

We report on AFOSR-sponsored research titled “Investigation of Ionospheric Turbulence and Whistler Wave Interactions with Space Plasmas" (FA9550-09-1-0391 for the period of June 1, 2009 – August 31, 2012). It includes two parts: (1) naturally occurring and radio wave-induced large-and medium-scale ionospheric turbulence, and (2) whistler wave-generated short-scale ionospheric turbulence. Two types of large- and medium-scale ionospheric turbulence are discussed separately, viz., (a) anomalous heat source-induced acoustic gravity waves (AGW), and (b) HF radio wave-excited large ionospheric ducts. Our whistler wave injection experiments have been conducted at Arecibo, Puerto Rico, and Gakona, Alaska, using Naval 40.75 kHz transmitter (code-named NAU) and HAARP heater to generate VLF whistler waves, respectively. These experiments are aimed at the controlled study of whistler wave interactions with ionospheric plasma and inner (outer) radiation belts at L = 1.35 (4.6). Several journal and conference papers as well as students’ Ph.D./M.S./B.S. theses have resulted from these research projects.

12. Distribution Statement

This is block 12 on the SF298 form.

Distribution A - Approved for Public Release

13. Explanation for Distribution Statement

If this is not approved for public release, please provide a short explanation. E.g., contains proprietary information.

14. SF298 Form

Please attach your SF298 form. A blank SF298 can be found here. Please do not spend extra effort to password protect or secure the PDF, we want to read your SF298. The maximum file size for SF298's is 50MB.

SF 298 (typed-report-cover).pdf

Upload the Report Document. The maximum file size for the Report Document is 50MB.

2012-AFOSR-final-report-FA9550-09-1-0391.pdf

16. Archival Publications (published) during reporting period:

Kuo, S. P., W.-T. Cheng, J. A. Cohen, R. Pradipta, M. C. Lee, S. S. Kuo, and A. Snyder (2009), "Simultaneous generation of large-scale density irregularities and geomagnetic pulsations via filamentation instability", Geophys. Res. Lett., 36, L09107, doi:10.1029/2009GL037942. Cohen, J. A., R. Pradipta, L. M. Burton, A. Labno, M. C. Lee, B. J. Watkins, C. Fallen, S. P. Kuo, W. J. Burke, D. Mabius, and B. Z. See, "Generation of ionospheric ducts by the HAARP HF heater", Phys. Scr. T142 (2010) 014040 (7pp) doi:10.1088/0031-8949/2010/T142/014040. Pradipta. R and M C Lee, Investigation of acoustic gravity waves created by anomalous heat sources: experiments and theoretical analysis, Phys. Scr. T149 (2012), in press. Whitehurst, L N, M C Lee, and R Pradipta, "Large plasma filaments and geomagnetic field fluctuations excited concomitantly by solar powered microwave transmissions", Phys. Scr. T149 (2012), in press. Rooker, LA, M C Lee, R Pradipta, "Generation and Detection of Whistler Wave Induced Space Plasma Turbulence", Phys. Scr. T149 (2012), in press. Pradipta, R., L.A. Rooker, L.N. Whitehurst, M.C. Lee, M.P. Sulzer, S. Gonzalez, C. Tepley, N. Aponte, B.Z. See, K.P. Hu, L.M. Ross, "Whistler Wave-induced Ionospheric Plasma Turbulence: Source Mechanisms and Remote Sensing", to appear in a special issue of J. Atmo. Solar Terr. Phys., for ISEA 2012, Peru. Kuo, S., M. C. Lee, and A Snyder, "Simultaneous Observation of Wideband HF Attenuation and Enhanced VLF Generation", J. Geophys. Res., 2012 (under review). Rooker, L.A., M.C. Lee, R. Pradipta, L.M. Ross, B.Z. See, M.J. Sulzer, C. Tepley, S. Gonzalez, N. Aponde, S.P. Kuo, "Direct Acceleration of Ionospheric Electrons by 40.75 kHz Whistler Waves Over Arecibo", J. Geophys. Res., 2012 (under review). Whitehurst, L.N., M.C. Lee, R. Pradipta, "Solar Powered Microwave Transmission for Communications and Remote Sensing", IEEE Trans. Plasma Sci., 2012 (under review).

17. Changes in research objectives (if any):

None

18. Change in AFOSR Program Manager, if any:

Dr. Kent Miller (original) Dr. Cassandra Fesen (current)

19. Extensions granted or milestones slipped, if any:

Yes, a no-cost extension was granted.

Response ID: 2163

Survey Submitted:	Nov 25, 2012 (9:05 PM)
IP Address:	74.104.168.221
Language:	English (en-US,en;q=0.8)
User Agent:	Mozilla/5.0 (Windows NT 5.1) AppleWebKit/537.11 (KHTML, like Gecko) Chrome/23.0.1271.64 Safari/537.11
Http Referrer:	http://www.wpafb.af.mil/library/factsheets/factsheet.asp?id=9389
Page Path:	1 : (SKU: 1) 2 : Thank You (SKU: 2)

SessionID:	1353891925_50b2c0557cb048.05961454

Response Location

Country:	United States
Region:	MA
City:	Lexington
Postal Code:	02421
Long & Lat:	Lat: 42.442799, Long:-71.231697